Experimental Study of Gas Turbine Endwall Cooling with Endwall Contouring under Transonic Conditions

Arnab Roy

Dissertation submitted to the faculty of Virginia Polytechnic Institute and State University in partial fulfillment of the requirement for the degree of

Doctor of Philosophy

In

Mechanical Engineering

Srinath V. Ekkad Co-chair
Wing F. Ng Co-chair

Brian Y. Lattimer
Uri Vandsburger
Rakesh K. Kapania

January 27, 2014
Blacksburg, Virginia Tech

Keywords: Gas Turbine, Endwall Contouring, Film Cooling, Heat Transfer, Transonic Cascade

Experimental Study of Gas Turbine Endwall Cooling with Endwall Contouring under Transonic Conditions

Arnab Roy

Abstract

The effect of global warming due to increased level of greenhouse gas emissions from coal fired thermal power plants and crisis of reliable energy resources has profoundly increased the importance of natural gas based power generation as a major alternative in the last few decades. Although gas turbine propulsion system had been primarily developed and technological advancements over the years had focused on application in civil and military aviation industry, use of gas turbine engines for land based power generation has emerged as the most promising candidate due to higher thermal efficiency, abundance of natural gas resources, development in generation of hydrogen rich synthetic fuel (Syngas) using advanced gasification technology for further improved emission levels and strict enforcement in emission regulations on installation of new coal based power plants. The fundamental thermodynamic principle behind gas turbine engines is Brayton cycle and higher thermal efficiency is achieved through maximizing the Turbine Inlet Temperature (TIT). Modern gas turbine engines operate well beyond the melting point of the turbine component materials to meet the enhanced efficiency requirements especially in the initial high pressure stages (HPT) after the combustor exit. Application of thermal barrier coatings (TBC) provides the first line of defense to the hot gas path components against direct exposure to high temperature gases. However, a major portion of the heat load to the airfoil and passage is reduced through injection of secondary air from high pressure compressor at the expense of a penalty on engine performance. External film cooling comprises a significant part of the entire convective cooling scheme. This can be achieved injecting coolant air through film holes on airfoil and endwall passages or utilizing the high pressure air required to seal the gaps and interfaces due to turbine assembly features. The major objective is to maximize heat transfer performance and film coverage on the surface with minimum coolant usage.

Endwall contouring on the other hand provides an effective means of minimizing heat load on the platform through efficient control of secondary flow vortices. Complex vortices form due to the interaction between the incoming boundary layer and endwall-airfoil junction at the leading edge which entrain the hot gases towards the endwall, thus increasing surface heat transfer along its trajectory. A properly designed endwall profile can weaken the effects of secondary flow thereby improving the aerodynamic and associated heat transfer performance.

This dissertation aims to investigate heat transfer characteristics of a non-axisymmetric contoured endwall design compared to a baseline planar endwall geometry in presence of three major endwall cooling features – upstream purge flow, discrete hole film cooling and mateface gap leakage under transonic operating conditions. The preliminary design objective of the contoured endwall geometry was to minimize stagnation and secondary aerodynamic losses. Upstream purge flow and mateface gap leakage is necessary to prevent ingestion to the turbine

core whereas discrete hole cooling is largely necessary to provide film cooling primarily near leading edge region and mid-passage region. Different coolant to mainstream mass flow ratios (MFR) were investigated for all cooling features at design exit isentropic Mach number (0.88) and design incidence angle. The experiments were performed at Virginia Tech's quasi linear transonic blow down cascade facility. The airfoil span increases in the mainstream flow direction in order to match realistic inlet/exit airfoil surface Mach number distribution. A transient Infrared (IR) thermography technique was employed to measure the endwall surface temperature and a novel heat transfer data reduction method was developed for simultaneous calculation of heat transfer coefficient (HTC) and adiabatic cooling effectiveness (ETA), assuming a 1D semi-infinite transient conduction. An experimental study on endwall film cooling with endwall contouring at high exit Mach numbers is not available in literature.

Results indicate significant benefits in heat transfer performance using the contoured endwall in presence of individual (upstream slot, discrete hole and mateface gap) and combined (upstream slot with mateface gap) cooling flow features. Major advantages of endwall contouring were observed through reduction in heat transfer coefficient and increase in coolant film coverage by weakening the effects of secondary flow and cross passage pressure differential. Net Heat Flux Reduction (NHFR) analysis was carried out combining the effect of heat transfer coefficient and film cooling effectiveness on both endwall geometries (contoured and baseline) where, the contoured endwall showed major improvement in heat load reduction near the suction side of the platform (upstream leakage only and combined upstream with mateface leakage) as well as further downstream of the film holes (discrete hole film cooling). Detailed interpretation of the heat transfer results along with near endwall flow physics has also been discussed.

Acknowledgements

I wish to express my sincere gratitude to my advisors, Prof(s). Srinath Ekkad and Wing Ng for their continuous support, encouragement and thorough guidance during my doctoral studies. I am thankful to them for keeping faith in my research capabilities and providing me the opportunity to work in one of the most challenging projects in their research group. Their mentoring towards effective communication and presentation skills has certainly played an important role in my transition from a student to a professional.

I would like to thank my committee members Prof. Brian Lattimer, Prof. Uri Vandsburger and Prof. Rakesh Kapania for their valuable suggestions and advice. Special thanks to Profs. Lattimer and Vandsburger for their support during the gasification project.

I am indebted to my parents Kalyanmoy Roy and Purnima Roy for their sacrifices, prayers and blessings for my wellbeing and success. Thank you Jethu and Jemma for your encouragement to pursue doctoral studies and making sure I do not deviate halfway towards achieving my goal. I owe special gratitude to Sanchari, my dear wife for her unconditional love and support.

It has been a great pleasure and learning experience working with project sponsors from Siemens Energy Inc. Sincere thanks to Andrew Lohaus and Dr. Michael Crawford from Siemens team for providing valuable technical insights and continuing the funding support throughout my dissertation research. I am grateful to Dr. Santosh Abraham and Dr. Kapil Panchal, previous researchers in our group for providing excellent resources from their contributions towards successful completion of first three years of this project. Many thanks to Dorian Blot and Sakshi Jain for helping me conduct all the heat transfer experiments. It has been a pleasure working with both of you and thanks for adjusting to my workaholic schedules. Special thanks to Dr. Xue Song for all the discussions on heat transfer methods and co-authoring the technique paper. I would also like to thank my colleagues, past and present research group members – James, Alan, Anto, Justin, Jaideep, Sridhar, Chris, Hunter, Sean, Kevin, Colin and Jacob for lending their helping hand whenever I needed. Completing the experiments within stringent deadlines wouldn't have been possible without the help of high precision manufacturing support from the Machine Shop staff in the Mechanical Engineering Department, specially Bill Songer, Timothy Kessinger and Johnny Cox. Thanks a lot Diana for giving me special purchasing privileges that was often useful.

I would also like to thank the entire Jadavpur team at Virgina Tech - Surya, Saikat, Suvojit, Pal, Abhra da, Banga da, Abhijit da, Gupta and many others for making my weekends full of fun. Special thanks to Subhradeep and Debarati, for all the lunch and dinner invites that helped me to stay away from cooking during the final stages of my dissertation writing. Finally, I won't ever forget to mention my dearest friends from childhood school days – Saptarshi, Lamba, Tanay, Subhro, Koushik, Rechiek for their unconditional support and encouragement.

Table of Contents

List of Figures

List of Tables

Preface

This dissertation is written in a manuscript format that encompasses all three major aspects of external cooling of gas turbine endwall – upstream purge cooling, discrete hole film cooling and mateface leakage flow, put together in a coherent style that consists of three major research papers, either submitted or to be submitted (awaiting approval from sponsors) for publication in archival journals. The author was the lead graduate student in the entire research project sponsored by Siemens Energy Inc. working closely with two master's students Dorian Blot and Sakshi Jain. While investigation of aerodynamic performance was also another focus area of the research project, the author of this dissertation was responsible largely for all aspects of heat transfer performance analysis – design modification, instrumentation, reduction and data analysis with comprehensive literature review.

The first article portrays the effect of endwall contouring on heat transfer performance of a transonic turbine passage in presence of upstream slot purge flow. The second paper experimentally investigates the isolated effect of discrete hole endwall film cooling with endwall surface modification. The objective of the third paper is to understand the effect of addition of mateface gap feature on the endwall and analyze the benefits of endwall contouring for mateface leakage flow only as well as combined upstream purge and mateface gap leakage flow to simulate realistic engine cooling conditions. Finally, major contributions of this dissertation work towards gas turbine heat transfer research community have also been highlighted.

A series of appendices follow that provides information on - further experiments on a new endwall contour design optimized to minimize aerodynamic losses in presence of upstream slot (Appendix – A), an analysis to quantify the hot mainstream gas ingestion into the mateface gap (Appendix – B), development and details of the new heat transfer data reduction methodology – Linear Regression method, article submitted for publication in Measurement Science and Technology journal (Appendix – C), and finally another manuscript that was published at the International Pittsburgh Coal Conference, 2011 on computational fluid dynamics (CFD) based modeling of an entrained flow gasifier with parametric analysis of the effect of oxygen/coal and steam/coal ratio (Appendix – D). The author was involved in a project on design and CFD analysis of a laboratory scale entrained flow coal gasifier during 2010-2011 sponsored by Institute of Critical Technology and Applied Sciences, Virginia Tech.

Chapter 1 : Effect of Endwall Contouring in presence of Upstream Leakage Flow in a Transonic Turbine Blade Passage: Heat Transfer Measurements

EFFECT OF ENDWALL CONTOURING IN PRESENCE OF UPSTREAM LEAKAGE FLOW IN A TRANSONIC TURBINE BLADE PASSAGE: HEAT TRANSFER MEASUREMENTS

Arnab Roy, Dorian M. Blot, Srinath V. Ekkad, Wing F. Ng
Department of Mechanical Engineering, Virginia Tech
Blacksburg, Virginia, USA

Andrew S. Lohaus, Michael E. Crawford
Siemens Energy, Inc.
Orlando, Florida, USA

49th AIAA Joint Propulsion Conference and Exhibit, 2013, Paper no. 1587590, San Jose, California

To be submitted to AIAA Journal of Thermophysics and Heat Transfer

ABSTRACT

Comparison of heat transfer performance of a non-axisymmetric contoured endwall to a non-contoured baseline endwall in presence of leakage flow through stator-rotor rim seal interface is reported in this paper. Heat transfer experiments were performed on a high turning (~127°) turbine airfoil passage under transonic exit Mach number conditions at three leakage to mainstream mass flow ratios (MFR), 0.5%, 1% and 1.5% respectively. The contoured endwall geometry was generated to minimize stagnation and secondary aerodynamic losses. In this experiment, the blade span increases in the mainstream flow direction in order to match realistic inlet/exit airfoil surface Mach number distribution. Transient IR (Infrared) thermography technique was applied to measure endwall surface temperature and calculation of simultaneous of heat transfer coefficient (HTC) and cooling effectiveness (ETA) was performed assuming 1-D semi-infinite transient conduction theory is valid. Results show considerable reduction in area averaged HTC and higher coolant film coverage using the contoured endwall compared to baseline endwall with different levels of coolant MFRs, whereas, significant reduction was observed for cases without coolant flow and without purge slot. Net Heat Flux Reduction (NHFR) analysis was carried out combining the effect of HTC and ETA on both endwall geometries where, the contoured endwall showed major improvement on local heat load reduction especially near the suction side of the platform. The backward facing step seems to have a first order impact on endwall heat transfer coefficient distribution compared to coolant blowing cases.

INTRODUCTION

Endwall heat transfer is a critical issue for turbine designers as modern gas turbine engines operate at high temperatures. It has been estimated that increase in metal temperature by 25°C reduces the durability and life cycle of the turbine to half of its design value [1]. External cooling of the airfoils and passages is therefore an integral part of the turbine cooling system to reduce overall heat load to the surface and protect the metal surface by creating a thin coolant barrier from the hot mainstream gases. Secondary flows formed due to complex vortical interaction of

the mainstream flow boundary layer with airfoil leading edge are a major contributor to aerodynamic losses as well enhanced endwall heat transfer. Upstream slots exist between the stationary and rotating parts due to turbine assembly feature and high pressure leakage flow is introduced through these gaps in order to provide film cooling to the hub region upstream of the airfoils as well as to seal these interfaces to prevent hot gas ingestion. Endwall contouring to reduce or eliminate the effects of secondary flow structures formed inside the passages have been a topic of active research, as many researchers have found that aerodynamic losses as well as heat transfer to the surface can be reduced to a significant extent by effectively guiding the passage vortex through a desired direction along the passage. An endwall contour design optimized for aerodynamic losses that is able to reduce endwall heat load as well would improve the durability and turbine efficiency. Endwall contour shapes can be further classified into two categories – axisymmetric, where the contour shape is a function of axial coordinates only and non-axisymmetric, where a three dimensional non-linear contoured surface is generated. Axisymmetric contouring is generally employed to stator vanes, whereas non-axisymmetric has potential to improve turbine blade performance.

BACKGROUND STUDY

Several researchers have extensively studied endwall heat transfer performance in presence of leakage flow within HPT stages. A comprehensive review of widely used platform heat transfer and cooling technologies can be obtained from Han et al. [1], Dunn [2], Chyu [3], Simon and Piggush [4]. Blair [5] and Graziani et al. [6] were among the pioneering researchers on endwall heat transfer study. Blair [5] investigated film cooling performance in the presence of coolant injection from an upstream slot by using local wall thermocouple measurements as well as surface heaters. He reported significant variation of complex passage heat transfer profiles arising due to secondary flow along the endwall. Graziani et al. [6] concluded that secondary flows have a larger impact on heat transfer coefficients near suction side compared to pressure side of the airfoil. Colban et al. [7] showed that increase in upstream leakage flow increased the overall adiabatic effectiveness levels downstream of the passage and moreover, the slot exit flow is non-uniform and tends to spread towards suction side of the passage. Zhang and Moon [8] compared several upstream film cooling cases with and without a backward facing step. Adiabatic effectiveness was measured using pressure sensitive paint (PSP) technique and they reported that presence of backward facing slot reduced cooling effectiveness, compared to smooth inlet configuration. Oke et al. [9] at University of Minnesota have conducted investigations of slot injection on contoured as well as flat endwall using different slot designs. They obtained reduction of secondary flow strength by increasing the coolant flow rates as the boundary layer upstream of leading edge gets energized resulting in better cooling of pressure side. Partially blocking the slots yielded further insight on re-distribution of mass and momentum flux of the coolant. More recently Papa et al. [10] reported oil flow visualization and endwall cooling studies for different purge flow rates using heat/mass transfer analogy (naphthalene sublimation technique established by Goldstein et al. [11]). Knost and Thole [12] showed that local high heat transfer zones such as leading edge and pressure side can be significantly cooled with combination of strategically placed coolant holes along with increased upstream leakage flow rates. Ranson et al. [13] and Cardwell et al. [14] further extended this study and investigated combined effect of coolant injection from upstream slot, mate

face (misalignment between adjacent endwalls) and aft slots. They concluded that mate face leakage has a significant impact on overall coolant coverage and effectiveness due to aft slot cooling is negligible. Wright et al. [15] and Gao et al. [16] also performed film cooling experiments using PSP technique with purge flow from stator-rotor seal combined with discrete holes on endwall. They recommended that upstream slot provides adequate cooling of the platform at higher blowing ratios, hence discrete hole locations can be carefully designed and coolant usage can be minimized.

Majority of the published literature on turbine endwall cooling as presented in the brief review above are based on subsonic flow conditions, whereas in contrast there are limited studies on endwall heat transfer and film cooling measurements for high pressure transonic turbine blade cascade. Giel et al. [17] used transient liquid crystal (TLC) technique along with foil heaters to determine local heat transfer coefficients (HTC) under high speed operating conditions. Nicklas [18] applied a superposition approach to evaluate simultaneous endwall HTC and ETA distribution under transonic operating conditions. IR thermography for surface temperature measurement along with known heat flux conditions from a surface heater were used to analyze the experimental data. Jonsson et al. [19] performed film cooling experiments in presence of upstream slot leakage and discrete hole blowing and calculated simultaneous HTC, ETA and heat flux on endwall surface using non-linear regression method developed by Vogel et al. [20]. More recently, effects of endwall contouring study with emphasis on heat transfer performance (without film cooling) at design and off-design conditions was published by Panchal et al. [21] at transonic conditions. Salvadori et al. [22] used steady state PSP technique to calculate ETA distributions for fan shaped discrete cooling holes on the endwall at design isentropic exit Mach number of 0.88.

Endwall contouring to reduce or eliminate the effects of secondary flow structures formed inside the turbine passage have been a topic of active research over the past decade, as many researchers have found that aerodynamic losses can be reduced to a significant extent [23-27] by effectively guiding the secondary flow through a preferred streamwise direction along the passage. However, there have been limited studies describing the effect of endwall contouring on heat transfer performance of a turbine passage. Saha and Acharya [28] published one of the pioneering studies on effect of non-axisymmetric contouring on endwall heat transfer. Their computational studies predicted an area averages Nusselt number reduction of 8% using a contoured endwall compared to a flat planar passage. Local heat transfer reduction close to three times near suction side of the passage was also reported. Piggush and Simon [29] investigated adiabatic effectiveness levels considering upstream and mate-face leakage flow for an axisymmetric contoured endwall. They discussed the effect of step orientation and its influence on the local boundary layer. However, no baseline case was performed for comparison. Lin and Shih [30] performed heat transfer measurements using endwall contouring upstream as well as a case where the contouring started upstream and continued along the passage. LaFleur et al. [31] reported 24% reduction in average endwall Stanton number using a contoured endwall compared to a flat baseline endwall. Lynch et al. [32] discussed the effects of endwall contouring on a LP turbine blade passage and compared heat transfer performance of the contoured endwall with a flat passage. They reported local augmentation levels close to 20% near the pressure side junction of the passage and

an overall heat transfer reduction of 3% while using the contoured endwall. Thrift et al. [33-34] performed extensive heat transfer and adiabatic effectiveness measurements on an axisymmetric contoured endwall of a nozzle guide vane. In all cases the contoured endwall showed lowest heat transfer levels. However, the heat transfer augmentation values decreased with increase in leakage flow due to intensification of the horse-shoe vortex.

MOTIVATION AND OBJECTIVE

All of the above mentioned heat transfer studies on endwall contouring were performed at very low exit Mach numbers and only Panchal et al. [21] has investigated the effect of endwall contouring on heat transfer performance at transonic operating conditions similar to those encountered in realistic modern engine environments. Panchal et al. [21] compared three different endwall geometries (two contoured and one baseline planar) and experimentally found out that the contoured endwalls (both aerodynamic and heat transfer optimized) performed significantly better in reducing average heat transfer coefficient values on the turbine passage. Any investigation on the effect of endwall contouring with leakage flow under transonic operating conditions does not exist in open literature.

The present study is a continuation and further development of Panchal et al. [21] introducing leakage flow aspects onto the baseline and aero-optimized (AO) endwall geometries for a high turning (127°), high pressure turbine passage operating at design exit Mach number - 0.88 and design incidence angle. The aero-optimized (AO) endwall was chosen between two endwall designs investigated by Panchal et al. [21] as AO design achieved better aerodynamic performance as well reducing overall loss coefficient at the cascade exit [35]. The inlet Mach number is 0.45 and inlet Reynolds number (based on axial chord length) is about 9 x 10^5. Heat transfer results are reported based on the effect of the purge flow, as well as effect of endwall contouring for different coolant to mainstream mass flow ratios (MFR) – 0.5%, 1.0% and 1.5%. The objective of the present study is to provide experimental data for film cooled endwall at transonic operating conditions in presence of endwall contouring and quantitative comparison of the heat transfer performance of the contoured endwall w.r.t to non-contoured conventional endwall geometry.

NOMENCLATURE

AO	Aero-Optimized
C_{ax}	Axial chord length (m)
h, HTC	Heat transfer coefficient $\left(\frac{W}{m^2K}\right)$
h_f	Heat transfer coefficient – Film Cooled case $\left(\frac{W}{m^2K}\right)$
h_{ref}	Heat transfer coefficient – Reference case $\left(\frac{W}{m^2K}\right)$

IR	Infrared
k	Thermal conductivity $\left(\frac{W}{m\,K}\right)$
M	Mach number
M_{iso}	Isentropic Mach number $M_{iso} = \sqrt{\left(\left(\frac{p_{0in}}{p_{s\,exit}}\right)^{\frac{\gamma-1}{\gamma}} - 1\right)\frac{2}{\gamma-1}}$
MFR	Mass flow ratio (coolant mass flow rate per passage/ mainstream mass flow rate per passage)
NHFR	Net Heat Flux Reduction
p_{0in}	Pitchwise average stagnation pressure at inlet midspan (Pa)
$p_{s\,exit}$	Pitchwise average static pressure on angled end wall 0.5 C_{ax} downstream of the trailing edge (Pa)
q''	Heat flux $\left(\frac{W}{m^2}\right)$
r	Recovery factor
t	Time (s)
T	Temperature (K or ^{o}C)
T_r	Recovery temperature (K or ^{o}C)
T_{ref}	Reference temperature (K or ^{o}C)
T_w	Wall temperature (K or ^{o}C)
T_i	Initial temperature (K or ^{o}C)
T_c	Coolant temperature (K or ^{o}C)
T_m	Mainstream temperature (K or ^{o}C)

Greek Letters

α	Thermal diffusivity $\left(\frac{m^2}{s}\right)$
φ	Overall Cooling effectiveness
γ	Ratio of specific heats
η, ETA	Film/Adiabatic Cooling effectiveness

Suffix

min	Minimum value
max	Maximum value

EXPERIMENTAL METHODOLOGY

Experimental Test Facility

A schematic of the transonic cascade wind tunnel at Virginia Tech is shown in Fig. 1. The wind tunnel is a blow down facility capable of a thirty second run time. The air supply is pressurized by a four-stage Ingersoll-Rand compressor and stored in large outdoor tanks. The maximum tank pressure used for transonic tests is about 2068 kPa (300psig). A control valve is used to regulate the flow from the tanks to the test section. During a run, the upstream total pressure is held constant by varying the opening of a butterfly valve controlled by a computerized feedback circuit. The airfoil isentropic exit Mach number is varied by changing the upstream total pressure. The airflow through the cascade is controlled valve 1 as shown in Fig. 1. The first and the second valve remain open during the aerodynamic measurements while the third one remains closed allowing the air flow directly from inlet to the test section. For the heat transfer experiments, the valves one and two are initially kept closed and the third one is kept open. Air is circulated through heater loop and the copper bars acting as thermal capacitor. The heated air from heater heats up copper tubes in the heat exchanger. The third valve is closed and the other two valves are opened when the temperature in the heat exchanger reaches a specified magnitude (100^{o}C). The air gets heated through the heat exchanger while passing from the inlet to the test section.

The cascade test section, as shown in Fig. 2, consists of 5 airfoils resulting in 4 passages, with a controlled bleed flow above the first airfoil. This passage design is identical to as reported in Panchal et al. [21], the 3rd passage from top is the passage of interest where all heat transfer measurements are carried out. The airfoils are mounted on a rotatable window, which allows for changes in incidence angles as and when required. All experiments were performed at design incidence angle, therefore cascade angle was fixed accordingly. Airfoil 3 from top is considered

as the center airfoil of the linear cascade. A headboard, positioned upstream of the cascade is instrumental in controlling the incoming flow by preventing an induced incidence angle effect on the leading edges of the airfoils.

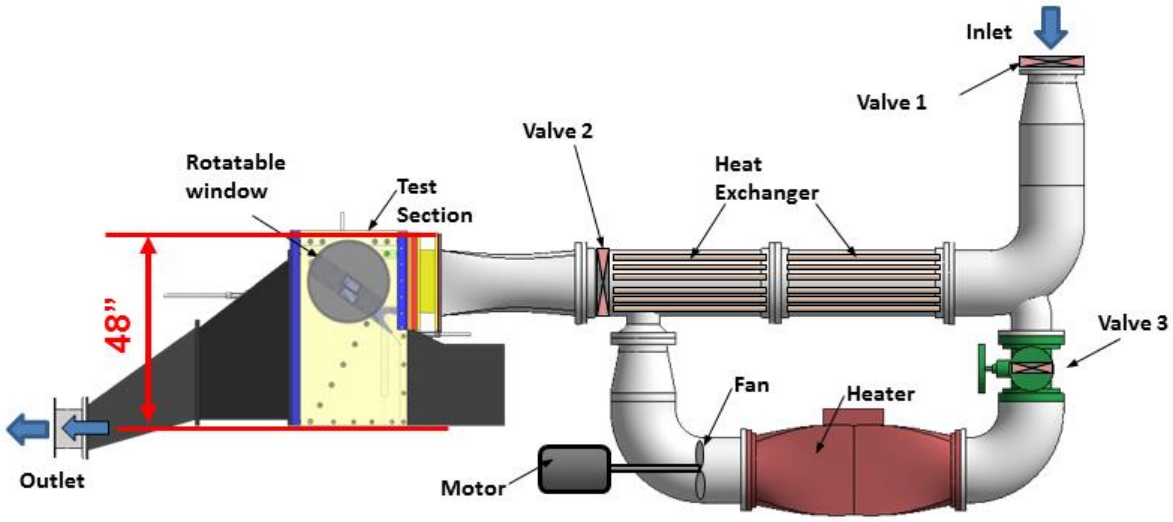

Figure 1: Virginia Tech transonic tunnel facility

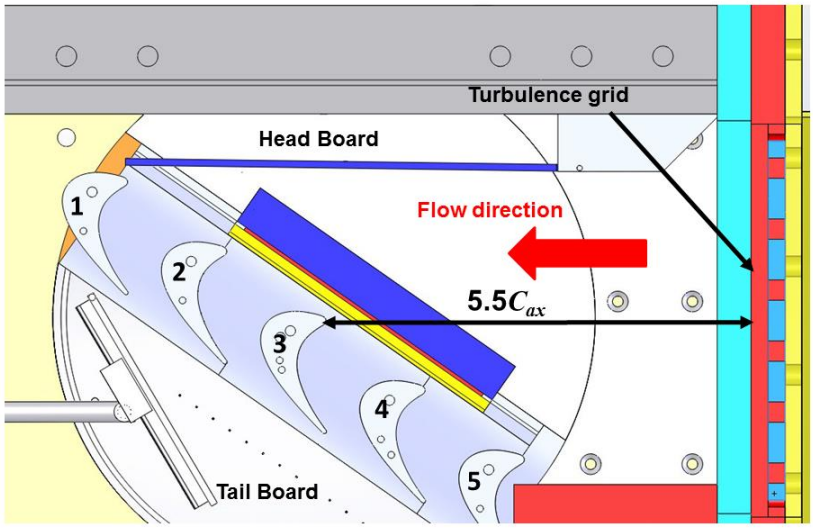

Figure 2: Cascade test section details with turbulence grid

The headboard is used to create and control a flow bleed that prevents the flow from turning prior to reaching the leading edge of the airfoils. Uniform inlet flow conditions can be achieved by careful adjustment of the headboard angle which aids in maintaining uniform and periodic flow through each airfoil passage and ensuring that the flow angle gradient ahead of the cascade is zero.

The inlet Mach number is measured by a Pitot static probe located 0.5 axial chords upstream of the center blade leading edge. The isentropic exit Mach number is decided based on the inlet total pressure (as measured by the pitot static probe) and the average wall static pressure measured 0.5 axial chords downstream of the cascade. The inlet total pressure profile was measured 0.5 C_{ax} upstream of the leading edge using 5 hole probe traverses in pitchwise direction at different span locations from the endwall up to the midspan. A turbulence grid is placed 5.5 C_{ax} upstream of the center blade as shown in Fig. 2. Inlet free stream turbulence intensity was measured at mid-span 0.5 C_{ax} upstream of the blade leading edge using a hot-wire anemometer and was found to be about 8%.

Purge Slot Design

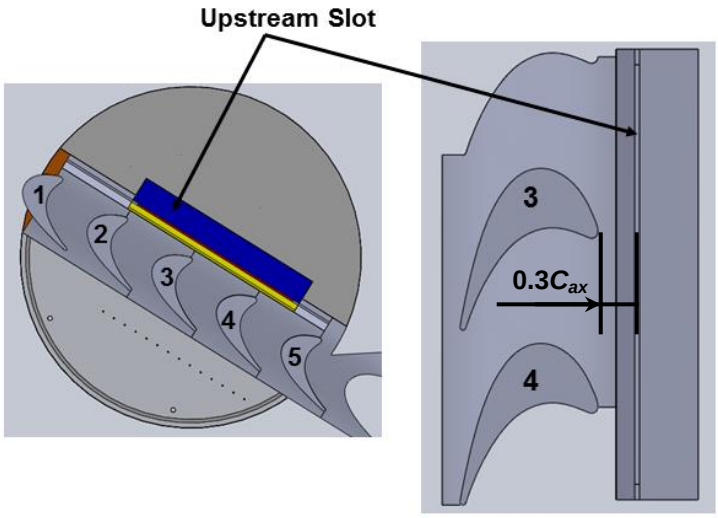

Figure 3: Cascade center part with upstream slot location

The upstream purge slot is located ~ 0.3 axial chord distance upstream of the leading edge of airfoil as shown in Fig. 3. The slot length was optimized to be ~ 2.6 pitch distance spaced in such a way such that the coolant flow pattern is periodic and wall effects can be safely neglected around the measurement passage. Internal features of the upstream leakage slot are also detailed. The coolant path through the slot is shown in Fig. 4 for clarity. Because of the ease with which complex geometries can be built in quick time at a fraction of the machining cost, all endwall and airfoil geometries were fabricated using ABS as the material in a rapid prototyping machine.

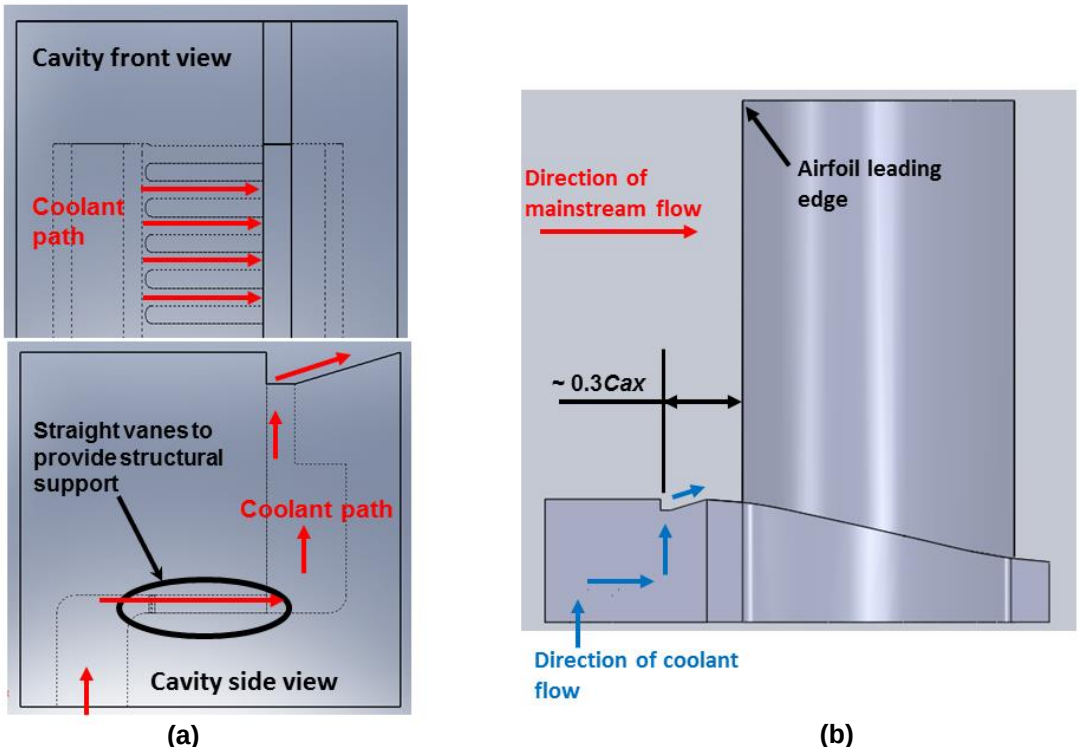

Figure 4: Purge slot design (a) internal details, (b) location of slot

Endwall Design

Two different endwall designs were studied for heat transfer performance in presence of upstream leakage slot. The endwall designs were provided by Siemens Energy, Inc. The first endwall geometry is non-contoured referred as Baseline endwall. The other endwall geometry denoted as AO (Aero-optimized) endwall was obtained from an optimization study in order to minimize aerodynamic losses at $1.0C_{ax}$ downstream of the airfoil trailing edge. The upstream purge slot design and dimensions were kept identical for both endwall geometries. The basic features of the contoured endwall geometry are shown in Fig. 5. The AO contoured endwall height is normalized w.r.t. baseline endwall which shows a strong peak region along the passage starting from the leading edge pressure side and a trough region along suction side starting ~ $0.2C_{ax}$ normal up to trailing edge. Further details of the design procedure and surface modification features are provided in Panchal et al. [21].

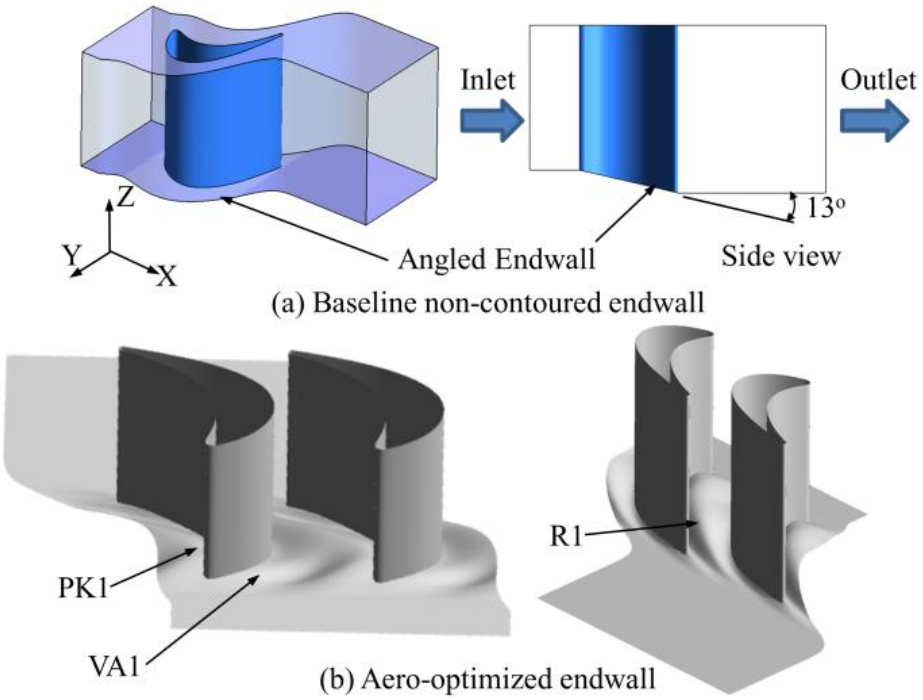

Figure 5: Endwall geometries

HEAT TRANSFER MEASUREMENT TECHNIQUE

Endwall surface temperature measurements were performed using an Infrared (IR) camera. Two IR transparent windows were added with a line of sight to the endwall surface being studied, as shown in Fig. 6(a). Due to the large forces seen in a transonic facility, the window also needed to be structurally sound. Two 4.5”x2.5” rectangular Zinc Selenide windows were used as to satisfy the design constraints. Only one window was used at a time for endwall temperature measurements while the other window was closed using a piece of lexan block. All the inner surfaces of the test section and outer surfaces of the test-section window were painted using a black paint to avoid thermal reflection from the surfaces. A rectangular coolant plenum was mounted to the test section window as seen in the rear view (Fig. 6(b)) to feed coolant into the upstream slot cavity. The coolant inlets to the plenum were from opposite directions in order to provide better coolant mixing and temperature uniformity. Coolant temperature was measured at a point inside the plenum where the coolant enters into the cavity.

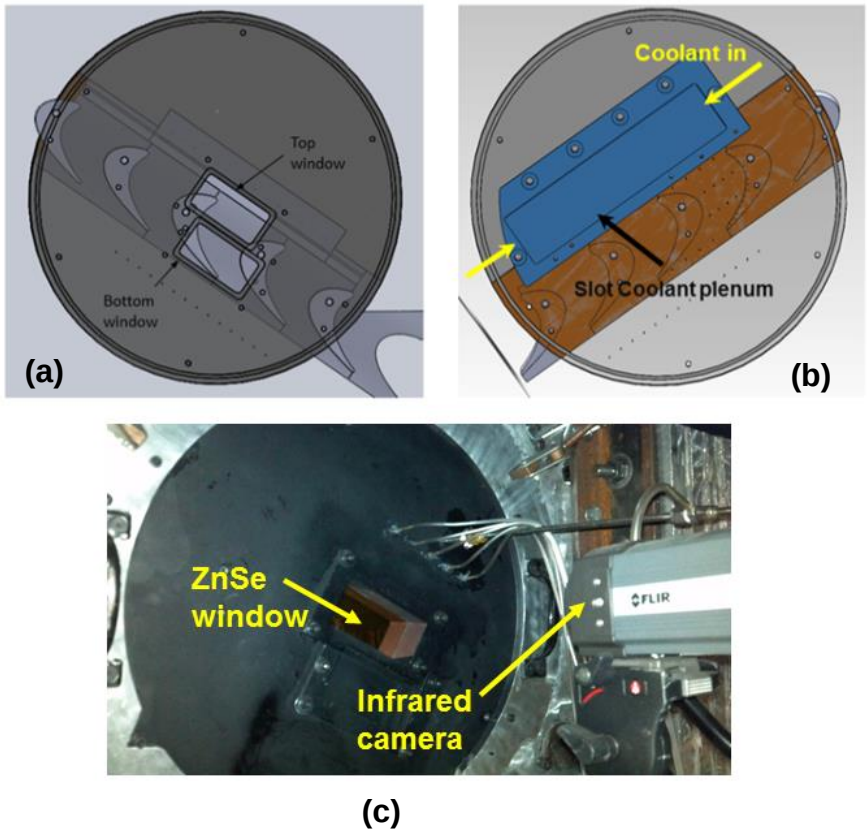

Figure 6: Heat transfer cascade set up (a) front window, (b) rear window, and (c) actual setup

The material of the endwall and the airfoils is Acrylonitrile butadiene styrene (ABS) that has low thermal conductivity. Since the reducible data is obtained only over a short duration (~ 5s), the thermal penetration length into the endwall in any direction is about 0.8mm. Other modes of heat transfer e.g. radiation can be safely neglected as the maximum operating range of the endwall surface temperatures is about 60^{o}C. The paint film thickness is so small (order of microns) compared to endwall dimensions, conduction in the transverse direction through the paint coating is assumed to be negligible. Therefore, the 1-D, semi-infinite heat transfer assumption is applicable at each location on the endwall. Moreover, significant cool down times in between runs were allowed so the endwall is at a uniform initial temperature at the start of every tunnel run. The IR camera used, ThermaCam SC325, at a resolution of 320x240, can measure 76800 surface temperature locations simultaneously with a 0.6mm x 0.6mm cross section for an individual pixel. Due to 1-D semi-infinite assumption results obtained for each individual pixel is assumed to be independent of the other.

The governing differential equation for 1D transient conduction along with initial and boundary conditions are expressed as,

$$\alpha \frac{\partial^2 T}{\partial x^2} = \frac{\partial T}{\partial t} \tag{1}$$

$t = 0$, $T = T_i$ (Initial Condition) (2)

$x = 0$, $T = T_w$ (Surface temperature boundary condition) (3)

$x \rightarrow \infty$, $T = T_i$ (Semi-infinite solid assumption) (4)

The convective heat flux at the surface can be defined as,

$$q'' = \left(T_m - T_w\right) \tag{5}$$

Uncooled heat transfer analysis

The mainstream fluid temperature (T_m) is replaced by local recovery temperature (T_r) considering compressible flow to account for aerodynamic heating near boundary layer.

Hence Eq. (5) is modified accordingly as shown,

$$q'' = h\left(T_r - T_w\right) \tag{6}$$

$$T_r = T_m \left(\frac{1 + r\left(\frac{\gamma - 1}{2}\right) Ma^2}{1 + \left(\frac{\gamma - 1}{2}\right) Ma^2} \right) \tag{7}$$

where, r = recovery factor = $Pr^{1/3}$ for turbulent boundary layer (Pr = Prandtl Number).

The calculation of surface heat flux is a two-step process where, in the first step, the conduction heat flux inside the solid material is calculated using a Finite Difference Method where Eq.(1)-(4) is solved using 2nd order discretization. The surface heat flux is thus computed from conduction analysis and is equal to the convective heat flux. The second step consists of for estimation of HTC, the calculation take place in the convective domain. However, the data processing time window can be chosen to avoid the transition period of the tunnel start, so that the HTC remains constant in the calculation. The data reduction time window of these two steps is shown in Fig. 7. The data reduction time window of curve fitting method is also shown on the same plot. The heat flux reconstruction needs the data from the tunnel start, because a uniform condition of the initial temperature in the material is necessary to solve Eq. (1)-(4).

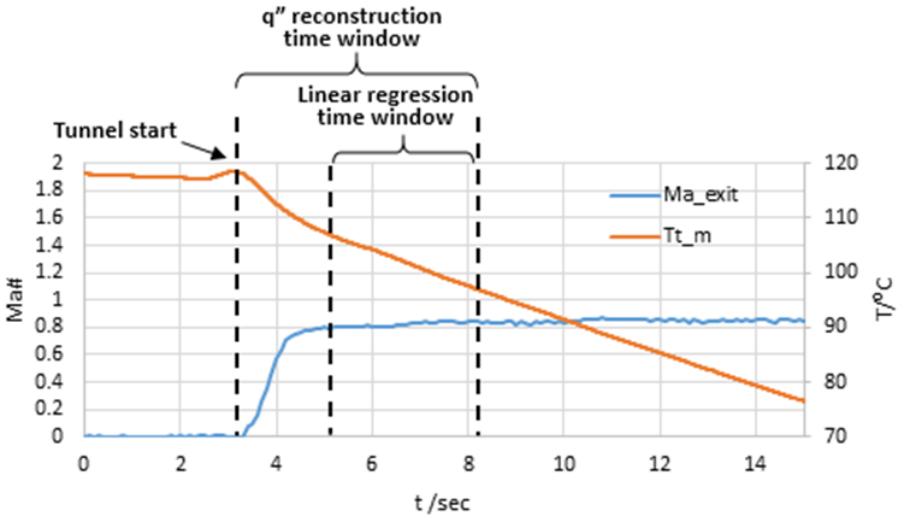

Figure 7: Tunnel temperature history and data processing window

Rearrange Eq. (6), we can get a linear relationship in the form,

$$q''(t) = h\left(T_m(t) - T_w(t)\right) + h\left(T_r(t) - T_m(t)\right) \tag{8}$$

The value of the last term in Eq. (8), only depends on the aerodynamic condition, and is constant as the local Mach number does not change within the calculation time window. Theoretically, all the data points should fall on a straight line, as shown in Fig. 8. The slope of this line is the HTC, and the recovery temperature can be estimated from the Y intercept.

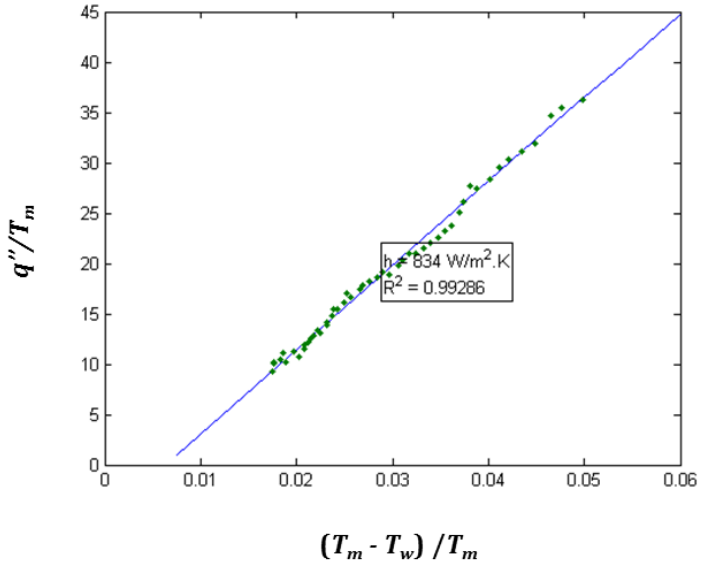

Figure 8: Linear regression plot for uncooled heat transfer

Film-cooled heat transfer analysis

However, for film cooling cases, where coolant is injected into the mainstream, T_m needs to be replaced by film temperature T_f which is a mixed intermediate temperature between mainstream and coolant governing the convective heat transfer to the surface wherever coolant film exists on the endwall. Therefore, all film cooling cases can be considered as three temperature problem involving mainstream (local recovery temperature), coolant and wall temperature. Adiabatic film cooling effectiveness (ETA) is a non-dimensional representation of T_f and is defined as,

$$\eta = \frac{T_r - T_f}{T_r - T_c} \tag{9}$$

Hence, the convective heat flux equation for film cooling cases is expressed as,

$$q'' = h\left(T_f - T_w\right) \tag{10}$$

Equation (10) can be algebraically manipulated to obtain the following expression,

$$\frac{q''}{T_r - T_c} = h\left(\frac{T_r - T_w}{T_r - T_c}\right) - h\eta \tag{11}$$

Since data is acquired during the steady period of the tunnel run, HTC and ETA can be assumed constant.

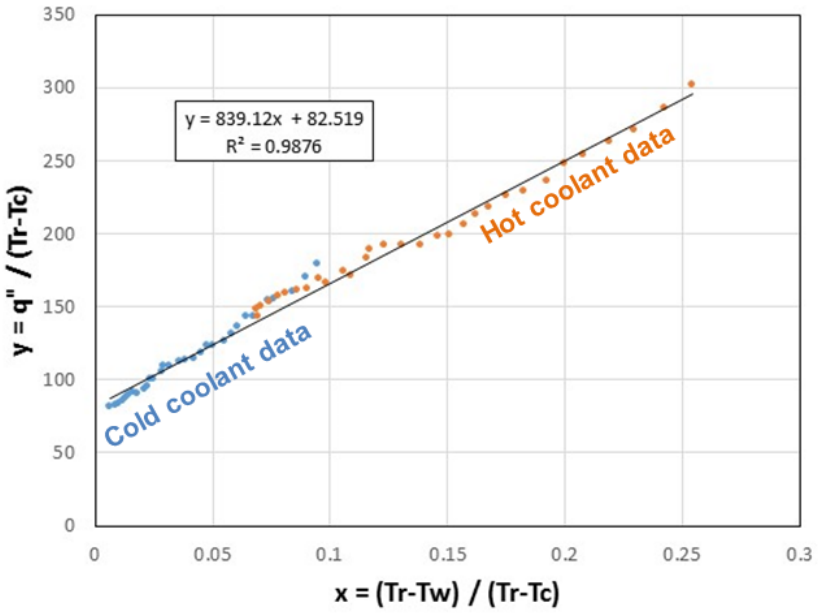

Figure 9: Linear regression curve fit for film cooled cases

Two similar transient tests are necessary in order to solve for HTC and ETA simultaneously. The experimental methodology of running two similar tests for film cooling cases has been adopted from Ekkad et al. [36] which is referred to as heated mainstream transient technique in section 3.2.1 of the article. The first transient test is carried out with mainstream at a high temperature and coolant at chilled temperatures (lower than ambient) and suddenly exposed to surface at ambient temperature. In the second test, the only difference is the coolant is heated up to a certain temperature instead of being cooled. The current method differs to some extent from the method described in Ekkad et al. [36], where for high speed flows coolant and mainstream temperatures cannot be matched and the mainstream cannot be continuously heated during experiments. Nevertheless, generating two different data sets from two similar transient runs provides enough points to solve the two unknowns iteratively. The basic assumption embedded into the data reduction technique is that HTC and ETA being hydrodynamic parameters, hence independent of operating temperatures, and experimental operating (flow) conditions remains same between "hot coolant" run and "cold coolant run". The T_r values are matched for both hot coolant run and cold coolant run as it depends on local Mach number and remains constant for a particular location during the data reduction period. The linear fit of data for film cooling cases is shown in Fig. 9 where, HTC is obtained from the slope and ETA is obtained from the Y-intercept.

Uncertainty Analysis

For linear regression technique, two different uncertainty analysis methods are applied in the two data processing steps respectively. The propagation of the major errors is analyzed through the Moffat's [37] perturbation method. The linear regression uncertainty analysis was carried out according to the method recommended by Brown and Coleman [38]. The average uncertainty for HTC measurements is about 8% whereas, for ETA values it is ~ 6%.

Data Representation

The basic data representation technique which involves mapping of two-dimensional raw HTC data onto three dimensional endwall surface using camera transformation matrix and image stitching was developed by Panchal et al. [21] and is not repeated here. This technique was further used for representing ETA values on a three-dimensional endwall similarly.

CFD ANALYSIS

A three-dimensional steady state, compressible flow CFD simulation was performed using commercial software package ANSYS-CFX® with SST k-ω turbulence model. The CFD modeling was performed by Siemens Energy Inc. The main flow passage had a structured grid with about 3.6 million cells resulting in Y+ values of less than 1.0 on all surfaces. The cavity mesh was also generated using a structured grid of similar quality and was attached to the flow domain with a GGI-direct interface.

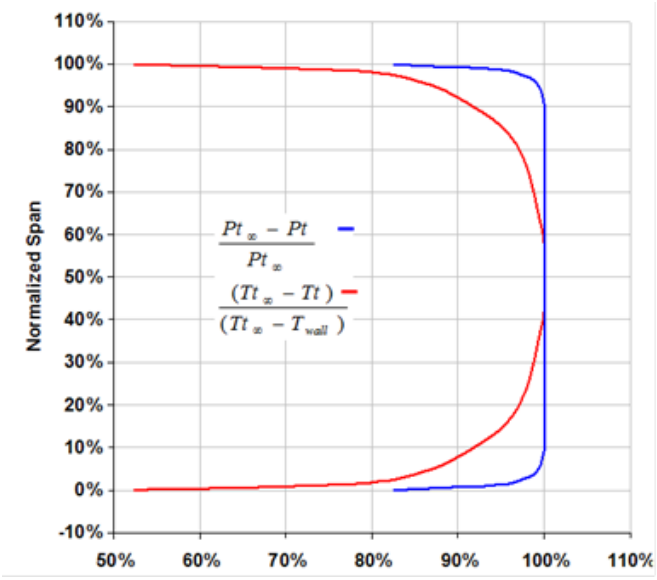

Figure 10: Inlet boundary layer profiles (obtained from experiments) used in the CFD simulation

At $0.5C_{ax}$ upstream, inlet T_t and P_t profiles derived from experimental data as shown in Fig. 10, were applied along with uniform unit vectors and 8% turbulence. At $2.0C_{ax}$ downstream, the outlet static pressure was varied to provide the airfoil loadings [35]. For further details on model development, readers are requested to contact co-authors from Siemens Energy Inc. directly due to proprietary reasons. It is important to note that, in this paper CFD simulations are used only to qualitatively compliment the experimental data and provide insight into the flow physics.

RESULTS AND DISCUSSION

The results discussed in this section are arranged in the following manner – First, the effect of presence of the upstream purge slot has been examined and compared with an existing case having no upstream slot, without coolant flow, Second, heat transfer characteristics have been elaborated for both endwall geometries corresponding to with (MFRs – 0.5%, 1.0%, and 1.5%) and without leakage flow cases. Finally, quantitative comparison between both endwall geometries has been described based on overall thermal performance. All heat transfer results shown in the following sections have been normalized (HTC normalized by area averaged HTC $1.0C_{ax}$ upstream of the slot and adiabatic effectiveness normalized by maximum value over the area) due to proprietary nature of the data. Experimental data for with and without coolant blowing cases are presented in the following sections.

Effect of upstream slot – without coolant blowing

Heat transfer experiments without the upstream slot have been carried out Panchal et al. [21]. During the experiments in presence of slot and without blowing, the exit of the slot was not sealed, therefore even if there was no net leakage flow, mainstream flow ingress into the cavity was present.

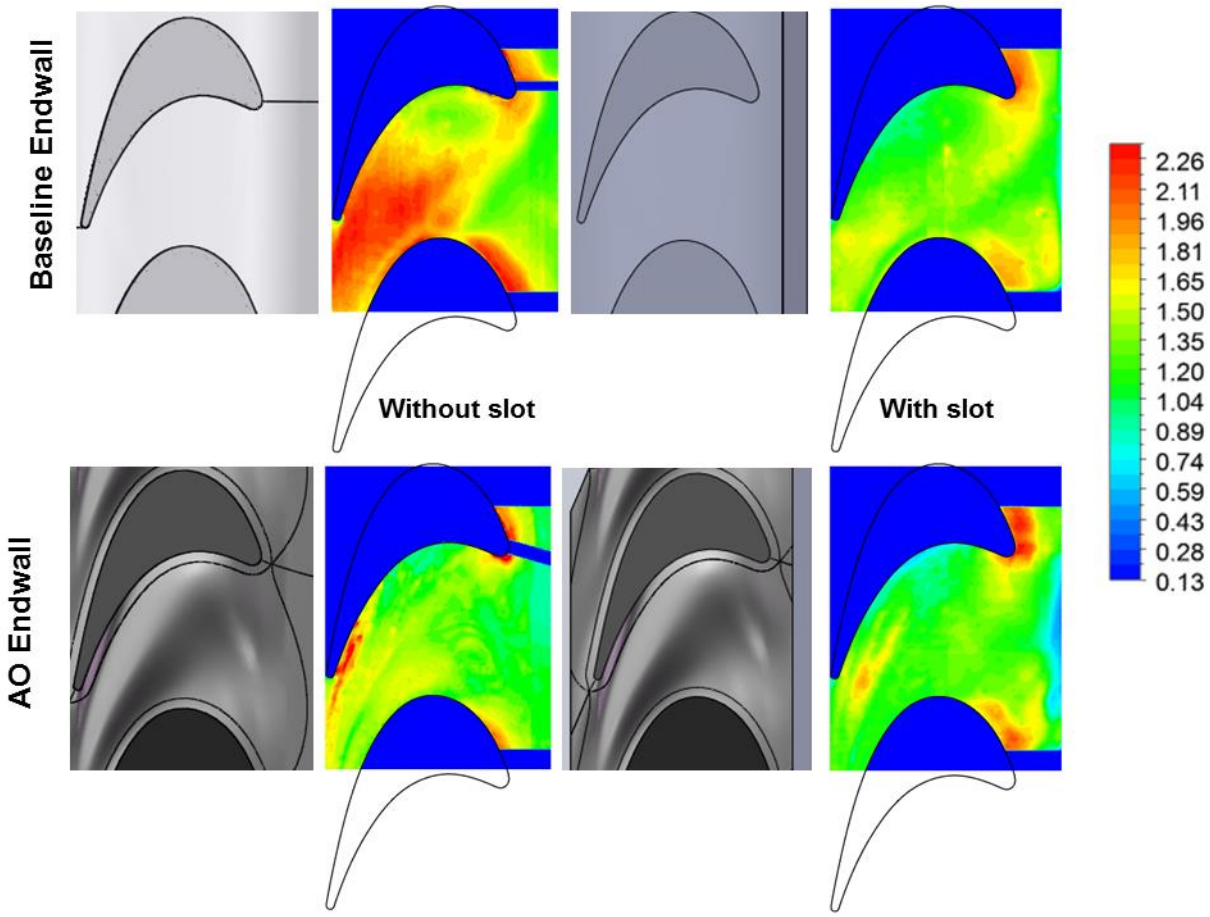

Figure 11: Normalized endwall heat transfer coefficient distribution with endwall contouring without coolant flow

Figure 11 shows the normalized endwall heat transfer coefficient distribution for the baseline and contoured (AO) endwall while uncooled heat transfer case has been considered. The absence of leakage flow emphasizes the effect of upstream backward facing slot on endwall heat transfer performance. The sole effect of the upstream purge slot on endwall contouring can be explained comparing Figs. 11(a)-(d) for baseline and AO geometry respectively. The complex vortices generated within the passage for the baseline geometry follows classical secondary flow pattern as explained by Wang et al. [38] and therefore is only discussed in brief and as follows.

In case of baseline geometry, the incoming boundary layer bifurcates at the stagnation point upstream of the leading edge of the airfoil and forms a horse-shoe vortex. The pressure side leg of the horse-shoe vortex traverses further inside the passage and grows in strength as it mixes with the mainstream flow. The cross passage pressure differential formed between pressure side of one airfoil and suction side of the adjacent airfoil drives the passage vortex towards suction side of the airfoil, where it meets with the suction side leg of the horse-shoe vortex and lifts off from the endwall. The corner vortex adheres and grows along the suction side of the airfoil up to the trailing

edge. Thereafter, the passage vortex grows further towards the trailing edge adhering to the suction side of the airfoil. Figure 12 shows endwall flow features observed after an oil flow visualization experiment was performed on the baseline endwall. The horse-shoe vortex, passage vortex formation and propagation, separation and re-attachment lines are clearly visible.

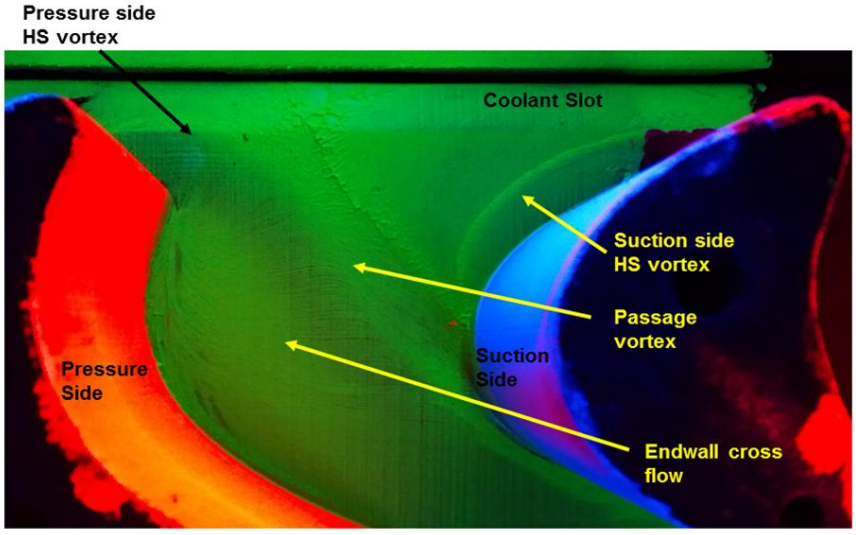

Figure 12: Baseline endwall oil flow visualization

The AO endwall passage contour is designed to redirect the pressure side leg of the horse-shoe vortex along more favorable streamwise direction. The protruded region on AO endwall starting from the leading edge of the airfoil extending towards the suction side prohibits the passage vortex from cutting across the passage even in presence of large pressure gradient. Therefore, the passage vortex remains weaker compared to baseline endwall as it is prevented to mix with the mainstream flow and influence of cross passage pressure differential is minimum. The peak region guides the passage vortex primarily along the pressure side of the airfoil and therefore meets the suction side leg of horse-show vortex further downstream compared to baseline endwall. The path and strength of the passage vortex strongly influence endwall heat transfer. Therefore, it is important to note that local HTC values are dependent on flow features near the endwall, hence increased HTC levels are observed in locations where the vortices are stronger. Figure 13 shows CFD prediction of endwall static pressure distribution superimposed with vortex cores. All vortex cores are iso-surfaces of identical strength. Therefore, a stronger vortex can be identified with a larger core radius. Comparing Figs. 11 and 13 it can be inferred that regions with low pressure and high velocity strengthen the passage vortex, resulting in higher convective heat transfer. Similarly, high heat transfer zone can is also observed at the leading edge stagnation point neat the formation of horse-shoe vortex.

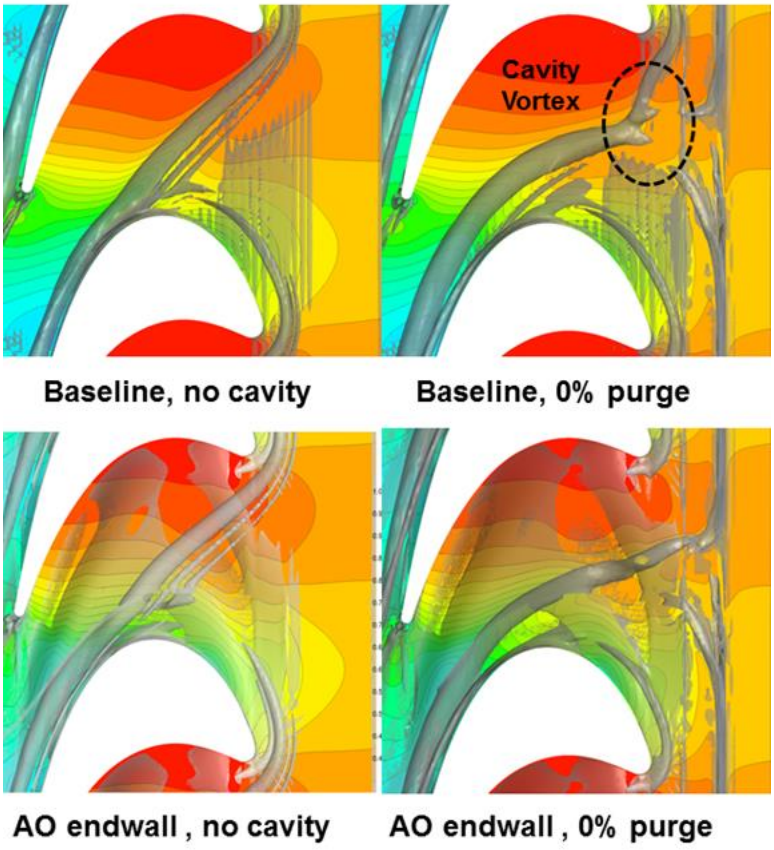

Figure 13: Endwall flow structure with vortex cores using CFD

The presence of the purge slot upstream of the airfoils doesn't change the overall endwall flow patterns for both baseline and AO endwall. However significant reduction of HTC values is observed compared to without slot case. A new vortex structure can be identified which is known as the "cavity vortex". This vortex forms due to mainstream flow ingress into the cavity. Since, the lift-off point of the passage vortex is further upstream in presence of a slot, the overall strength of the pressure side leg of horse-shoe vortex diminishes resulting in lower endwall heat transfer. Therefore the major difference in HTC distribution between with and without slot case can be attributed due to reduced strength of the horse-shoe vortex, as the purge slot trips the inflow boundary layer. For AO geometry, further reduction of endwall HTC is obtained due to the contour guiding the passage vortex primarily along pressure side of airfoil and delaying the meeting point with suction side leg of horse-shoe vortex.

Effect of endwall contouring with coolant injection

Figure 14 illustrates normalized endwall HTC distribution for film cooling cases where three coolant to mainstream mass flow ratios (MFRs) have been considered for both endwall geometries – 0.5%, 1.0% and 1.5%. Prominent interaction between coolant and secondary flow features is observed for both baseline and AO endwall

geometry. The purge flow from the upstream slot follows the path traversed between the pressure side leg of the horse-shoe vortex and suction side horse-shoe vortex of the adjacent airfoil and gets mixed out into the mainstream flow. The extent of coolant jet penetration and diffusion into the passage mainstream flow is found to increase with increase in coolant MFRs. Moreover, a local high HTC zone (Region A) can be identified upstream of the airfoils near the chamfer region especially for baseline geometry at higher MFRs. Region A is highly affected by turbulent dissipation and mixing of coolant jet into the mainstream – higher the coolant momentum flux, higher is the rate of dissipation and therefore resulting in concentrated high heat transfer zones expanding with increasing MFR. Strengthening of the "Slot induced coolant vortex" imparting additional coolant momentum flux can also be attributed towards higher HTC values in Region A. The coolant vortex is a stronger version of the cavity vortex explained earlier due to coolant addition. Enhancement of local endwall heat load due to coolant jet mixing is also seen in contoured geometry as shown in Fig. 14. However, the region is shifted more downstream compared to non-contoured baseline endwall and for higher MFR (1.5%) condition higher coolant significantly reduces heat load within that region.

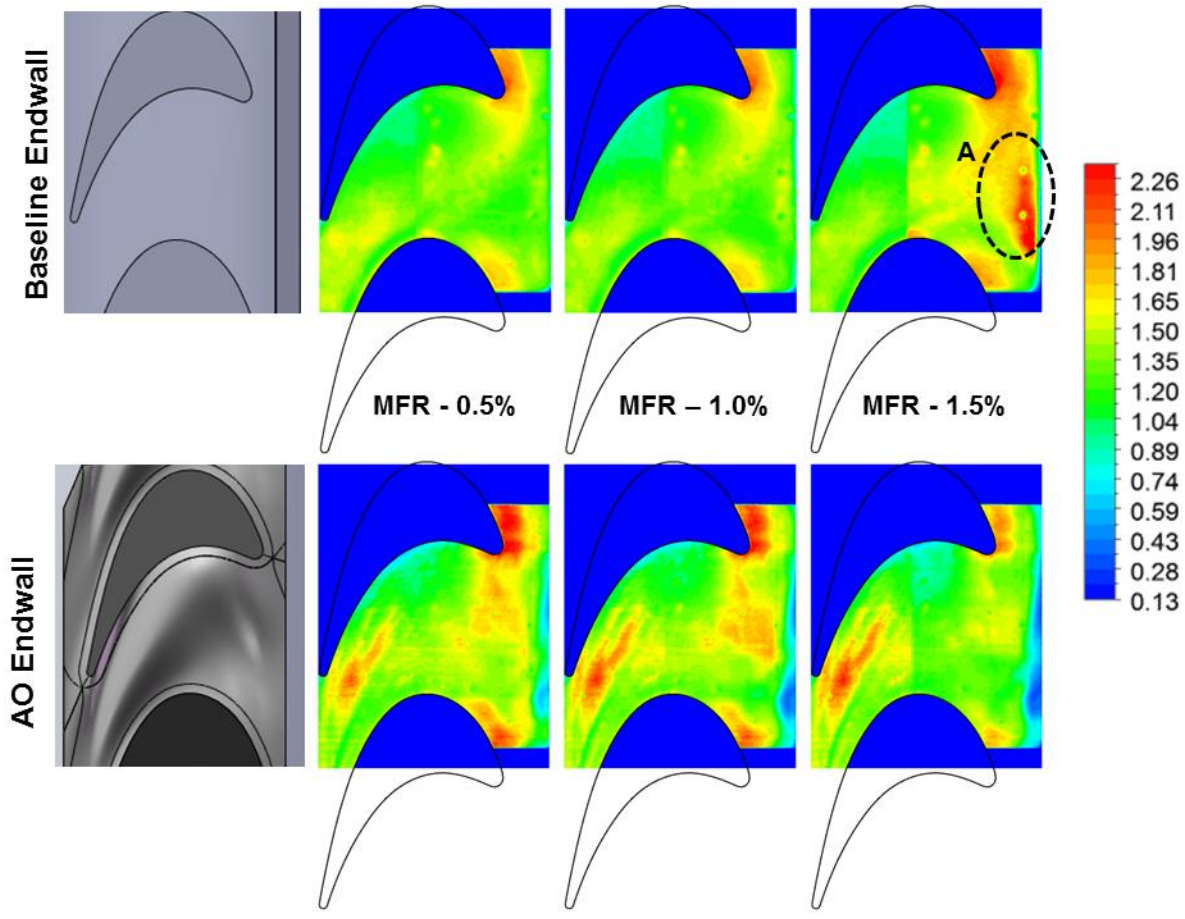

Figure 14: Normalized heat transfer coefficient distribution – upstream purge flow cases

Considering baseline endwall, as shown in Fig. 15, it can be noted that as the upstream leakage flow is increased from the coolant further progresses into the passage. At 0.5% MFR the coolant momentum flux is low, hence diffuses rapidly and is not able to penetrate significantly into the passage. For 1.0% MFR and 1.5% MFR the coolant acquires higher momentum flux and hence is able to penetrate further into mainstream flow. The V-shaped effectiveness contours near the leading edge for higher coolant MFRs lies between the horse-shoe vortices of adjacent airfoils for baseline geometry. The cross passage pressure differential between the airfoils drives the coolant more towards the suction side of the airfoil. It can also be observed that with higher MFR, better cooling be obtained near leading edge stagnation region. However for 1.5% MFR case the coolant spread is not significantly higher along the mainstream direction compared to 1.0% due to coolant lift off from the endwall. The coolant lift off phenomenon can also be supported from HTC contours at 1.5% MFR case as shown in Fig. 14, where, very high local heat transfer zone exists due to enhanced turbulence mixing of coolant jet with mainstream flow.

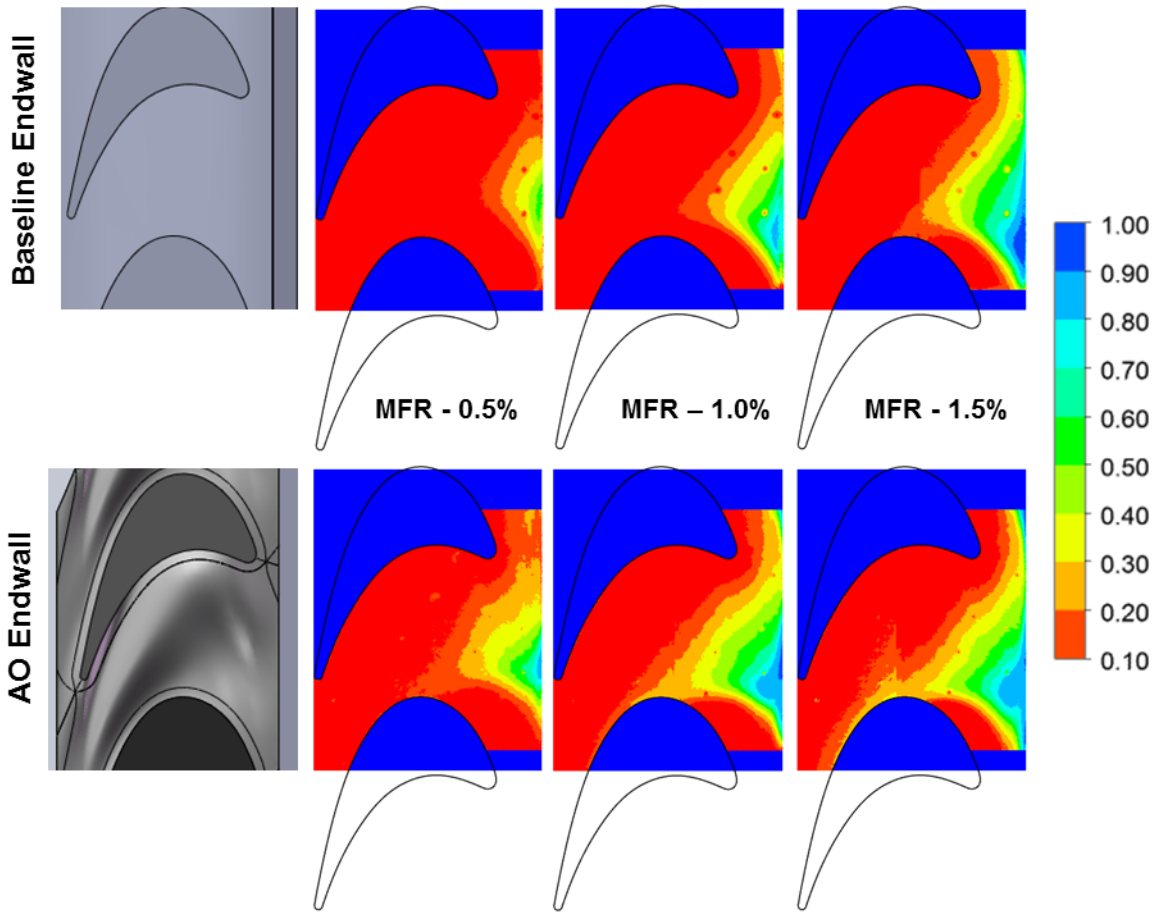

Figure 15: Normalized endwall adiabatic effectiveness contours

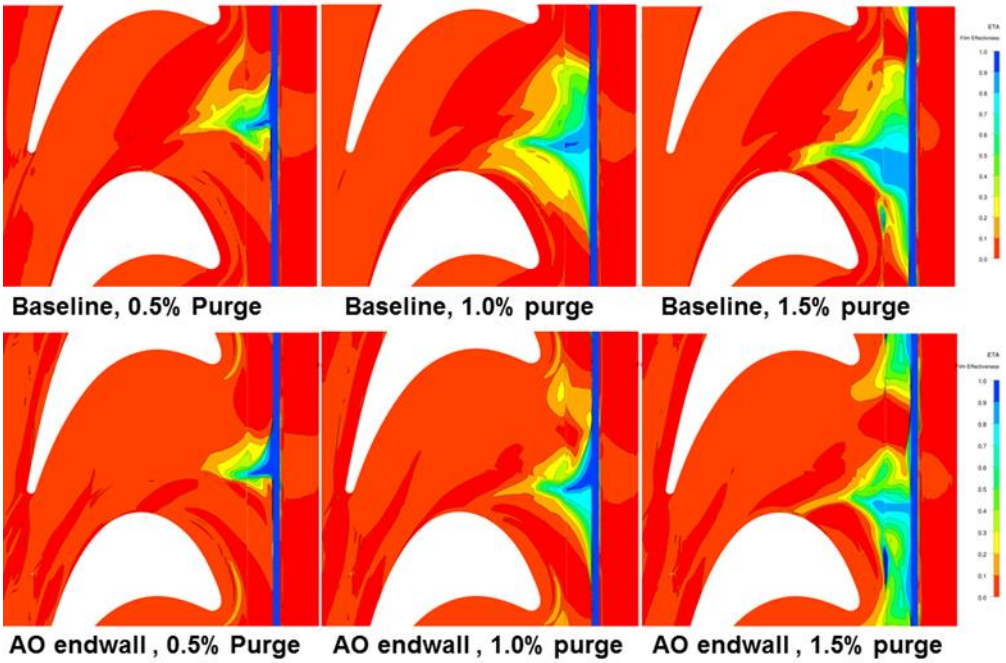

Figure 16: Normalized endwall adiabatic effectiveness contours – CFD prediction

Furthermore, Fig. 15 also illustrates that for AO endwall the coolant effectiveness spread is higher towards the streamwise direction and also around suction side of the airfoils compared to baseline geometry especially for higher coolant MFRs, however cooling near the leading edge upstream region is better in case of baseline geometry. This is attributed due to the effect of contouring which helps the coolant to adhere to the endwall further downstream of the passage.

Figure 16 shows predicted effectiveness contours obtained using CFD analysis for different coolant MFRs with endwall contouring and are in good qualitative agreement with experimental results. Due to the formation of the passage vortices as described earlier, CFD results also show that the extent of the purge flow is contained within the triangular region upstream of the horse-shoe vortex. With increase in coolant MFR, the coverage expands outward, but is not able to reach the leading edge or beyond the horse-shoe. However, the experimental data shows higher effectiveness levels towards trailing edge along suction side for higher MFR.

Table 1 presents a summary of comparative performance of endwall heat transfer for all with and without film cooling cases. Area averaged endwall HTC has been considered as the basis for comparison with Baseline endwall without coolant (with slot) as the reference. It can be emphasized again, that significant reduction in endwall heat transfer performance can be obtained only due to the presence of upstream slot. Considering film cooling cases at 0.5% and 1.0% MFR although the overall HTC values are higher for AO geometry, however, significant heat flux reduction can be achieved as the effectiveness levels are higher than corresponding baseline cases. At 1.5% MFR,

AO endwall performance is better as the contouring helps the coolant film to be attached to the surface whereas, jet lift off occurs in case of baseline endwall.

Table 1: Area averaged heat transfer coefficient comparison

	No slot	No coolant – with slot	MFR – 0.5%	MFR – 1.0%	MFR – 1.5%
Baseline	+ 24%	-	- 1%	- 4%	+ 5%
AO	+ 5%	-7%	+ 4%	+ 3%	- 4%

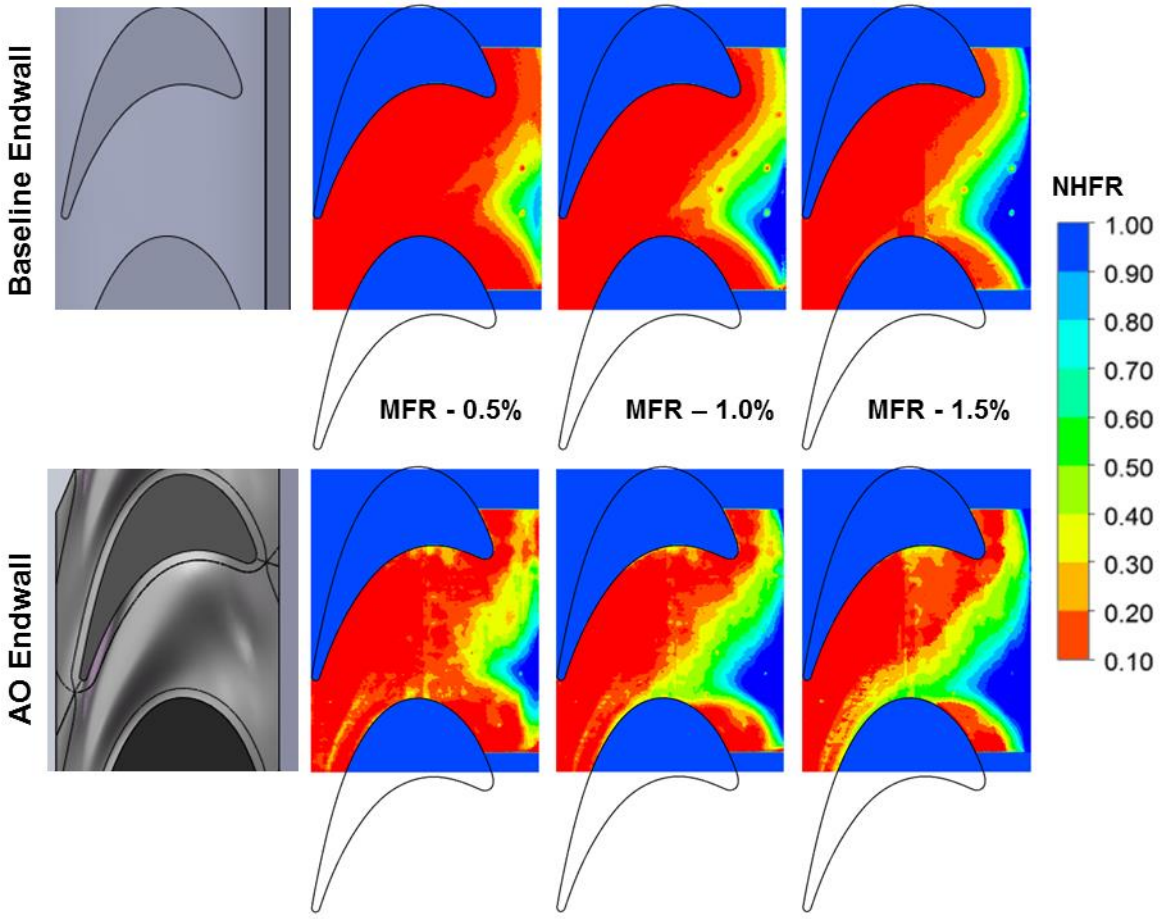

Figure 17: Local Net Heat Flux Reduction (NHFR) distribution for all leakage cases

Net Heat Flux Reduction (NHFR) analysis has also been carried out to further identify the benefits of using endwall contouring as depicted in Fig. 17. NHFR – a combination of HTC and ETA, the analytical expression of which is provided in Eq. (12), is used widely in literature to figure out the overall performance enhancement in presence of cooling features compared to a non-blowing reference case (Baseline geometry without net upstream purge flow).

$$\text{NHFR} = 1 - \frac{h_f}{h_{ref}}\left(1 - \frac{\eta}{\varphi}\right) \quad (12)$$

Where, φ is a non-dimensional metal temperature defined as overall cooling effectiveness and an average value of φ = 0.6 is used considering realistic gas turbine inlet, metal and coolant temperatures [40]. It is evident from Fig. 17 that the contoured endwall significantly improves endwall NHFR due to the combination of the following – 1) effective control of the secondary flow reducing the passage vortex strength and strong cross passage flow gradients and 2) the coolant film can penetrate further into the passage almost up to the trailing edge for higher MFR. The major contributor towards pressure side NHFR is due to reduction in local HTC. However, effect of coolant film coverage is dominant towards suction side of the platform as well as the region just downstream of the slot within the stagnation zone.

CONCLUSIONS

Heat transfer performance of a non-axisymmetric contoured (AO) endwall generated to minimize aerodynamic losses was experimentally investigated and compared with a conventional planar (baseline) endwall at three different leakage flow rates (0.5%, 1.0% and 1.5% MFR) at design exit isentropic Mach number of 0.88 and design incidence angle using IR thermography technique.

- The presence of purge slot has a significant impact on endwall heat transfer distribution. 19% area averaged heat transfer coefficient reduction was observed for baseline endwall, whereas, in case of contoured endwall the reduction was 11% when without and with purge slot (without coolant) cases are compared.

- The contoured endwall shows significant improvement over heat transfer performance for all uncooled heat transfer cases. However, the area averaged Nusselt number reduction is comparatively lower in presence of slot. This may be attributed due to the design procedure of the contoured endwall. The contoured endwall geometry was generated to minimize the aerodynamic losses without taking into account the presence of the slot, therefore, presence of the slot might have an impact on the overall performance.

Considering film cooling cases, although the area averaged Nusselt number for contoured endwall is marginally higher than baseline counterpart for low (0.5%) to moderate (1.0%) coolant MFRs, the higher effectiveness levels may reduce the overall passage heat load onto the hub. This was evident considering local NHFR as an overall comparison basis. The contoured endwall outperforms the baseline geometry in significant reduction of heat load especially near the conventional hot-spot regions. Improvement near the pressure side is largely due to reduced HTC levels however, suction side NHFR is largely contributed by adiabatic effectiveness. At higher MFR (1.5%) the contouring helps the coolant film to stay attached to the endwall surface for a longer distance along the mainstream flow, therefore, larger coolant spread is achievable in case of contoured endwall. The coolant lift off at higher MFRs is due to intense turbulent mixing for baseline endwall increases overall Nusselt number as well as decreasing the coolant spread on the surface.

ACKNOWLEDGEMENTS

The authors would like to acknowledge the funding support from the US Department of Energy through Siemens Energy, Inc. This material is based upon work supported by the US Department of Energy under Award Number DE-FC26-05NT42644.

REFERENCES

[1] Han, J.C., Dutta, S., and Ekkad, S.V., 2000, *Gas Turbine Heat Transfer and Cooling Technology*, Taylor & Francis, New York.

[2] Dunn, M.G., 2001, Convective Heat Transfer and Aerodynamics in Axial Flow Turbines, J. Turbomachinery, 123, pp. 637-686

[3] Chyu, M.K., 2001, "Heat Transfer Near Turbine Nozzle Endwall", Ann. N.Y. Acad. Sci., 934, pp. 27-36.

[4] Simon, T.W., and Piggush, J.D., 2006, "Turbine Endwall Aerodynamics and Heat Transfer", AIAA J., 22(2), pp. 301-312.

[5] Blair, M.F., 1974, "An Experimental Study of Heat Transfer and Film Cooling on Large-Scale Turbine Endwalls", ASME J. Heat Transfer, 96, pp. 524-529.

[6] Graziani, R.A., Blair, M.F., Taylor, J.R., and Mayle, R.E., 1980, "An Experimental Study of Endwall and Airfoil Surface Heat Transfer in a Large Scale Turbine Blade Cascade", ASME J. Eng. Power, 102, pp. 257-267.

[7] Colban, W.F., Thole, K.A., and Zess, G., 2002, "Combustor-Turbine Interface Studies: Part 1: Flow and Thermal Field Measurements", J. Turbomachinery, 125, pp. 203-209.

[8] Zhang, L., and Moon, H.K., 2003, "Turbine Nozzle Endwall Inlet Film Cooling – The Effect of a Back-Facing Step", ASME Paper No. GT2003-38319.

[9] Oke, R., and Simon, T., 2002, "Film Cooling Experiments with Flow Introduced Upstream of a First Stage Nozzle Guide Vane Through Slots of Various Geometries", ASME Paper No. GT2002-30169.

[10] Papa, M., Srinivasan, V., and Goldstein, R.J., 2012, "Film Cooling Effect of Rotor-Stator Purge Flow on Endwall Heat/Mass Transfer", J. Turbomachinery, 134(4), pp. 041014-1-8.

[11] Goldstein, R.J., and Spores, R.A., 1988, "Turbulent Transport on the Endwall in the Region Between Adjacent Turbine Blades", J. Heat Transfer, 110, pp. 862-869.

[12] Knost, D.G., and Thole, K.A., 2005, "Adiabatic Effectiveness Measurements of Endwall Film-Cooling for a First-Stage Vane", J. Turbomachinery, 127, pp. 297-305.

[13] Ranson, W.W., Thole, K.A., and Cunha, F.J., 2005, "Adiabatic Effectiveness Measurements and Predictions of Leakage Flows Along a Blade Endwall", J. Turbomachinery, 127, pp. 609-618.

[14] Cardwell, N.D., Sundaram, N., and Thole, K.A., 2006, "Effect of Midpassage Gap, Endwall Misalignment, and Roughness on Endwall Film-Cooling", J. Turbomachinery, 128, pp. 62-70.

[15] Wright, M.L., Gao, Z., Yang, H., and Han, J.C., 2008, "Film Cooling Effectiveness Distribution on a Gas Turbine Blade Platform With Inclined Clot Leakage and Discrete Film Hole Flows", J. Heat Transfer, 130, pp. 071702-1-11.

[16] Gao, Z., Narzary, D., and Han, J.C., 2009, "Turbine Blade Platform Film Cooling With Typical Stator-Rotor Purge Flow and Discrete-Hole Film Cooling", J. Turbomachinery, 131, pp. 041004-1-11.

[17] Giel, P.W., Thurman, D.R., Van Fossen, G.J., Hippensteele, A.A., and Boyle, R.J., 1998, "Endwall heat transfer measurements in a transonic turbine cascade", J. Turbomachinery, 120, pp. 305-313.

[18] Nicklas, M., 2001, "Film-Cooled Turbine Endwall in a Transonic Flow Field: Part II – Heat Transfer and Film Effectiveness", J. Turbomachinery, 123, pp. 720-729.

[19] Jonsson, M., Charbonnier, D., Ott, P., and von Wolfersdorf, J., 2008, "Application of the transient heater foil technique for heat transfer and film cooling effectiveness measurements on a turbine vane endwall", ASME Paper No. GT2008-50451.

[20] Vogel, G., Wagner, G., and Bolcs, A., 2002, "Transient Liquid Crystal Technique combined with PSP for Improved Film Cooling Measurements", The 10th Int. Symp. Flow Visualization, Kyoto, Japan, F0109.

[21] Panchal, K.V., Abraham, S., Ekkad, S.V., Ng, W.F., Lohaus, A.S., and Crawford, M.E., 2012, "Effect of endwall contouring on a transonic turbine blade passage: Part 2 – Heat transfer performance", ASME Paper No. GT2012-68405.

[22] Salvadori, S., Ottanelli, L., Jonsson, M., Ott, P., and Martelli, F., 2012, "Investigation of High-Pressure Turbine Endwall Film Cooling Performance Under Realistic Inlet Conditions", J. Propulsion and Power, 28(4), pp. 799-810.

[23] Harvey, N.W., Rose, M.G., M. D., Shahpar, S., Hartland, J., Gregory-Smith, D. G., "Nonaxisymmetric turbine end wall design: Part I- three-dimensional linear design system," *ASME Journal of Turbomachinery*, Vol. 122, April 2000, pp. 278-285.

[24] Hartland, J. C., Gregory-Smith, D. G., Harvey, N. W., Rose, M. G., " Nonaxisymmetric turbine end wall design: Part II – Experimental validation," *ASME Journal of Turbomachinery*, Vol. 122, April 2000, pp. 286-293.

[25] Knezevici, D. C., Sjolander, S. A., Praisner, T. J., Allen-Bradley, E., and Grover, E. A., "Measurements of Secondary Losses in a Turbine Cascade With the Implementation of Non-Axisymmetric Endwall Contouring," *Proceedings of ASME Turbo Expo* 2008, Paper No. GT2008-51311.

[26] Gustafson, R., Mahmood, G., Acharya, S., "Aerodynamic measurements in a linear turbine blade passage with three-dimensional endwall contouring," *Proceedings of ASME Turbo Expo* 2007, May 14-17, Montreal, Canada, Paper no. GT2007-28073.

[27] Rose, M. G., Harvey, N. W., Seaman, P., Newman, D. A., McManus, D., "Improving the efficiency of the Trent 500 HP turbine using non-axisymmetric end walls. Part II- Experimental Validation", *International Gas Turbine & Aero engine Congress & Exhibition*, June 4-7, 2001, New Orleans, LA, Paper no. 2001-GT-505.

[28] Saha, A. K., Acharya, S., "Computations of turbulent flow and heat transfer through a three-dimensional non-axisymmetric blade passage," *Proceedings of ASME Turbo Expo* 2006, May 8-11, Barcelona, Spain, Paper no. GT2006-90390.

[29] Piggush, J. D., and Simon, T. W., "Heat Transfer Measurements in a First Stage Nozzle Cascade Having Endwall Contouring, Leakage and Assembly Features," *ASME Summer Heat Transfer Conference*, July 17-22, 2005, San Francisco, California, Paper No. HT2005-72573.

[30] Lin, Y.-L., Shih, T. I.-P., and Simon, T. W., 2000, "Control of Secondary Flows in a Turbine Nozzle Guide Vane by Endwall Contouring," *Proceedings of ASME Turbo Expo* 2000, Paper No. GT2000- 556.

[31] LaFleur, R. S., Whitten, T. S., Araujo, J. A., "Second vane endwall heat transfer reduction by endwall contouring," *International gas turbine & aeroengine congress & exhibition*, Indianapolis, Indiana, June 7-10, 1999, Paper 99-GT-422.

[32] Lynch, S. P., Sundaram, N., Thole, K. A., Kohli, A., Lehane, C., "Heat transfer for a turbine blade with non-axisymmetric endwall contouring", *ASME Journal of Turbomachinery*, 2011, Vol. 133, pp. 011019-1-011019-9.

[33] Thrift, A.A., Thole, K. A., Hada, S., "Effects of an Axisymmetric Contoured Endwall on a Nozzle guide Vane: Convective Heat Transfer Measurements", *ASME Journal of Turbomachinery*, 2011, Vol. 133, pp. 041008-1-041008-10.

[34] Thrift, A.A., Thole, K. A., Hada, S., "Effects of an Axisymmetric Contoured Endwall on a Nozzle guide Vane: Adiabatic Effectiveness Measurements", *ASME Journal of Turbomachinery*, 2011, Vol. 133, pp. 041007-1-041007-10.

[35] Abraham, S., Panchal, K.V., Ekkad, S.V., Ng, W.F., Lohaus, A.S., and Malandra, A., 2012, "Effect of endwall contouring on a transonic turbine blade passage: Part 1 – Aerodynamic performance", *Proceedings of ASME Turbo Expo* 2012, ASME Paper No. GT2012-68425.

[36] Ekkad, S.V., and Han, J.C., "A transient liquid crystal thermography technique for turbine heat transfer measurements", *Measurement. Science and Technology*, 2000, Vol. 11, pp. 957-968.

[37] Moffat, R. J., 1988, "Describing Uncertainties in Experimental Results," Exp. Thermal and Fluid Science, 1, pp. 3-17.

[38] Coleman, H. W., Brown, K. H., and Steele, W. G., 1995, "Estimating Uncertainty Intervals for Linear Regression," AIAA-1995-0796.

[39] Wang, H.P., Olson, S.J., Goldstein, R.J., and Eckert, E.R.G., *Flow Visualization in a Linear Turbine Cascade of High Performance turbine blades*, ASME J. of Turbomachinery, **119**, pp. 1-8.

[40] Mick W.J., Mayle R.E.,1988, "Stagnation film cooling and heat transfer, including its effect within the hole pattern", J. Turbomachinery,110,pp.61-70.

CHAPTER 2 : Convective Heat Transfer Measurements in a Transonic Turbine Blade Passage with Discrete Hole Cooling and Endwall Contouring

CONVECTIVE HEAT TRANSFER MEASUREMENTS IN A TRANSONIC TURBINE BLADE PASSAGE WITH DISCRETE HOLE COOLING AND ENDWALL CONTOURING

Arnab Roy, Dorian M. Blot, Srinath V. Ekkad, Wing F. Ng
Department of Mechanical Engineering, Virginia Tech
Blacksburg, Virginia, USA

Andrew S. Lohaus, Michael E. Crawford
Siemens Energy, Inc.
Orlando, Florida, USA

To be submitted to ASME Journal of Thermal Sciences and Engineering Applications

ABSTRACT

Heat transfer experiments with endwall discrete hole film cooling were carried out for a high turning (127°) airfoil passage in presence of an upstream purge slot in a transonic linear cascade. However, no leakage flow from the purge slot was considered in this study. Two different coolant to mainstream mass flow ratios (MFR) – 0.15% and 0.25% were investigated at design exit Mach number (0.88) and design incidence angle. Measurements with identical operating conditions were performed using two passage designs – 1) a planar endwall (Baseline), and 2) a non-axisymmetric aerodynamically optimized endwall (AO) contour design. The contoured endwall was generated to minimize stagnation losses integrated over a plane 1.0 axial chord away from the trailing edge of the airfoil. The experiments were performed at Virginia Tech's quasi two-dimensional, linear, transonic blow down facility. The airfoil span increases in the mainstream flow direction in order to match realistic inlet/exit airfoil surface Mach number distribution. A transient Infrared thermography technique was employed to measure the endwall surface temperature. Heat transfer coefficient (HTC) and Adiabatic film cooling effectiveness (ETA) were calculated simultaneously from measured temperatures using a linear regression analysis assuming a 1-D semi-infinite transient conduction. The experimental technique consists of a two test methodology where, the coolant temperature was varied in both tests whereas, the mainstream temperature was kept similar with other flow and geometrical conditions remaining identical. The test section was always kept at ambient conditions initially. A cavity was fabricated inside the test section hardware to work as a coolant plenum. Three rows of strategically placed cylindrical holes with varied orientation and specific Length/Diameter (L/D) ratios were chosen to ensure fully developed flow for the present endwall cooling study. Results indicate prominent interaction between the three rows of coolant injection as well as with the passage vortex. Benefits of the endwall contouring can also be observed in reducing area averaged HTC as well as with higher coolant spread. In general, the coolant coverage improved with higher coolant blowing ratios, however, an increase in overall averaged HTC was observed for all blowing ratios compared to without blowing. The contoured endwall was also found to be advantageous in reducing net heat load to the platform for all film cooling conditions.

INTRODUCTION

Development of environmentally friendly power plants with strict regulations on significantly reducing NO_x emission levels along with increased efficiency has posed a critical challenge to turbine designers. Advanced gas turbines as a part of Integrated Gasification Combined Cycle (IGCC) have emerged as promising candidates to meet goals set by U.S. Depart of Energy (DOE) in achieving higher performance levels with increased fuel flexibility (specially for hydrogen rich fuels). Increased power output and thermal efficiency is driving advanced turbine development towards higher pressure ratios, operating temperatures and highly loaded airfoils which require further detailed investigation of aero-thermal performance parameters. Advanced airfoil and passage cooling schemes are required to address the issue of higher firing temperature at the turbine inlet high pressure stages (HPT) specially, with increased loading at transonic operating conditions. Endwall cooling schemes can be broadly classified into three categories – 1) upstream purge cooling, 2) discrete hole film cooling and 3) mate-face cooling. While upstream purge cooling and leakage flow through mate-face gap utilize existing turbine assembly features, endwall film cooling using discrete holes require thorough understanding of the secondary flow characteristics. Knowledge of local high heat transfer zones (hot spots) are required for location and basic hole design parameters (e.g. shape, ejection angle, L/D ratio). The major objective again like other cooling features is to obtain maximum film surface coverage and heat load reduction with minimum coolant usage. Three-dimensional vortices generated due to complex secondary flow effects largely influence location and orientation of film holes.

Endwall contouring on the other hand has emerged as an effective tool to reduce aerodynamic loss [1] as well as shown potential to improve endwall heat transfer performance [2]. Contoured endwalls are generated modifying passage geometric shape through numerical optimization routines with an objective function (to reduce secondary losses or overall heat transfer coefficient etc.). Now, it would be interesting to investigate how a combination of endwall film cooling in presence of endwall contouring is able to achieve better thermal performance compared to conventional passage with identical film cooling design. This comparison is illustrated with the aid of experimental measurements described in the following sections of the present article.

BACKGROUND STUDY

Prof. Goldstein's group at University of Minnesota performed some of the first pioneering studies [3-5] on film cooling applicable for gas turbines. The science and fundamentals behind film cooling technology has been widely studied by several researchers and has been well documented by Bogard and Thole [6], Bunker [7, 8], Han et al. [9]. According to the context of the present study the literature survey presented as following emphasizes efforts on understanding and improvements made by researchers with focus on endwall film cooling using primarily cylindrical hole design.

Takeishi et al. [10] proposed a three dimensional flow field model explaining the formation of major vortices contributing to secondary flow within the passage and underlined the impact on heat transfer and film cooling on

airfoil and endwall of a fully annular guide vane cascade (aspect ratio = 0.5). Rows of film holes were placed near leading edge and two other locations near the throat of the nozzle. The stronger influence of passage aerodynamic loading on the outer endwall compared to the inner endwall was the major conclusion of this study. Jabbari et al. [11] investigated the effect of blowing ratio, coolant density ratio and Reynolds number on adiabatic film cooling effectiveness measured at 60 different locations on the endwall. Film jet visualization was performed using ammonia-diazo technique. Majority of the jet traces were influenced by trajectory and strength of the passage vortex, however traces from the holes located near the downstream region were aligned along the mainstream direction. Friedrichs et al. [12] utilized the ammonia-diazo technique to quantify adiabatic film cooling effectiveness distribution on the endwall of a large scale, low speed, linear cascade. Effectiveness values were calculated based on the ammonia concentration gradient on the diazo paper using heat/mass transfer analogy. This paper had several important insights on endwall film cooling design based on the experimental results – 1) three dimensional separation lines need to be identified and holes should be placed underneath lift-off lines, 2) cooling requirements on the endwall are highly non-uniform and pressure side of the endwall requires improvement and 3) trajectory of the coolant jet was largely dependent on secondary flow structure and effect of ejection angles were negligible except immediate vicinity of the holes. Extensive studies on vane endwall film cooling performance have been carried out by Knost and Thole [13], Colban et al. [14,15] using Infrared (IR) thermography technique under steady state conditions. Knost and Thole [13] reported adiabatic film cooling effectiveness distribution for two different endwall discrete hole patterns with coolant blowing through discrete holes only as well as combined upstream purge slot and film coolant injection. As it was evident that upstream purge cooling was dominant near the center of inlet to the passage redesign of discrete hole patters were required in order to prevent over cooling. Interaction between slot cooling and film cooling flow streamlines were discussed. Colban et al. [14, 15] further continued this investigation to evaluate film cooling performance by comparing shaped hole design with nominal cylindrical hole design varying blowing ratios and inlet freestream turbulence levels. For both studies shaped hole provided significantly better film effectiveness coverage under identical conditions. The major deficiency in cylindrical film hole design was jet lift off/separation at higher blowing ratios which was hardly observed for fan shaped hole due to jet diffusion at the exit of the hole. Wright et al. [16] and Gao et al. [17] employed steady state Pressure Sensitive Paint (PSP) technique to measure endwall film cooling effectiveness for film only and combined purge slot/discrete hole coolant blowing conditions. Multiiple rows of discrete holes were fabricated near the pressure side of the platform with ejection angles aligned at 30° to the mainstream flow trajectory. The hole pattern followed the blade profile closely. Similar conclusions were drawn for cylindrical design where jet lift off was observed with increase in blowing ration beyond 1.0 when compared with laid back fan shaped holes [17]. Barrigozzi et al. [18, 19] performed film cooling effectiveness measurements using transient liquid crystal thermography under subsonic flow conditions for vane [18] and blade [19] endwall designs. The vane endwall consisted of four rows of discrete holes spread over the entire region from leading edge to trailing edge whereas, only one row of pressure side holes were used for the blade endwall experiments.

In contrast to the brief literature review presented in the preceding paragraph, experimental measurements on endwall discrete hole film cooling under transonic conditions are rare. Harasgama and Burton [20] were the first to report heat transfer performance of a nozzle guide vane passage in presence of endwall film cooling using a short duration annular cascade based on engine representative operating conditions (exit Reynolds number ~ 2.55 x 10^6, exit Mach number ~ 0.93, coolant density ratio ~ 1.8). A typical aircraft engine endwall film cooling pattern was chosen using four rows of holes strategically placed on iso-Mach lines to ensure uniform blowing rate and momentum ratio at the hole exit. They achieved up to 75% reduction in endwall Nusselt number close to the plane of injection, however, near trailing edge along the pressure side coolant flow was swept away by passage vortex and strong cross passage flow due to induced pressure gradient reducing the cooling efficiency to 20% only. Nicklas [21] applied IR thermography along with known heat flux conditions from a surface heater for simultaneous measurement of endwall heat transfer coefficient and adiabatic film effectiveness distribution in presence of combined upstream slot leakage and endwall film cooling under transonic operating conditions. Local enhancement of heat transfer coefficient and turbulence levels were reported just downstream of the coolant ejection holes. Jonsson et al. [22] developed a three test methodology to measure three important film cooling parameters simultaneously on a vane platform under compressible flow conditions – heat transfer coefficient, adiabatic film cooling effectiveness and surface heat flux using IR thermography coupled with thermo-chromic liquid crystal and surface foil heater. Salvadori et al. [23] used steady state PSP technique to calculate film effectiveness distributions for fan shaped discrete cooling holes on the endwall at design isentropic exit Mach number of 0.88.

Endwall discrete hole film cooling in presence of endwall contouring has been investigated only by Thrift et al. [24]. They reported film cooling performance of an axisymmetric endwall contour design and concluded the baseline planar endwall showed better film cooling coverage as the turning of the mainstream flow at the contoured surface reduced the local blowing ratios near the pressure side.

MOTIVATION AND OBJECTIVE

The present study is a continuation and further development of Roy et al. [25] incorporating discrete hole film cooling onto the baseline and aero-optimized (AO) endwall geometries for a high turning (127°), high pressure turbine passage operating at design exit Mach number - 0.88 and design incidence angle. The inlet Mach number is 0.45 and inlet Reynolds number (based on axial chord length) is about 9 x 10^5. Key heat transfer parameters – heat transfer coefficient (HTC) and adiabatic film cooling effectiveness (ETA), have been experimentally measured for two different coolant to mainstream mass flow ratios (MFR) – 0.15% and 0.25%. The objective of the present study is to provide experimental data for film cooled endwall at transonic operating conditions in presence of endwall contouring and quantitative comparison of overall heat transfer performance based on local net heat flux reduction (NHFR) distribution. To the best of the authors' knowledge, no studies have been reported in open literature on the effect of endwall contouring with discrete hole film cooling under transonic operating conditions.

NOMENCLATURE

AO	Aero-Optimized
C_{ax}	Axial chord length (m)
h, HTC	Heat transfer coefficient $\left(\frac{W}{m^2K}\right)$
h_f	Heat transfer coefficient – Film Cooled case $\left(\frac{W}{m^2K}\right)$
h_{ref}	Heat transfer coefficient – Reference case $\left(\frac{W}{m^2K}\right)$
IR	Infrared
k	Thermal conductivity $\left(\frac{W}{m\,K}\right)$
M	Mach number
M_{iso}	Isentropic Mach number $M_{iso} = \sqrt{\left(\left(\frac{p_{0in}}{p_{s\,exit}}\right)^{\frac{\gamma-1}{\gamma}} - 1\right)\frac{2}{\gamma-1}}$
MFR	Mass flow ratio (coolant mass flow rate per passage/ mainstream mass flow rate per passage)
NHFR	Net Heat Flux Reduction
p_{0in}	Pitchwise average stagnation pressure at inlet midspan (Pa)
$p_{s\,exit}$	Pitchwise average static pressure on angled end wall 0.5 C_{ax} downstream of the trailing edge (Pa)
q''	Heat flux $\left(\frac{W}{m^2}\right)$
r	Recovery factor
t	Time (s)
T	Temperature (K or ^{o}C)

T_{aw} Adiabatic wall temperature (K or ^{o}C)

T_f Film temperature (K or ^{o}C)

T_r Recovery temperature (K or ^{o}C)

T_{ref} Reference temperature (K or ^{o}C)

T_w Wall temperature (K or ^{o}C)

T_i Initial temperature (K or ^{o}C)

T_c Coolant temperature (K or ^{o}C)

T_m Mainstream temperature (K or ^{o}C)

Greek Letters

α Thermal diffusivity $\left(\frac{m^2}{s}\right)$

φ Overall Cooling effectiveness

γ Ratio of specific heats

η, ETA Film/Adiabatic Cooling effectiveness

Suffix

min Minimum value

max Maximum value

EXPERIMENTAL METHODOLOGY

Experimental Test Facility

A schematic of the transonic cascade wind tunnel at Virginia Tech is shown in Figure 18. The wind tunnel is a blow down facility capable of a thirty second run time. The air supply is pressurized by a four-stage Ingersoll-Rand compressor and stored in large outdoor tanks. The maximum tank pressure used for transonic tests is about 2068 kPa (300psig). A control valve is used to regulate the flow from the tanks to the test section. During a run, the upstream total pressure is held constant by varying the opening of a butterfly valve controlled by a computerized feedback circuit. The airfoil isentropic exit Mach number is varied by changing the upstream total pressure. The airflow through the cascade is controlled valve 1 as shown in Figure 18. The first and the second valve remain open during

the aerodynamic measurements while the third one remains closed allowing the air flow directly from inlet to the test section. For the heat transfer experiments, the valves one and two are initially kept closed and the third one is kept open. Air is circulated through heater loop and the copper bars acting as thermal capacitor. The heated air from heater heats up copper tubes in the heat exchanger. The third valve is closed and the other two valves are opened when the temperature in the heat exchanger reaches a specified magnitude (100^{o}C). The air gets heated through the heat exchanger while passing from the inlet to the test section.

The cascade test section, as shown in Figure 19, consists of 5 airfoils resulting in 4 passages, with a controlled bleed flow above the first airfoil. This passage design is identical to as reported in Roy et al. [25], the 3rd passage from top is the passage of interest where all discrete holes are fabricated and heat transfer measurements are carried out. The airfoils are mounted on a rotatable window, which allows for changes in incidence angles as and when required. All experiments were performed at design incidence angle, therefore cascade angle was fixed accordingly. Airfoil 3 from top is considered as the center airfoil of the linear cascade. A headboard, positioned upstream of the cascade is instrumental in controlling the incoming flow by preventing an induced incidence angle effect on the leading edges of the airfoils.

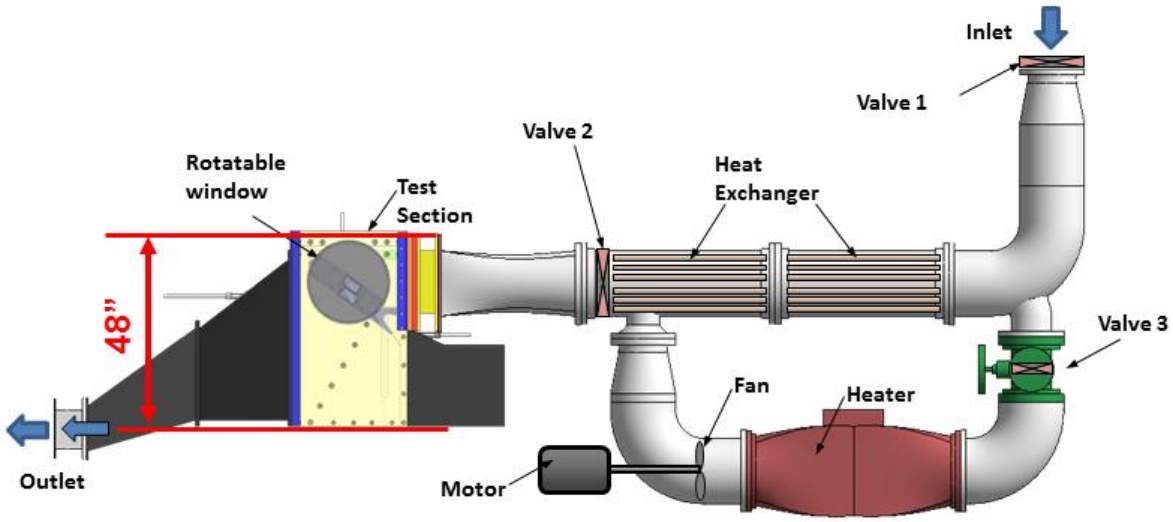

Figure 18: Virginia Tech transonic tunnel facility

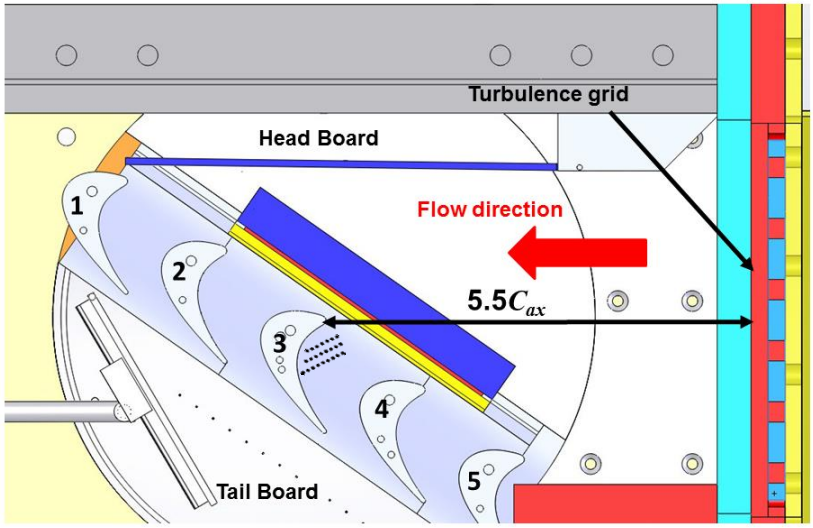

Figure 19: Cascade test section details with turbulence grid

The headboard is used to create and control a flow bleed that prevents the flow from turning prior to reaching the leading edge of the airfoils. Uniform inlet flow conditions can be achieved by careful adjustment of the headboard angle which aids in maintaining uniform and periodic flow through each airfoil passage and ensuring that the flow angle gradient ahead of the cascade is zero.

The inlet Mach number is measured by a Pitot static probe located 0.5 axial chords upstream of the center blade leading edge. The isentropic exit Mach number is decided based on the inlet total pressure (as measured by the pitot static probe) and the average wall static pressure measured 0.5 axial chords downstream of the cascade. The inlet total pressure profile was measured 0.5 C_{ax} upstream of the leading edge using 5 hole probe traverses in pitchwise direction at different span locations from the endwall up to the midspan. A turbulence grid is placed 5.5 C_{ax} upstream of the center blade as shown in Fig. 2. Inlet free stream turbulence intensity was measured at mid-span 0.5 C_{ax} upstream of the blade leading edge using a hot-wire anemometer and was found to be about 8%.

Discrete Hole Design

The preliminary endwall discrete hole film cooling design was provided by Siemens Energy Inc. All film cooling holes were cylindrical in shape and 1.2mm in diameter. The hole ejection angles were based on specific coolant requirements at corresponding locations. The location of the first row of holes as shown in Figure 20 starts just after the leading edge from pressure side of the passage and extends up to ~ 0.5C_{ax} along the passage.

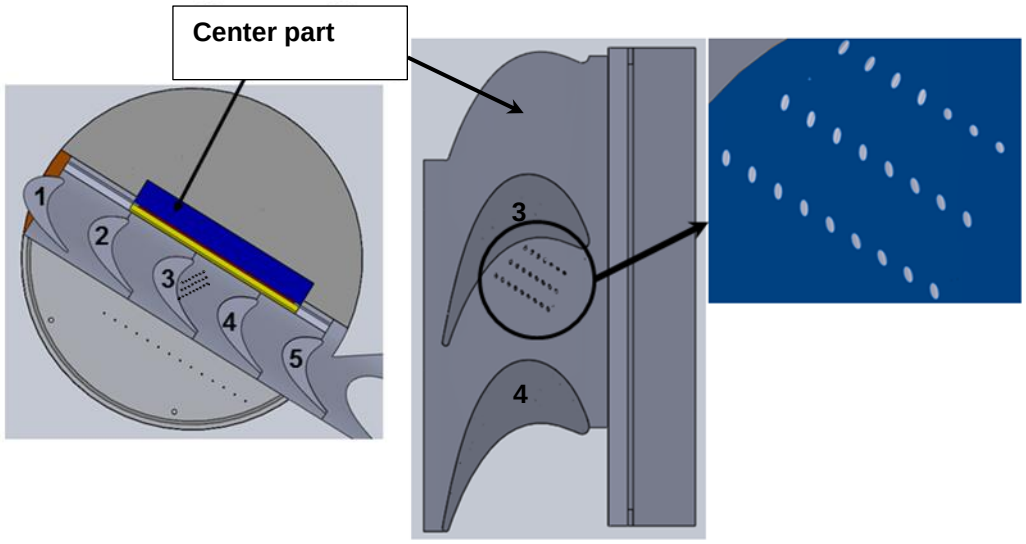

Figure 20: Discrete hole geometry (a) Cascade schematic, (b) measurement passage, (c) close up of hole location and orientation

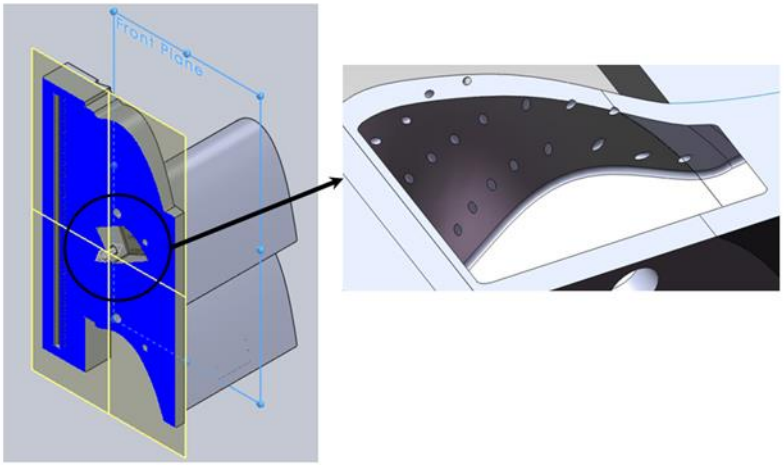

Figure 21: Discrete hole coolant cavity (a) section plane, (b) coolant cavity inside view

There are three rows of coolant holes, where the first, second and third row consists of 7, 8 and 9 holes respectively. An individual row starts near airfoil pressure side endwall junction and ends near mid passage. The length to diameter (L/D) ratio of all the holes were in the range 4-5 to simulate actual engine representative hole designs as well as ensure fully developed flow conditions. In order to keep such a small L/D ratio for both endwall geometries, the coolant plenum was embedded inside the endwall by making a cavity and hole inlet surface profile was made same as external endwall surface as shown in Figure 21. Hence, the coolant after entering into the cavity from external plumbing system flows into the coolant holes. The coolant cavity ensures proper mixing of the coolant stream and coolant temperature measurement was also performed inside the cavity just before the inlet of the

cooling holes. The hole location on endwall was primarily based on cooling requirements of high heat transfer zones along the passage horse-shoe vortex flow path for both geometries. Though the individual hole angles are different, identical hole pattern along with the plenum cavity was fabricated for the AO endwall as well to maintain consistency in comparing film cooling performance w.r.t. the baseline endwall.

Endwall Design

Two different passage designs were studied for endwall film cooling performance. The endwall designs were provided by Siemens Energy, Inc. The first endwall geometry is non-contoured referred as Baseline endwall. The other endwall geometry denoted as AO (Aero-optimized) endwall was obtained from an optimization study in order to minimize aerodynamic losses at $1.0C_{ax}$ downstream of the airfoil trailing edge. The upstream purge slot design and dimensions were kept identical for both endwall geometries, however no coolant was blown through. The basic features of the contoured endwall geometry are shown in Figure 22. The AO contoured endwall shows a strong peak region along the passage starting from the leading edge pressure side and a trough region along suction side starting ~ $0.2C_{ax}$ normal up to trailing edge. Further details of the design procedure and surface modification features are provided in Panchal et al. [2].

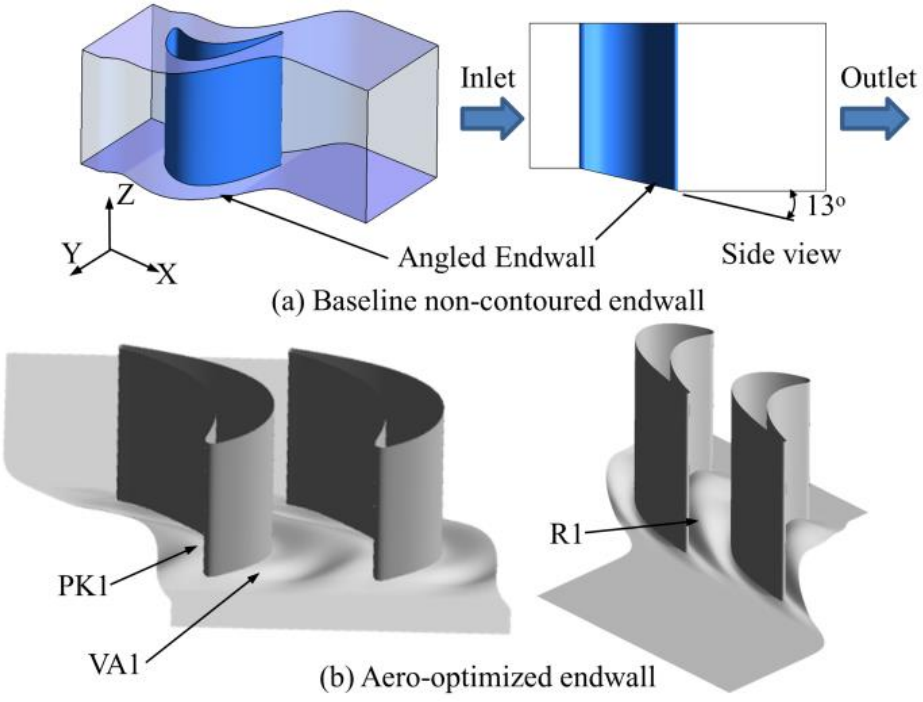

Figure 22: Endwall geometries

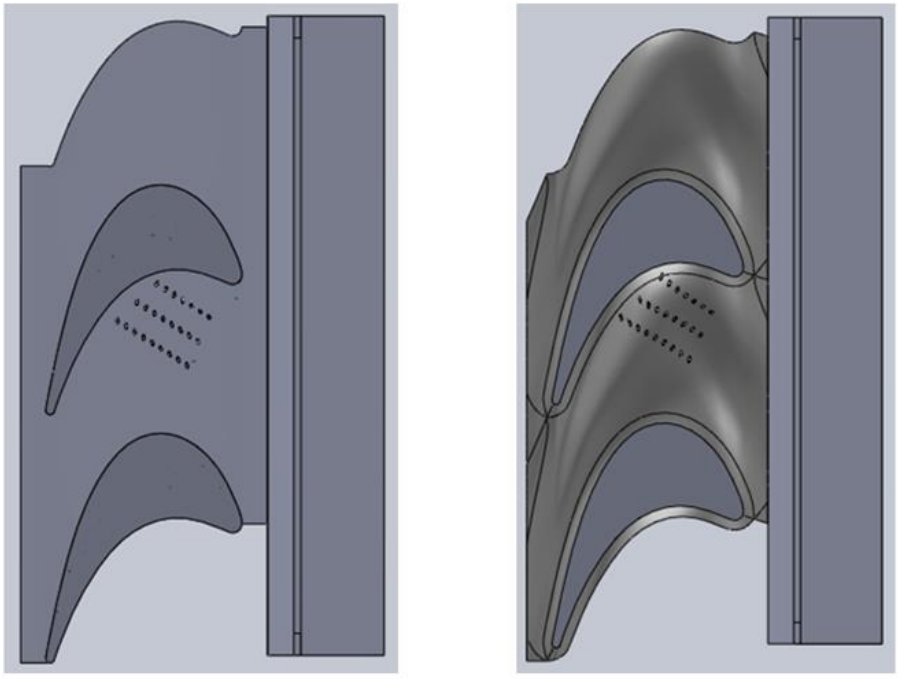

Baseline geometry **AO geometry**

Figure 23: Endwall hole patterns

Figure 23 shows the endwall discrete hole locations on baseline and AO passage. The hole inlet plane was designed to match the exact shape of corresponding endwall in order to achieve the same L/D ratio of all holes for both baseline and AO geometry. As seen in Fig. 6 the holes on the AO endwall are located on the peak region as well as across the valley of the contour.

HEAT TRANSFER MEASUREMENT TECHNIQUE

Endwall surface temperature measurements were performed using an Infrared (IR) camera. Two IR transparent windows were added with a line of sight to the endwall surface being studied, as shown in Figure 24. Due to the large forces seen in a transonic facility, the window also needed to be structurally sound. Two 4.5”x2.5” rectangular Zinc Selenide windows were used as to satisfy the design constraints. Only one window was used at a time for endwall temperature measurements while the other window was closed using a piece of lexan block. All the inner surfaces of the test section and outer surfaces of the test-section window were painted using a black paint to avoid thermal reflection from the surfaces. Coolant plenum cavity was fabricated inside the test section hardware as mentioned earlier and coolant temperature was measured at a point inside the cavity close to the inlet of the film holes.

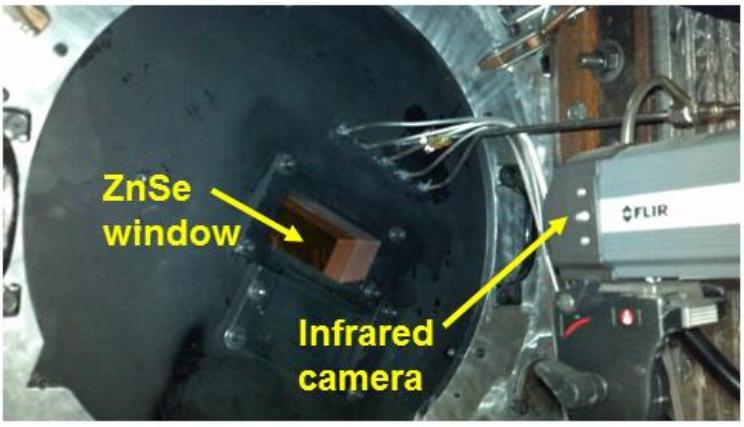

Figure 24: Heat transfer cascade set up (a) front window, (b) rear window, and (c) actual setup

The material of the endwall and the airfoils is Acrylonitrile butadiene styrene (ABS) that has low thermal conductivity. Since the reducible data is obtained only over a short duration (~ 5s), the thermal penetration length into the endwall in any direction is about 0.8mm. Other modes of heat transfer e.g. radiation can be safely neglected as the maximum operating range of the endwall surface temperatures is about 60^{o}C. The paint film thickness is so small (order of microns) compared to endwall dimensions, conduction in the transverse direction through the paint coating is assumed to be negligible. Therefore, the 1-D, semi-infinite heat transfer assumption is applicable at each location on the endwall. Moreover, significant cool down times in between runs were allowed so the endwall is at a uniform initial temperature at the start of every tunnel run. The IR camera used, ThermaCam SC325, at a resolution of 320x240, can measure 76800 surface temperature locations simultaneously with a 0.6mm x 0.6mm cross section for an individual pixel. Due to 1-D semi-infinite assumption results obtained for each individual pixel is assumed to be independent of the other.

The governing differential equation for 1D transient conduction along with initial and boundary conditions are expressed as,

$$\alpha \frac{\partial^2 T}{\partial x^2} = \frac{\partial T}{\partial t} \tag{1}$$

$t = 0$, $T = T_i$ (Initial Condition) (2)

$x = 0$, $T = T_w$ (Surface temperature boundary condition) (3)

$x \rightarrow \infty$, $T = T_i$ (Semi-infinite solid assumption) (4)

The convective heat flux at the surface can be defined as,

$$q'' = (T_m - T_w) \tag{5}$$

Uncooled heat transfer analysis

The mainstream fluid temperature (T_m) is replaced by local recovery temperature (T_r) considering compressible flow to account for aerodynamic heating near boundary layer.

Hence Eq. (5) is modified accordingly as shown,

$$q'' = h(T_r - T_w) \tag{6}$$

$$T_r = T_m \left(\frac{1 + r\left(\frac{\gamma - 1}{2}\right) Ma^2}{1 + \left(\frac{\gamma - 1}{2}\right) Ma^2} \right) \tag{7}$$

where, r = recovery factor = $Pr^{1/3}$ for turbulent boundary layer (Pr = Prandtl Number).

The calculation of surface heat flux is a two-step process where, in the first step, the conduction heat flux inside the solid material is calculated using a Finite Difference Method where Eq.(1)-(4) is solved using 2nd order discretization. The surface heat flux is thus computed from conduction analysis and is equal to the convective heat flux. The second step consists of for estimation of HTC, the calculation take place in the convective domain. However, the data processing time window can be chosen to avoid the transition period of the tunnel start, so that the HTC remains constant in the calculation. The data reduction time window of these two steps is shown in Figure 25. The data reduction time window of curve fitting method is also shown on the same plot. The heat flux reconstruction needs the data from the tunnel start, because a uniform condition of the initial temperature in the material is necessary to solve Eq. (1)-(4).

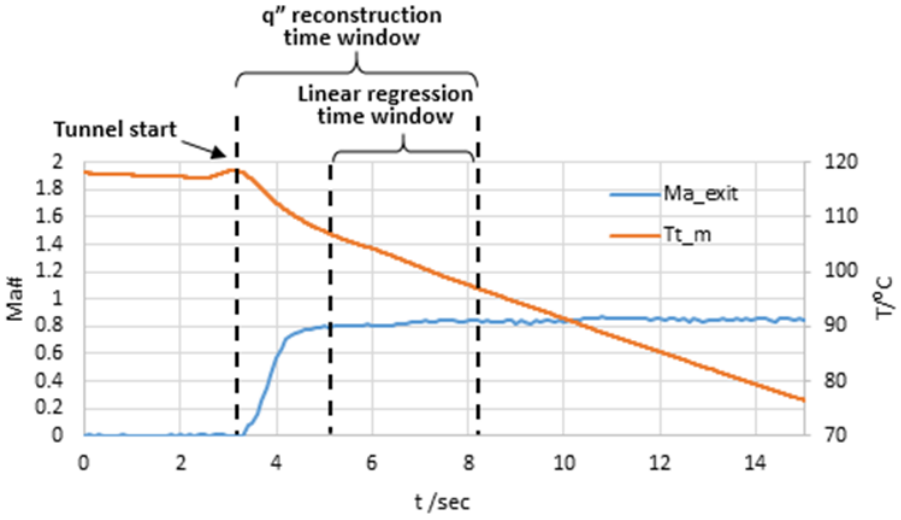

Figure 25: Tunnel temperature history and data processing window

Rearrange Eq. (6), we can get a linear relationship in the form,

$$q''(t) = h\left(T_m(t) - T_w(t)\right) + h\left(T_r(t) - T_m(t)\right) \tag{8}$$

The value of the last term in Eq. (8), only depends on the aerodynamic condition, and is constant as the local Mach number does not change within the calculation time window. Theoretically, all the data points should fall on a straight line, as shown in Figure 26. The slope of this line is the HTC, and the recovery temperature can be estimated from the Y intercept.

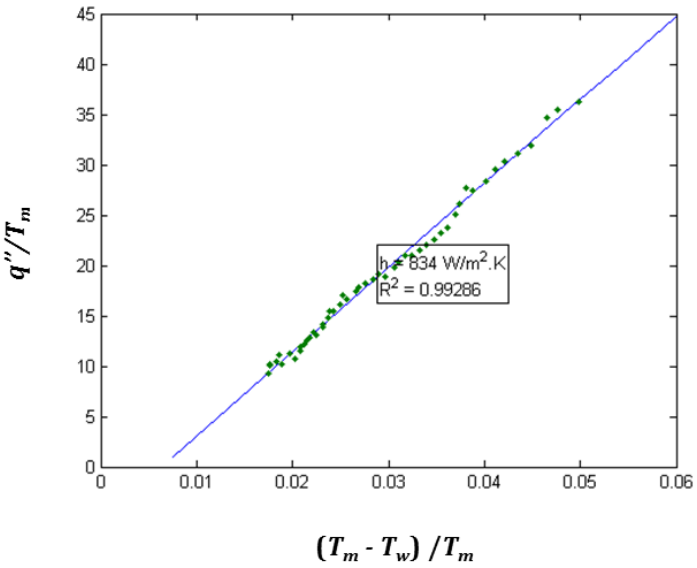

Figure 26: Linear regression plot for uncooled heat transfer

Film-cooled heat transfer analysis

However, for film cooling cases, where coolant is injected into the mainstream, T_m needs to be replaced by film temperature T_f which is a mixed intermediate temperature between mainstream and coolant governing the convective heat transfer to the surface wherever coolant film exists on the endwall. Therefore, all film cooling cases can be considered as three temperature problem involving mainstream (local recovery temperature), coolant and wall temperature. Adiabatic film cooling effectiveness (ETA) is a non-dimensional representation of T_f and is defined as,

$$\eta = \frac{T_r - T_f}{T_r - T_c} \tag{9}$$

Hence, the convective heat flux equation for film cooling cases is expressed as,

$$q'' = h\left(T_f - T_w\right) \tag{10}$$

Equation (10) can be algebraically manipulated to obtain the following expression,

$$\frac{q''}{T_r - T_c} = h\left(\frac{T_r - T_w}{T_r - T_c}\right) - h\eta \tag{11}$$

Since data is acquired during the steady period of the tunnel run, HTC and ETA can be assumed constant.

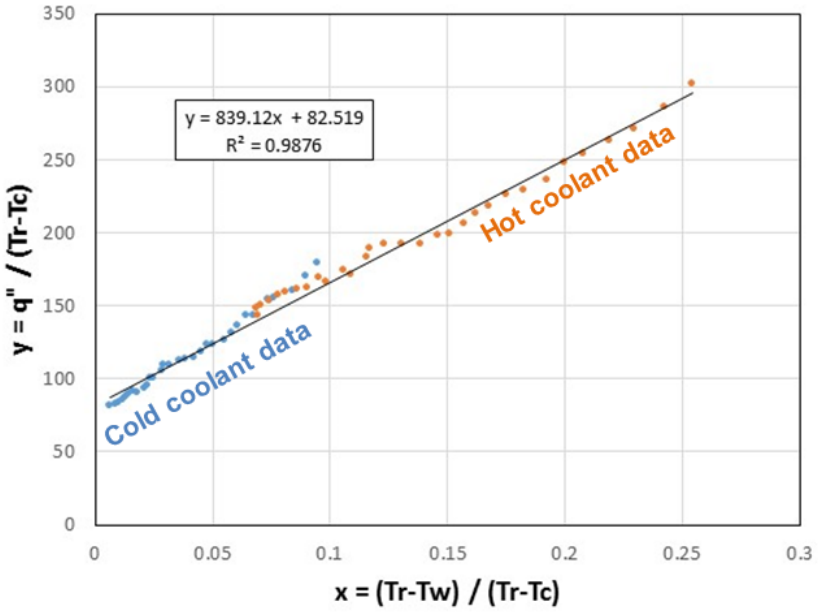

Figure 27: Linear regression curve fit for film cooled cases

Two similar transient tests are necessary in order to solve for HTC and ETA simultaneously. The experimental methodology of running two similar tests for film cooling cases has been adopted from Ekkad et al. [26] which is referred to as heated mainstream transient technique in section 3.2.1 of the article. The first transient test is carried out with mainstream at a high temperature and coolant at chilled temperatures (lower than ambient) and suddenly exposed to surface at ambient temperature. In the second test, the only difference is the coolant is heated up to a certain temperature instead of being cooled. The current method differs to some extent from the method described in Ekkad et al. [26], where for high speed flows coolant and mainstream temperatures cannot be matched and the mainstream cannot be continuously heated during experiments. Nevertheless, generating two different data sets from two similar transient runs provides enough points to solve the two unknowns iteratively. The basic assumption embedded into the data reduction technique is that HTC and ETA being hydrodynamic parameters, hence independent of operating temperatures, and experimental operating (flow) conditions remains same between "hot coolant" run and "cold coolant run". The T_r values are matched for both hot coolant run and cold coolant run as it depends on local Mach number and remains constant for a particular location during the data reduction period. The linear fit of data for film cooling cases is shown in Figure 27 where, HTC is obtained from the slope and ETA is obtained from the Y-intercept.

Uncertainty Analysis

For linear regression technique, two different uncertainty analysis methods are applied in the two data processing steps respectively. The propagation of the major errors is analyzed through the Moffat's [27] perturbation method. The linear regression uncertainty analysis was carried out according to the method recommended by Brown and Coleman [28]. The average uncertainty for HTC measurements is about 8% whereas, for ETA values it is ~ 6%.

Data Representation

The basic data representation technique which involves mapping of two-dimensional raw HTC data onto three dimensional endwall surface using camera transformation matrix and image stitching was developed by Panchal et al. [2] and is not repeated here. This technique was further used for representing ETA values on a three-dimensional endwall similarly.

RESULTS AND DISCUSSION

The results discussed in this section are arranged in the following manner – First, local heat transfer analysis is presented for both Baseline and AO endwall without coolant flow through the film cooling holes, Second, key heat transfer parameters – endwall heat transfer coefficient and adiabatic film cooling effectiveness have been elaborated for both endwall geometries corresponding to two coolant blowing rates (MFRs – 0.15% and 0.25%). Finally, quantitative comparison between both endwall geometries has been described based on overall thermal performance. All heat transfer results shown in the following sections have been normalized (HTC normalized by area averaged HTC $1.0C_{ax}$ upstream of the slot and adiabatic effectiveness normalized by maximum value over the area) due to proprietary nature of the data.

Normalized endwall HTC distribution for baseline and AO geometry is shown in Figure 28 for cases without coolant blowing in order to evaluate the heat transfer performance of the endwall due to presence of the holes only. It can be immediately observed that even without blowing there are local high HTC zones surrounding the hole locations for the first row and most of holes of the second row. However, some streak patterns are present in almost all the holes in the third row. This happens due to mainstream flow ingress into the coolant cavity through the 1^{st} and 2^{nd} row of holes. The coolant comes out mostly from the 3^{rd} row of holes after flow circulation inside the coolant cavity. Typically the amount of mainstream ingress can be considered much less even compared to the case with lowest coolant blowing ratio because of small diameter of the holes. As mentioned earlier, the location of the holes were determined based on the path followed by the passage horse-shoe vortex for the baseline geometry. The horse-shoe vortex flow direction also signifies high HTC zones on the endwall and is the primary contributor for secondary losses.

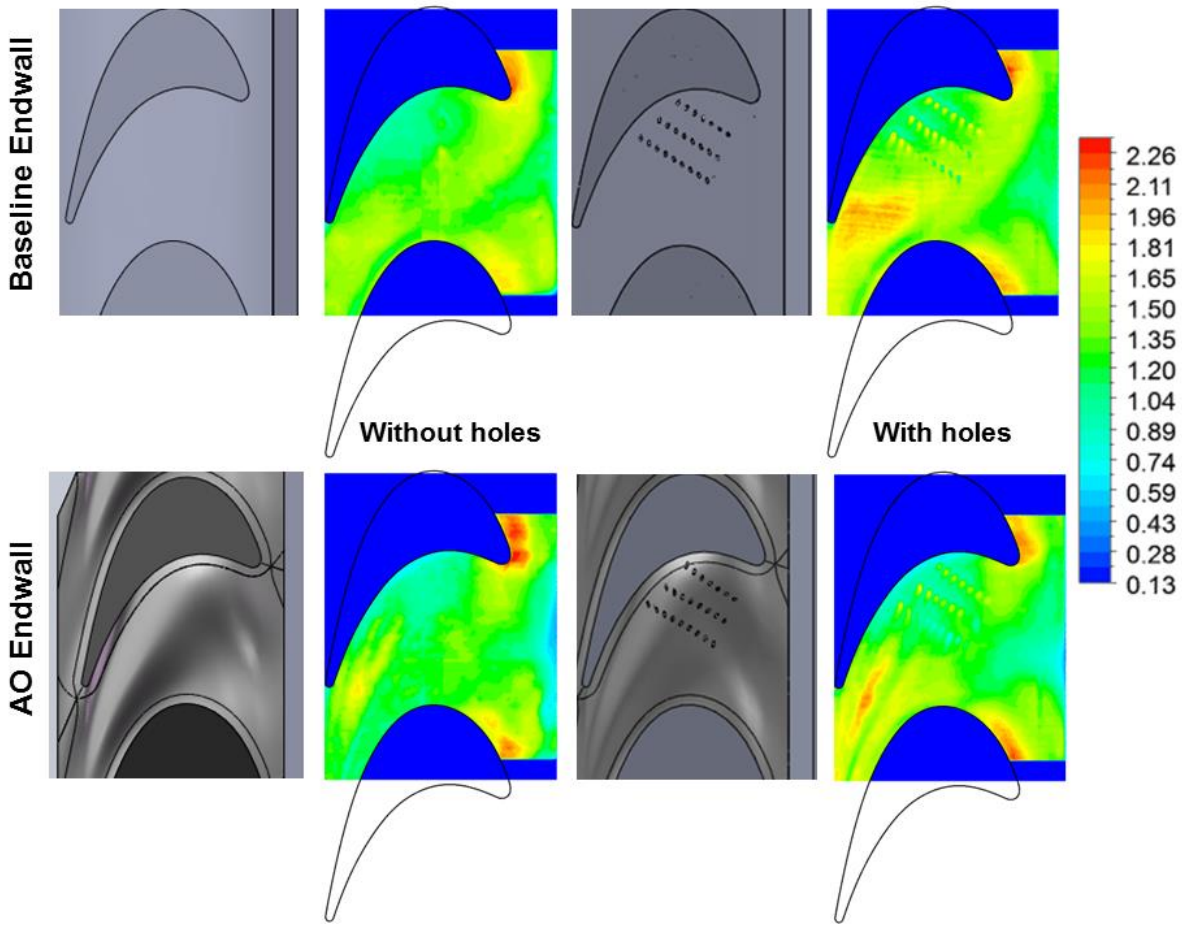

Figure 28: Normalized endwall heat transfer coefficient distribution with endwall contouring without coolant flow

As shown in Figure 28for both baseline and AO endwall presence of holes tend to increase the overall HTC to some extent. Table 1 shows the percentage deviation of overall area averaged endwall HTC values using baseline discrete holes without blowing as reference. As noticed in the contour plots, the AO endwall still performs better than baseline endwall but overall HTC has increased by 4% compared to without holes for AO endwall. Hence the effects of endwall contouring are less prominent for discrete hole without blowing cases compared to without hole cases. For both endwall designs, local heat transfer levels are observed to increase downstream after the throat region.

Figure 29 shows the normalized HTC contour plots of discrete hole film cooling cases for baseline and AO endwall. The overall area averaged HTC comparison for film cooling cases are also summarized in Table 2. It is important to observe that with injection of coolant local HTC values near the hole locations increase and it increases further with higher coolant blowing rates. The turbulent mixing of coolant jets with mainstream creates high HTC zones at the hole locations as well as along the coolant streaks. The coolant flow exiting the discrete holes also initiates a new boundary layer on the endwall surface which can contribute towards very high local HTC values.

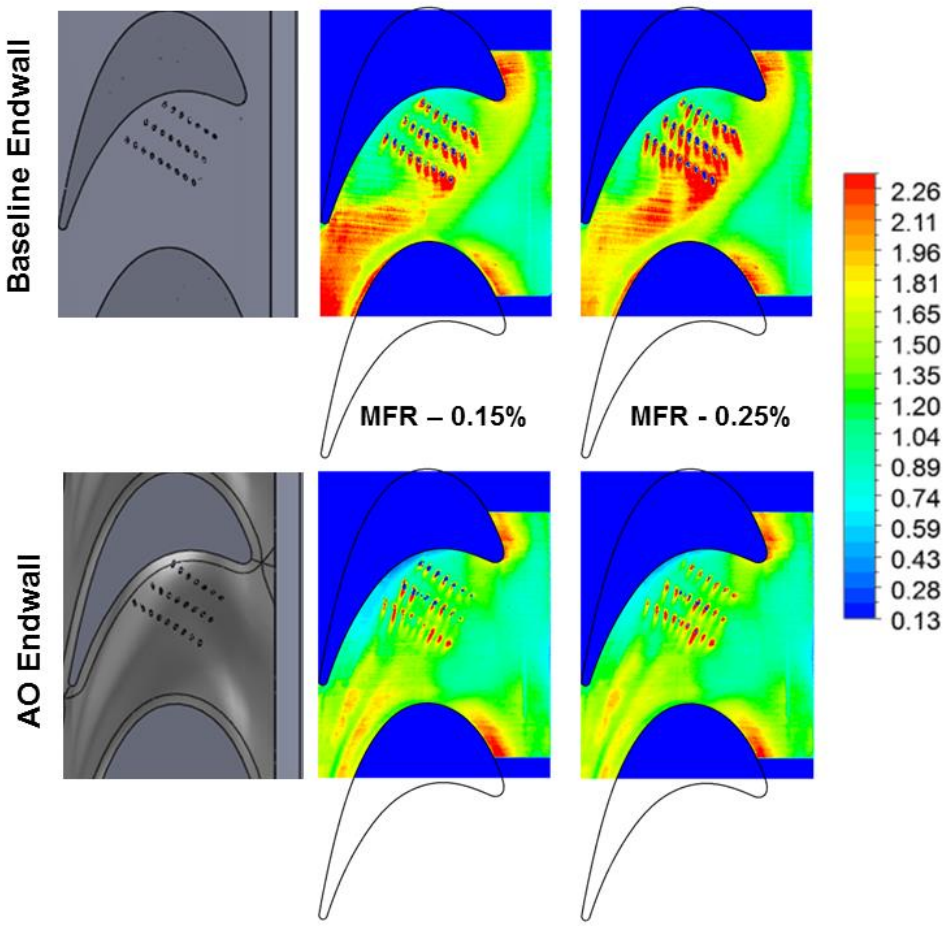

Figure 29: Normalized endwall heat transfer coefficient for film cooling cases

One interesting characteristic can be observed that, with increase in coolant blowing ratio higher endwall heat transfer regions are seen near hole exit for baseline geometry. This is more evident following the near hole HTC streaks emerging from all three rows. Therefore, overall area averaged HTC also increases with higher coolant MFR. However, for AO endwall HTC streaks are comparable for both coolant MFRs considered, with marginal reduction of area averaged HTC for higher blowing rate (MFR 0.25%). The major reason behind increased near hole heat transfer for baseline endwall is believed to be the interaction between strong secondary flow and injected coolant into the mainstream. Near the hole ejection region turbulent mixing is highly promoted due to mixing of coolant jet with pressure side leg of the horse-shoe vortex. This phenomenon is hardly visible from normalized HTC contour plots of AO endwall largely due to weaker secondary flow and redirection of passage horse-shoe vortex path.

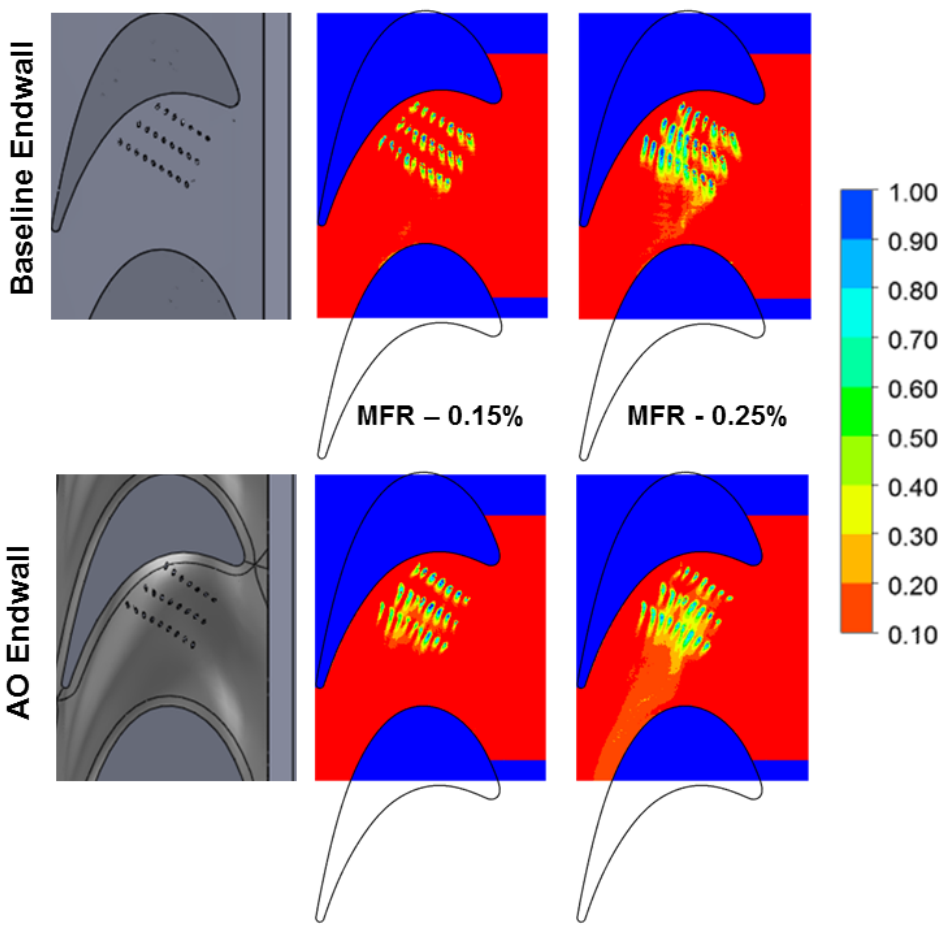

Figure 30: Normalized adiabatic film effectiveness contours for all film cooling cases

Table 2: Area averaged heat transfer coefficient comparison

	Without film holes	Without coolant	MFR – 0.15%	MFR – 0.25%
Baseline	- 7%	-	+ 1.5%	+ 6%
AO	- 13%	- 9%	- 13%	- 11.5%

It is important to mention here that for higher blowing rates merging of several coolant jets can be observed more significantly for baseline geometry. This can be attributed primarily due to the secondary flow sweeping the coolant jets across the passage. Minor conduction effects can also cause high HTC zones between the holes and streaks as the coolant cavity is only ~ 5mm thick from hole inlet to outlet. Although the theoretical thermal penetration depth is about ~ 1mm, low but finite thermal conductivity of the material can produce conduction effects near hole locations which is assumed to be negligible. For more accurate results transient conjugate heat transfer analysis is required to eliminate the effects of 2D conduction completely.

It is interesting to note that in Figure 30 for baseline endwall the coolant streaks are distinct and almost all of them are aligned towards the suction side of the airfoil, whereas for AO endwall the streaks are directed more towards mainstream flow direction. This can be explained from the interaction between secondary flow and coolant flow. For the baseline geometry there exists a strong cross passage flow due to pressure differential from pressure side to suction side of the airfoil. In case of low coolant blowing rates, the low momentum coolant jet rapidly diffuses into the mainstream and swept away by the secondary flow. However, for higher coolant MFR the coolant jet is stronger and able to sustain the flow along the endwall to some extent before diffusing into mainstream. Whereas, the cross passage secondary flow in AO endwall is not as strong as compared to baseline endwall, therefore the coolant streaks are more spread out on the endwall and aligned towards the mainstream flow direction for all blowing ratios.

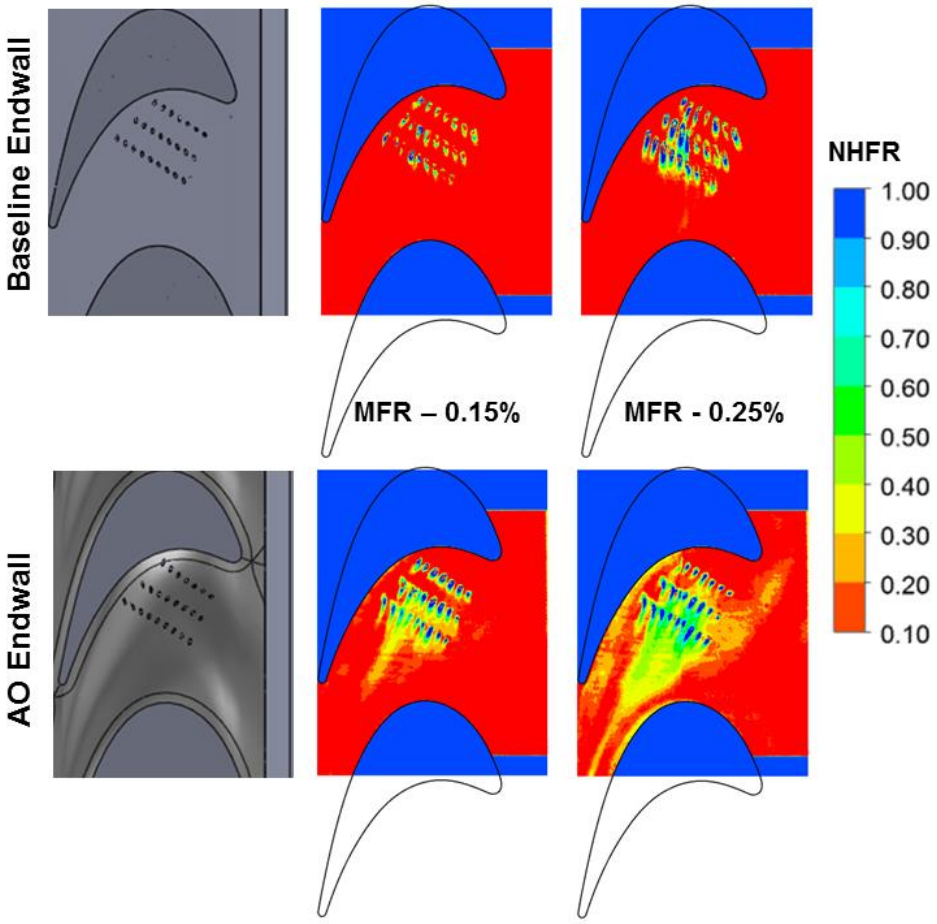

Figure 31: Local Net Heat Flux Reduction (NHFR) distribution – Endwall film cooling

Net Heat Flux Reduction (NHFR) analysis has also been carried out to further identify the benefits of using endwall contouring as depicted in Figure 31. NHFR – a combination of HTC and ETA, the analytical expression of which is provided in Eq. (12), is used widely in literature to figure out the overall performance enhancement in

presence of cooling features compared to a non-blowing reference case (Baseline geometry with discrete holes without coolant flow).

$$\text{NHFR} = 1 - \frac{h_f}{h_{ref}}\left(1 - \frac{\eta}{\varphi}\right) \tag{12}$$

Where, φ is a non-dimensional metal temperature defined as overall cooling effectiveness and an average value of φ = 0.6 is used considering realistic gas turbine inlet, metal and coolant temperatures [29]. It is evident from Figure 31 that the contoured endwall significantly improves endwall NHFR in presence of discrete hole film cooling due to the combination of the following – 1) effective control of the secondary flow reducing the passage vortex strength and strong cross passage flow gradients and 2) the coolant film is therefore able to stay attached to the endwall surface further into the passage especially for higher MFR. The major contributor towards pressure side NHFR is due to reduction in local HTC. However a combination of reduced HTC and improved film effectiveness levels is dominant in higher NHFR over the mid-passage region.

CONCLUSIONS

Heat transfer performance of a non-axisymmetric contoured (AO) endwall generated to minimize aerodynamic losses was experimentally investigated and compared with a conventional planar (baseline) endwall in presence of discrete hole film cooling at two different leakage flow rates (0.15% and 0.25% MFR) at design exit isentropic Mach number of 0.88 and design incidence angle using IR thermography technique. The major findings can be summarized as:

- The overall heat transfer performance for AO endwall was better than baseline geometry for all discrete hole film cooling cases considering key heat transfer parameters – heat transfer coefficient, film cooling effectiveness and net heat flux reduction.

- The presence of holes increased overall average heat transfer coefficient on AO endwall even without coolant blowing, thus reducing the benefits of contour design to some extent. It is important to mention that the AO endwall contour design was optimized without taking into account any endwall cooling features. This might be due to discrete holes creating additional local high turbulence.

- For film cooling cases, endwall contouring proved to be advantageous as up to 16% reduction in area averaged HTC together with significant improvement in endwall NHFR. In case of baseline endwall very high heat transfer zones are observed locally near the hole exit locations. The coolant streaks as visible from heat transfer coefficient contours are intense for baseline endwall due to high turbulence dissipation of coolant jet into mainstream and initiation of new boundary layer

ACKNOWLEDGEMENTS

The authors would like to acknowledge the funding support from the US Department of Energy through Siemens Energy, Inc. This material is based upon work supported by the US Department of Energy under Award Number DE-FC26-05NT42644.

REFERENCES

[1] Abraham, S., Panchal, K.V., Ekkad, S.V., Ng, W.F., Lohaus, A.S., and Malandra, A., 2012, "Effect of endwall contouring on a transonic turbine blade passage: Part 1 – Aerodynamic performance", *Proceedings of ASME Turbo Expo* 2012, ASME Paper No. GT2012-68425.

[2] Panchal, K.V., Abraham, S., Ekkad, S.V., Ng, W.F., Lohaus, A.S., and Crawford, M.E., 2012, "Effect of endwall contouring on a transonic turbine blade passage: Part 2 – Heat transfer performance", ASME Paper No. GT2012-68405.

[3] Wilson, D.J., and Goldstein, R.J., 1973, "Effect of Film Cooling Injection on Downstream Heat Transfer Coefficients in High Speed Flow", J. Heat Transfer, 95(4), pp. 505-509.

[4] Wilson, D.J., Eriksen, V.L., and Goldstein, R.J., 1974, "Predicting Heat Transfer Coefficients With Film Cooling From a Row of Holes", J. Heat Transfer, 96(2), pp. 258-260.

[5] Eriksen, V.L., and Goldstein, R.J., 1974, "Heat Transfer and Film Cooling Following Normal Injection Through a Round Hole", J. Engineering for Power, 96(4), pp. 329-334.

[6] Bogard, D.G., and Thole K.A., 2006, "Gas Turbine Film Cooling", AIAA J. Propulsion and Power, 22(2), pp. 249-270.

[7] Bunker, R.S., 2006, "Gas Turbine Heat Transfer: Ten Remaining Hot Gas Path Challenges", J. Turbomachinery, 129(2), pp. 193-201.

[8] Bunker, R.S., 2005, "A Review of Shaped Hole Turbine Film-Cooling Technology", J. Heat Transfer, 127(4), pp. 441-453.

[9] Dutta, S., and Ekkad, S.V., 2010, *Gas Turbine Heat Transfer and Cooling Technology*, Taylor & Francis, New York.

[10] Takeishi, K., Matsura, M., Aoki, S., and Sato, T., 1990, "An experimental study of heat transfer and film cooling on low aspect ratio turbine nozzles", J. Turbomachinery, 112, pp. 488-496.

[11] Jabbari, M.Y., Marston, K.C., Eckert E.R.G. and Goldstein R.J., 1996, "Film Cooling of the Gas Turbine Endwall by Discrete-Hole Injection", J. Turbomachinery, 118, pp. 278-284.

[12] Friedrichs, S., Hodson, H.P. and Dawes, W.N., 1996. “Distribution of Film-Cooling Effectiveness on a Turbine Endwall Measured Using the Ammonia and Diazo Technique”, J. Turbomachinery, 118, pp. 613-621.

[13] Knost, D.G., and Thole, K.A., 2005, “Adiabatic Effectiveness Measurements of Endwall Film-Cooling for a First-Stage Vane”, J. Turbomachinery, 127, pp. 297-305.

[14] Colban, W.F., Thole, K.A., 2007, “Influence of hole shape on the performance of a turbine vane endwall film-cooling scheme”, Int. J. Heat and Fluid Flow, 28, pp. 341-356.

[15] Colban, W., Thole, K. A., and Haendler, M., 2008, “A Comparison of Cylindrical and Fan-Shaped Film-Cooling Holes on a Vane Endwall at Low and High Freestream Turbulence Levels," J. Turbomachinery, 130, pp. 031007-1--031007-9.

[16] Wright, L.M., Gao, Z., Huitao Y., and Han. J-C, 2008, “Film Cooling Effectiveness Distribution on a Gas Turbine Blade Platform With Inclined Slot Leakage and Discrete Film Hole Flows”, J. Heat Transfer, 130, pp. 071702-1-071702-11.

[17] Gao, Z., Narzary, D., Han. J-C, 2009, “Turbine Blade Platform Film Cooling With Typical Stator-Rotor Purge Flow and Discrete-Hole Film Cooling”, J. Turbomachinery, 130, pp. 041004-1--041004-11.

[18] Barigozzi, G., Benzoni, G., Franchini, G., and Perdichizzi, A., 2006, “Fan-Shaped Hole Effects on the Aero-Thermal Performance of a Film Cooled Endwall,” J. Turbomachinery, 128, pp. 43–52.

[19] Barigozzi, G., Fontaneto, F., Franchini, G., Perdichizzi, A., Maritano, M., and Abram, R., 2012, “Influence of Coolant Flow Rate on Aero-Thermal Performance of a Rotor Blade Cascade With Endwall Film Cooling,” J. Turbomachinery., 134, pp. 05138–1-05138–8.

[20] Harasgama, S.P., and Burton, C.D., 1992, “Film Cooling Research on the Endwall of a Turbine Nozzle Guide Vane in a Short Duration Annular Cascade: Part 1—Experimental Technique and Results”, J. Turbomachinery., 114, pp. 734-740.

[21] Nicklas, M., 2001, “Film-Cooled Turbine Endwall in a Transonic Flow Field: Part II – Heat Transfer and Film Effectiveness”, J. Turbomachinery, 123, pp. 720-729.

[22] Jonsson, M., Charbonnier, D., Ott, P., and von Wolfersdorf, J., 2008, “Application of the transient heater foil technique for heat transfer and film cooling effectiveness measurements on a turbine vane endwall”, ASME Paper No. GT2008-50451.

[23] Salvadori, S., Ottanelli, L., Jonsson, M., Ott, P., and Martelli, F., 2012, “Investigation of High-Pressure Turbine Endwall Film Cooling Performance Under Realistic Inlet Conditions”, J. Propulsion and Power, 28(4), pp. 799-810.

[24] Thrift, A.A., Thole, K. A., Hada, S., “Effects of an Axisymmetric Contoured Endwall on a Nozzle guide Vane: Adiabatic Effectiveness Measurements”, *ASME Journal of Turbomachinery*, 2011, Vol. 133, pp. 041007-1-041007-10.

[25] Roy, A., Blot, D., Ekkad, S. V., Ng, W., Lohaus, A. S., and Crawford, M. E., 2013, "Effect of upstream purge slot on a transonic turbine blade passage: Part 2 - Heat Transfer Performance", ASME Paper No. GT2013-94581.

[26] Ekkad, S.V., and Han, J.C., “A transient liquid crystal thermography technique for turbine heat transfer measurements”, *Measurement. Science and Technology*, 2000, Vol. 11, pp. 957-968.

[27] Moffat, R. J., 1988, “Describing Uncertainties in Experimental Results,” Exp. Thermal and Fluid Science, 1, pp. 3-17.

[28] Coleman, H. W., Brown, K. H., and Steele, W. G., 1995, “Estimating Uncertainty Intervals for Linear Regression,” AIAA-1995-0796.

[29] Mick W.J., Mayle R.E., 1988, “Stagnation film cooling and heat transfer, including its effect within the hole pattern”, J. Turbomachinery,110, pp.61-70.

CHAPTER 3 : Heat Transfer Performance of a Transonic Turbine Blade Passage in presence of Leakage Flow through Upstream Slot and Mateface Gap with Endwall Contouring

Proceedings of ASME Turbo Expo 2014
GT 2014
June 16-20, Dusseldorf,
Germany

GT 2014-26476

HEAT TRANSFER PERFORMANCE OF A TRANSONIC TURBINE BLADE PASSAGE IN PRESENCE OF LEAKAGE FLOW THROUGH UPSTREAM SLOT AND MATEFACE GAP WITH ENDWALL CONTOURING

Arnab Roy, Sakshi Jain, Srinath V. Ekkad, Wing F. Ng
Department of Mechanical Engineering, Virginia Tech
Blacksburg, Virginia, USA

Andrew S. Lohaus, Michael E. Crawford
Siemens Energy, Inc.
Orlando, Florida, USA

ABSTRACT

Comparison of heat transfer performance of a non-axisymmetric contoured endwall to a planar baseline endwall in presence of leakage flow through stator-rotor rim seal interface and mateface gap is reported in this paper. Heat transfer experiments were performed on a high turning (~127°) turbine airfoil passage at Virginia Tech's transonic blow down cascade facility under design conditions (exit isentropic Mach number 0.88 and 0° incidence) for two leakage flow configurations – 1) mateface blowing only, 2) simultaneous coolant injection from the upstream slot as well as mateface gap. Coolant to mainstream mass flow ratios (MFR) were 0.35% for mateface blowing only, whereas for combination blowing, a 1.0% MFR was chosen from upstream slot and 0.35% MFR from mateface. A common source of coolant supply to the upstream slot and mateface plenum made sure the coolant temperatures were identical at both upstream slot and mateface gap at the injection location. The contoured endwall geometry was generated to minimize secondary aerodynamic losses. Transient IR (Infrared) thermography technique was used to measure endwall surface temperature and a linear regression method was developed for simultaneous calculation of heat transfer coefficient (HTC) and adiabatic cooling effectiveness (ETA), assuming a 1D semi-infinite transient conduction. Results indicate reduction in local hot spot regions near suction side as well as area averaged HTC using the contoured endwall compared to baseline endwall for all coolant blowing cases. Contoured geometry also shows better coolant coverage profiles further along the passage. Detailed interpretation of the heat transfer results along with near endwall flow physics has also been discussed.

INTRODUCTION

In modern gas turbine engines the airfoils on the hub section are cast as a single unit as shown in Figure 32(a). These individual parts are joined together circumferentially on the wheel-space to form the annular section of turbine blade rows as shown in Figure 32(b).

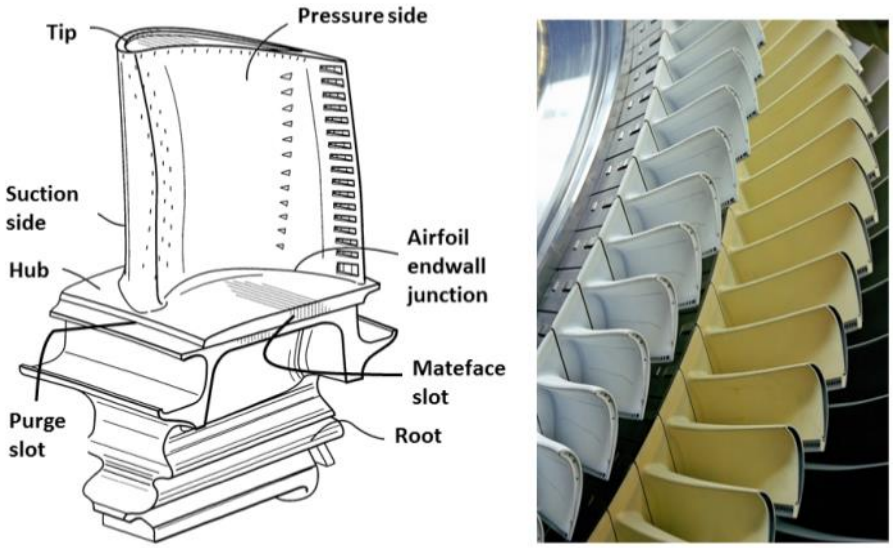

Figure 32: Turbine assembly features [1,2]

Figure 32 also shows several gaps due to turbine assembly feature – stator-rotor interface and the gap along the mating hub endwall surfaces of adjacent airfoils. Supply of high pressure coolant air is necessary to purge through these interfaces in order to prevent hot mainstream gas ingestion into the turbine core section. The leakage flow also protects the hub endwall from direct contact with the hot gas by creating a thin layer of film which reduces the heat load to the platform. Although, any leakage flow tapped from high pressure compressor introduces aerodynamic penalty, the coolant injection is essential with increasing turbine inlet temperatures for modern gas turbine engines. Current operating temperatures are well beyond metal melting point of the airfoil and endwall material. The chord-wise gap between the adjacent airfoils/endwall castings is often referred as mateface gap. These leakage gaps are also subjected to extremely high thermal stresses due to observed higher temperature gradients.

RELEVANT LITERATURE REVIEW

Endwall contouring has been widely studied by several researchers in the past decade as an effective tool to control secondary flow and minimize aerodynamic losses. While most of the existing literature discusses benefits of contouring from the perspective of aerodynamic performance, there are limited studies available that explain the

associated heat transfer performance both with and without considering leakage flows. Majority of the heat transfer literature pertaining to endwall contouring along with cooling features emphasize on upstream leakage flow and has been summarized in [3]. The following section presents a brief literature review specifically on endwall heat transfer in presence of leakage flow through mateface gap (with and without endwall contouring).

Experiments performed by Yamao et al. [4] is one of the first known studies on endwall cooling designs incorporating leakage flow through mid-passage gap. They reported improvement in film cooling effectiveness with increase in stator-rotor leakage flow as well as sealing flow through mateface gap. Aunapu et al. [5] incorporated a novel endwall flow modification technique in order to simulate the inter passage leakage for a turbine vane. They used hub endwall jets to modify the secondary flow within the passage and were successful to alter the trajectory of the pressure side leg of the horse-shoe vortex from meeting the suction side of the airfoil. However, there was no major effect on the strength of the passage vortex. Approximately 2% coolant mass flow ratio per passage was required to change the secondary flow path; however, the jets resulted in 30% increase in aerodynamic losses due to turbulent mixing of the jets into the mainstream flow. They concluded that overall aerodynamic performance highly depend on leakage flow from hub endwall surface. Extensive studies have been performed by Piggush and Simon [6-8] on endwall contouring and associated flow and thermal measurements in presence of several turbine assembly features. Piggush and Simon [6] found out that using an axi-symmetric endwall contouring results in weaker secondary flow, hence better aerodynamic performance can be expected. However, leakage flow from slash-face gap was a significant parameter affecting exit total pressure loss. Subsequent studies on the effect of endwall heat transfer [7,8] revealed presence of slash-face gap increased overall heat transfer coefficient. Heat transfer enhancement was observed locally near both front and aft part of the gap due to endwall pressure gradient and coolant flow path in comparison to a passage without the gap. Adiabatic effectiveness measurements were carried out on the same cascade by Piggush and Simon [9] and the study concluded that there is little benefit in terms of coolant coverage with increase in slash-face gap leakage flow rate compared to a nominal flow rate. Ranson et al. [10] investigated all possible endwall cooling features on a turbine blade passage (leakage flows) experimentally and compared with computational predictions. Their study involved leakage flows from front slot (upstream purge), aft slot and featherseal. Experiments with varying leakage flow rates from all slots were performed and results concluded that upstream slot leakage flow rate is the most important parameter dominating over cooling features considering coolant coverage on the endwall. Their study also showed that no added cooling benefits can be obtained with increase in leakage flow rate through the featherseal. The reversal of featherseal coolant coverage from pressure side near the front section towards suction side near the aft part was an important observation. Reid et al. [11] investigated the aerodynamic performance of chord-wise inter-platform leakage flows in a vane test section and reported a stage efficiency penalty of 0.5%-1.5% depending on the sealing arrangement. Computational predictions on pitchwise and spanwise flow angles were compared with experimental data. Reid et al.[12] also reported on the location of the inter-platform gap relative to the passage and concluded that gaps located closer to the pressure side of the endwall achieves better performance. Cardwell et al. [13] performed detailed experiments simulating the interface between the combustor and first stage nozzle guide vane along with mid-passage gap and endwall film cooling features. Variation of adiabatic effectiveness levels were reported for the following cases -

rough endwall and three geometrical designs for mid-passage gap (aligned, cascade and dam). They recommended cascade alignment to be the best design from heat transfer performance standpoint. However, the upstream slot purge flow was varied in their experiments and no leakage flow through the mid-passage gap was considered. Endwall film effectiveness levels were studied by Cardwell et al. [14] in a study by varying the upstream slot width as well as varying the mid-passage gap flows. Their conclusions were also similar to Ranson et al. [10], which showed that with increase in gap leakage flow rates there is no appreciable difference on endwall coolant coverage. The computational predictions performed by Hada and Thole [15] for a vane endwall film cooling were in fair agreement with experimentally measured adiabatic effectiveness distribution. The major significance of mateface gap flow was observed downstream of the suction side.

The experimental study performed by Lynch and Thole [16] is the only paper that reported endwall heat transfer coefficient distribution (in terms of Stanton number) in presence of mid-passage gap leakage and varying gap flow rates. They reported higher endwall Stanton numbers locally near the vane passage throat region with the presence of mid-passage gap compared to a smooth endwall. They also concluded that overall endwall heat transfer levels remain marginally affected with increase of mid-passage leakage flow rate up to 0.5%.

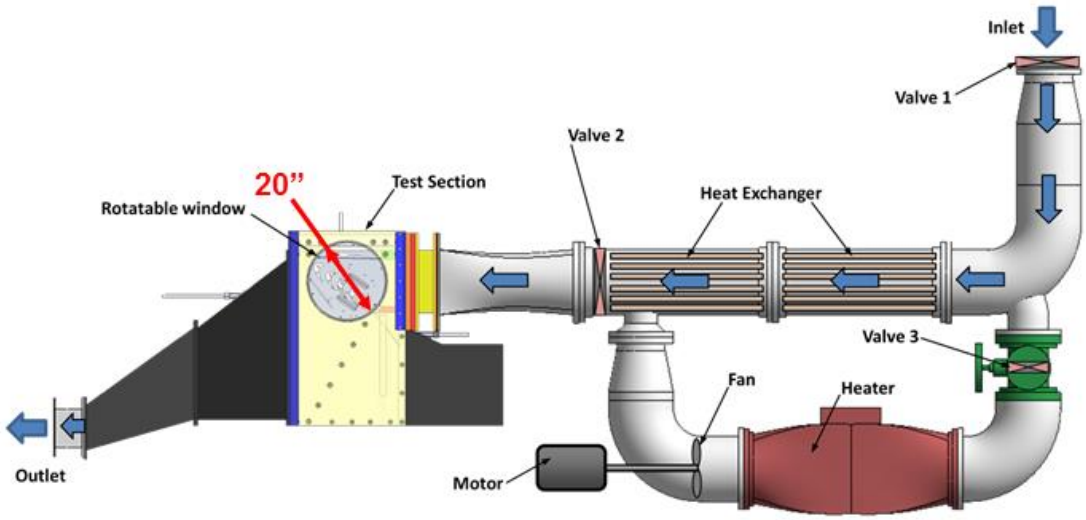

Figure 33: Virginia Tech Transonic Cascade facility

The brief literature survey presented above shows that only limited studies have been performed on mateface leakage effects in conjunction with endwall contouring. The background study also reveals that almost the entire body of published work [4-16] has been conducted at low speed conditions. In order to simulate the aero-thermal performance of realistic gas turbine engine environment, matching Reynolds number is not enough. High speed flow and operation near transonic conditions might have a significant impact on endwall heat transfer parameters.

The study on endwall heat transfer under transonic operating conditions with endwall contouring was first performed by Panchal et al. [17] and the best performing endwall contour design was chosen for subsequent heat transfer analysis on upstream purge flow was carried out by Roy et al. [3].

The present paper reports continuation and further development work by Roy et al. [3] introducing leakage flow through the mateface gap. All experiments were performed at design isentropic exit Mach no. 0.88 and design incidence angle for a high turbine blade passage with the aero-optimized endwall contour. Detailed heat transfer analysis of the contoured endwall relative to a baseline planar endwall is reported in this article. The other important feature of the paper is the data reduction methodology which calculates heat transfer coefficient and film cooling effectiveness simultaneously from a coupled set of experiments.

EXPERIMENTAL METHODOLOGY

Experimental Test Facility

Figure 33 shows a schematic of the linear transonic blow-down facility at Virginia Tech. A reference dimension has been given to provide an idea about the scale of the set up. Detailed description of the facility, working principle, instrumentation, measurement capability and heat transfer testing procedure has been elaborated in previous papers [3,17] and hence is not repeated here.

Test section details

Figure 34 shows the 5-blade 4-passage cascade test section for the baseline geometry. The turbulence grids are located at 5.5-Cax from the center airfoil which produces about 8% inlet free stream turbulence intensity measured at 0.5-Cax upstream of the leading edge. The head board and tail board angles are adjusted in such a way to maintain flow uniformity through the two middle passages in the cascade.

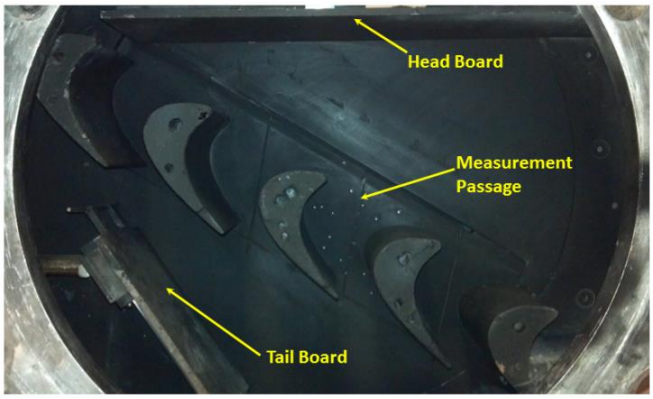

Figure 34: Cascade test section Baseline geometry with Mateface and Purge slot

The mateface gap design details are presented in Figure 35. The upstream slot is located 0.3-Cax upstream of the airfoil leading edge and the mateface gap starts from the upstream slot and extends through 0.1-Cax after the trailing edge. The gap width is about 0.03-Cax and coolant is fed through a series of holes that eject coolant normally to the gap walls. The upstream slot design details have been discussed previously in [18].

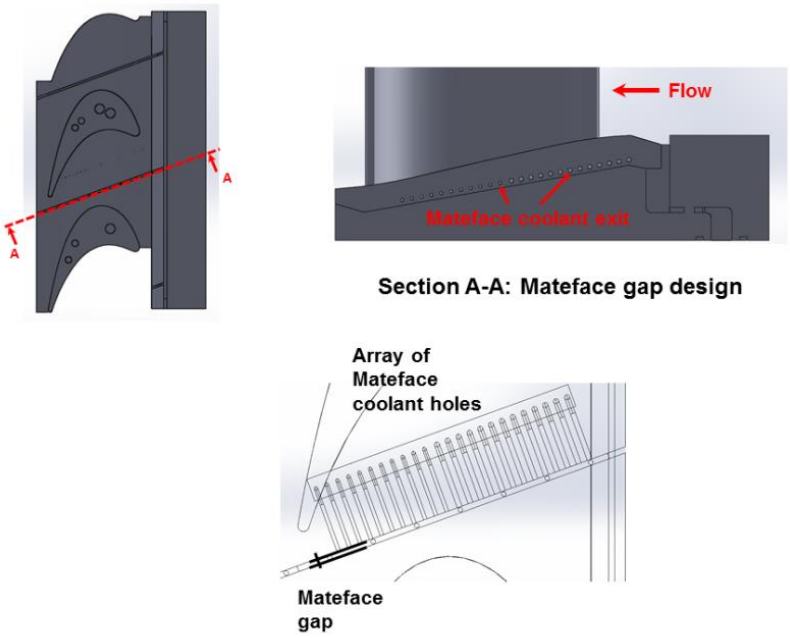

Figure 35: Mateface gap design

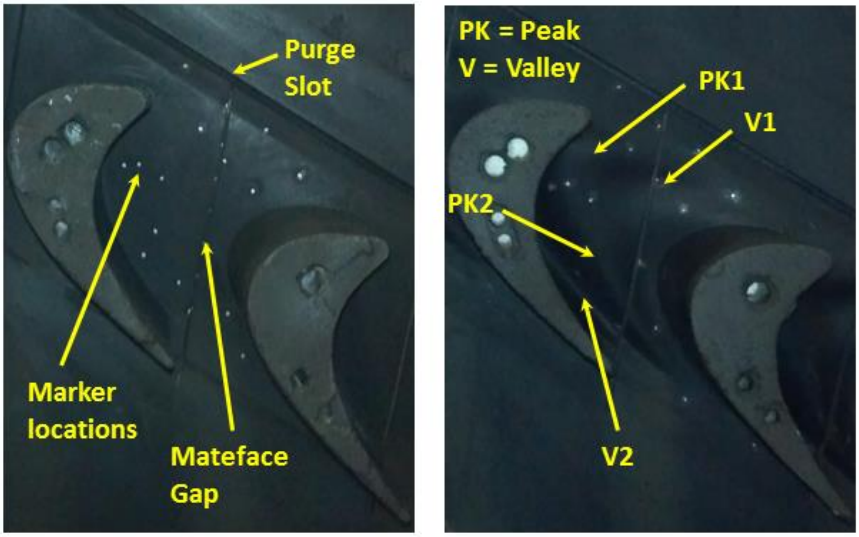

Baseline Endwall **Aero Optimized (AO) Endwall**

Figure 36: Endwall contour designs

The endwall contour profiles as well as leakage flow designs shown in Figure 36 were provided by Siemens Energy Inc. and minor modifications were done in order to suit the hardware for fabrication and set up. The leakage flow designs were kept identical for both geometries for consistency. The locations of peak and valley regions are highlighted for the aero-optimized (AO) endwall. Further details of the design procedure and surface modification features are provided in Panchal et al. [19].

Figure 37 represents a schematic of the cooling system at the rear of the test section. Two separate plenums are used for mateface leakage and upstream purge flow. The coolant is provided from the same source to both plenums in order to maintain identical coolant temperatures for both mateface and upstream leakage flow.

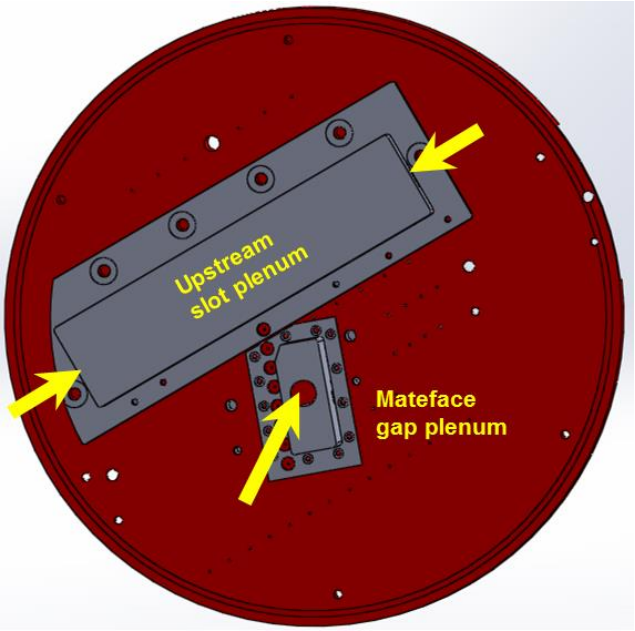

Figure 37: Coolant plenums for leakage flows

Heat transfer measurement technique

Figure 38 shows the heat transfer experimental set up. As shown in Figure 38, to make surface temperature measurements using an infrared camera, two rectangular windows slots were fabricated with a line of sight to the endwall surface being studied. Due to the large forces seen in a transonic facility, the window also needed to be structurally sound. Therefore, Zinc Selenide windows were used as to satisfy the design constraints. Only one window was used at a time for endwall temperature measurements while the other window was closed using a piece of lexan block. All the inner surfaces of the test section and outer surfaces of the test-section window were painted using a flat black paint to increase emissivity of the surface and to avoid thermal reflection from other surfaces. Further details on the measurement procedure with typical surface temperature history are provided in Roy et al. [18].

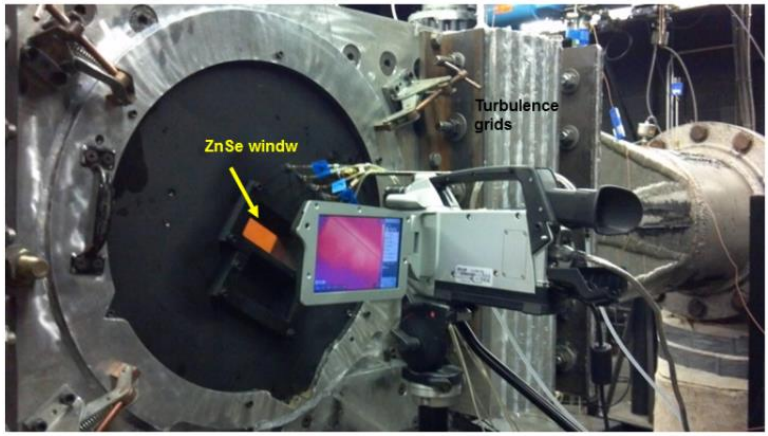

Figure 38: Cascade heat transfer experimental setup

Heat transfer measurement theory

The material of the endwall and the airfoils is Acrylonitrile butadiene styrene (ABS) that has low thermal conductivity. Since the reducible data is obtained only over a short duration ($\Delta t = 5s$), the thermal penetration length into the endwall in any direction is about 0.8mm. Other modes of heat transfer e.g. radiation can be safely neglected as the maximum operating range of the endwall surface temperatures is about 60^{o}C. The paint film thickness is so small (order of microns) compared to endwall dimensions, conduction in the transverse direction through the paint coating is assumed to be negligible. Therefore, the 1-D, semi-infinite heat transfer assumption is applicable at each location on the endwall.

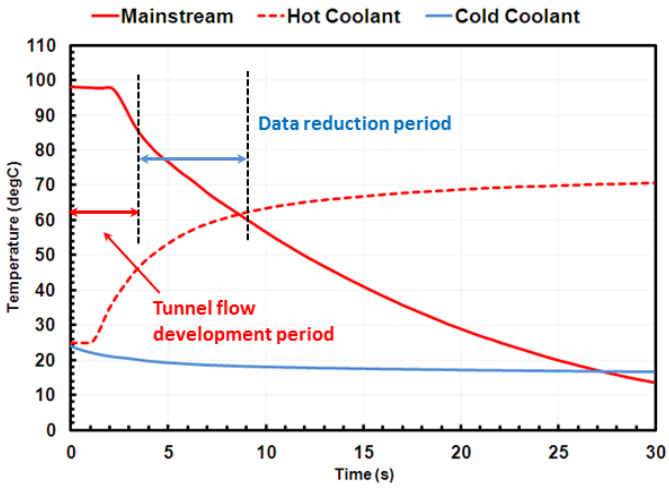

Figure 39: Mainstream and coolant temperature variation

Moreover, significant cool down times in between runs were allowed so the endwall is at a uniform initial temperature at the start of every tunnel run. The infrared camera used, ThermaCam SC325, at a resolution of 320x240, can measure 76800 surface temperature locations simultaneously with a 0.6mm x 0.6mm cross section for

an individual pixel. Due to 1-D semi-infinite assumption, results obtained for each individual pixel is assumed to be independent of the other.

Uncooled heat transfer

Based on the transient characteristic of Virginia Tech Transonic Wind Tunnel as shown in Figure 39, the heat transfer data processing method developed by Smith et al. [20] was used to determine the convective heat transfer coefficient. In this method the surface temperature data is used as a direct boundary condition. Thus, the governing heat transfer model can be described as in Eq. (1).

$$\begin{cases} \dfrac{\partial T}{\partial t} = \alpha \dfrac{\partial^2 T}{\partial x^2} \\ T|_{x=0} = T_w \\ T|_{x\to\infty} = T_i \\ T|_{t=0} = T_i \end{cases} \tag{1}$$

The surface heat flux q can be reconstructed through multiple ways. In the present study the heat flux is calculated by solving the 1-D conduction equation numerically through a finite difference code. Once the surface heat flux is reconstructed, the convective heat transfer coefficient can be estimated equating the calculated heat flux at the surface.

The 1-D surface convection model is:

$$q" = h(T_\infty - T_w) \tag{2}$$

In case of compressible flow domain the mainstream temperature T_∞ has to be replaced by the local recovery temperature, T_r , so the convective equation becomes

$$q" = h(T_r - T_w) \tag{3}$$

Rearranging this equation, we can get a linear relationship in the form: $\boldsymbol{y = ax + b}$:

$$\underset{\text{y}}{q"} = \underset{\text{a}}{h}\underbrace{(T_t - T_w)}_{\text{x}} + \underbrace{h(T_r - T_t)}_{\text{b}} \tag{4}$$

T_t is the total temperature of the bulk fluid flow, and varies at each time step. According to the definition of recovery temperature:

$$T_r = T_t - (1 - r)\frac{{u_\infty}^2}{2C_p} \tag{5}$$

The value of the last term in Eq. (4), $h(T_r - T_t)$, depends only on the aerodynamic condition, and remains constant if the local Mach number does not change within the calculation time window. Theoretically, all the data points should lie on a straight line, as shown in Figure 40. Equation (4) is plotted in Figure 40 with Y and X axis data normalized w.r.t. T_t. This is necessary to impose the condition that 'b' is a constant and independent of time.

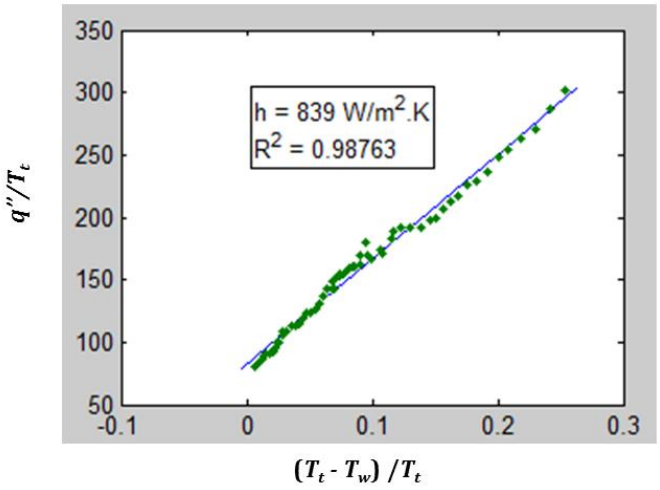

Figure 40: Linear regression method for uncooled heat transfer (sample data)

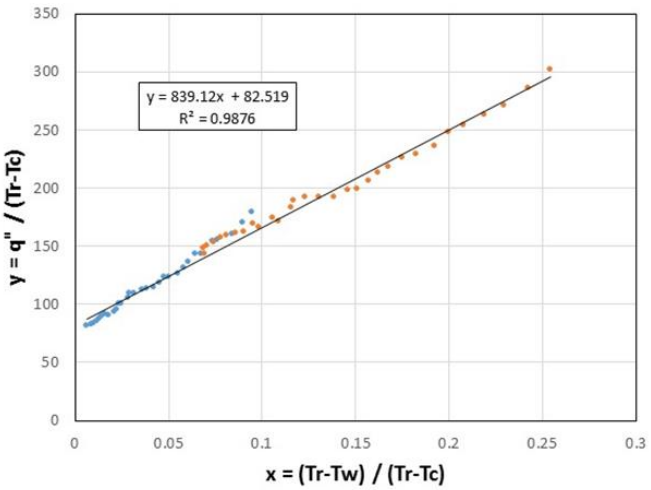

Figure 41: Linear regression method for film cooled heat transfer (sample data)

The slope of this line provides HTC, and the recovery temperature can be estimated from the y intercept value as $T_r = T_t - \frac{y}{a}\Big|_{x=0}$

Film cooled heat transfer

The governing physical model equations and assumptions remain the same for film cooled cases as well. However, film cooling is a three-temperature problem with the wall temperature, mainstream temperature and coolant temperature as important factors. Adiabatic effectiveness (η) is a key parameter quantifying the spread of the coolant film on the target surface and is defined as:

$$\eta = \frac{T_r - T_{aw}}{T_r - T_c} \tag{6}$$

Where T_{aw} is the adiabatic wall temperature, which is equal to the near wall film flow temperature, T_f. In the compressible flow domain, the mainstream temperature should be replaced by the recovery temperature, T_r. The convective heat flux is therefore defined as:

$$q" = h(T_f - T_w) \tag{7}$$

In the experiments, heat flux q, is calculated using Finite Difference method as described in the previous section and wall temperature T_w is measured directly using the IR camera. However, heat transfer coefficient h and adiabatic wall temperature T_{aw}, are unknowns. To solve for heat transfer coefficient simultaneously, Eq. (7) is rearranged in the following manner after incorporating the definition of adiabatic effectiveness shown in Eq. (6).

$$\frac{q"}{T_r - T_c} = h\frac{T_r - T_w}{T_r - T_c} - h \cdot \eta \tag{8}$$

Where, the recovery temperature is a function of local Mach number and bulk mainstream fluid temperature and expressed as,

$$T_r = T_t + r\frac{(\gamma - 1){M_a}^2}{2} \tag{9}$$

The data processing technique is a two-test strategy called Dual-Coolant Linear Regression Method, because it uses two sets of experimental data for surface temperature in the calculation. These two sets of data are recorded at the same aerodynamic conditions with the same mean flow Mach number, the same coolant blowing ratio, and similar mainstream flow total temperature, but coolant temperatures are different. Both heat transfer coefficient and film effectiveness being hydrodynamic parameters, should remain the same during these two tests. Effect of coolant to mainstream density ratio effect is however, considered negligible in the range of operating conditions. To go

through the calculation, a tentative guess of T_r value must be given and the optimization algorithm then calculates the best possible local Mach number that satisfies both the hot and cold coolant run for a particular location. The two sets of data can be plotted with $x = \frac{T_t - T_w}{T_t - T_c}$, and $y = \frac{q}{T_t - T_c}$, as shown in Figure 41. The cold run points are shown as blue dots and the hot run points are shown as red dots. Similar to the uncooled heat transfer case the slope provides the heat transfer coefficient value and cooling effectiveness is calculated from the y-intercept.

The overall uncertainties in heat transfer coefficient and adiabatic effectiveness are 8% and 5% respectively based on methods described by Smith et al. [20].

Data Representation

The basic data representation technique which involves mapping of two-dimensional raw HTC data onto three dimensional endwall surface using camera transformation matrix and image stitching was developed by Panchal et al. [17] and is not repeated here. This technique was further used for representing ETA values on a three-dimensional endwall similarly.

RESULTS AND DISCUSSION

Table 3 shows the test cases that have been performed on both baseline and aero-optimized endwall geometries. The results discussed in this section are arranged in the following manner – First, the effect of presence of the mateface gap has been examined and compared with an existing case having no mateface gap [3] with and without coolant flow. Second, heat transfer characteristics have been elaborated for both endwall geometries corresponding to with and without leakage cases described in Table 3. Finally, quantitative comparison between both endwall geometries has been described based on overall thermal performance. It is important to mention at this point that, all heat transfer results shown in the following sections have been normalized (HTC normalized by area averaged HTC upstream of slot and adiabatic effectiveness normalized by maximum value over the area) due to proprietary nature of the data.

Table 3: Test cases for both baseline and Aero-Optimized endwall

	Mateface leakage	Purge flow
Case 1	No gap	0%
Case 2	No gap	1%
Case 3	0%	0%
Case 4	0.35%	0%
Case 5	0.35%	1%

Effect on endwall heat transfer in presence of mateface gap

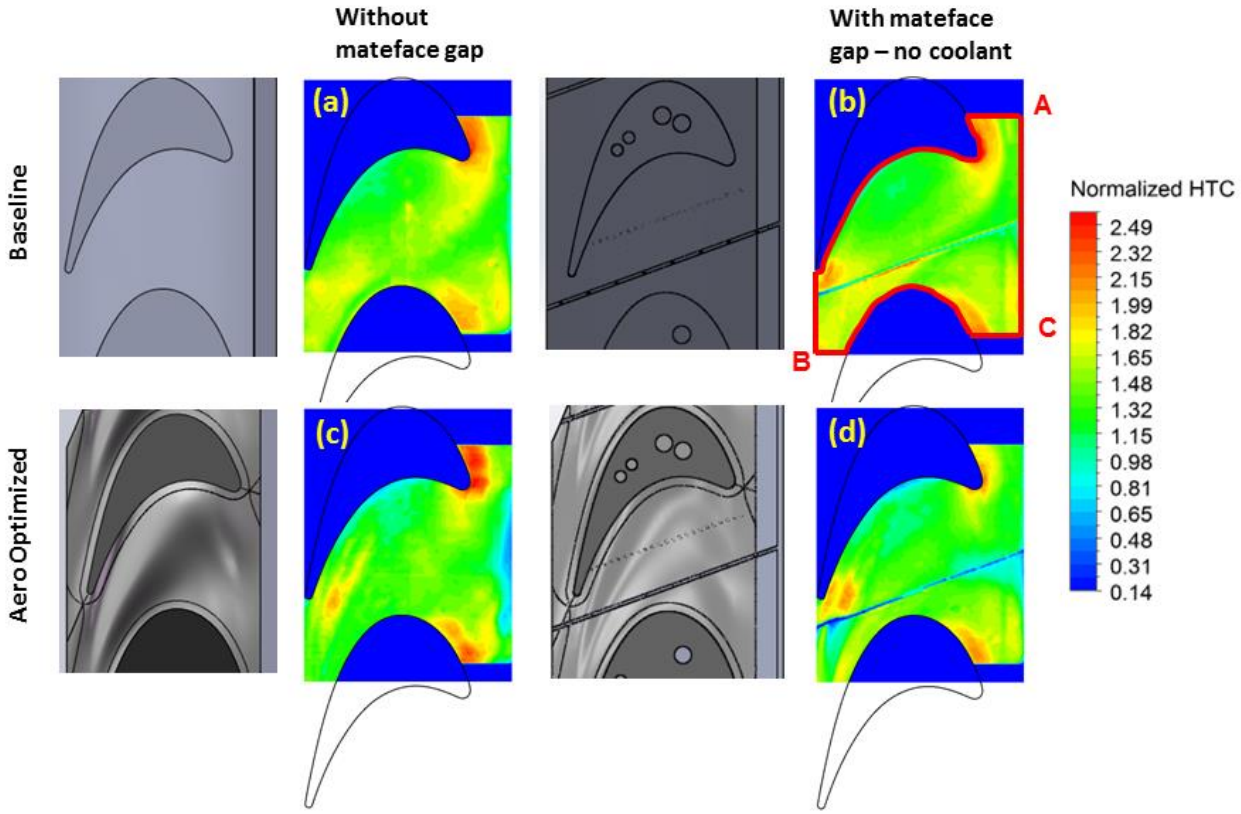

Figure 42: Normalized heat transfer distribution showing effect of the mateface gap (Cases 1 & 3)

Figure 42 shows contours of normalized endwall HTC distribution for the baseline and Aero-Optimized geometry without coolant (Cases 1 and 3 in Table 1). It is to be noted that, in actual engine conditions both purge slot and mateface gap are present and leakage flow necessary for sealing purposes; however, the cases presented in Figure 42 is intended to show the isolated effect of the presence of mateface gap on endwall heat transfer. For baseline geometry an increase in endwall heat transfer is observed near suction side of the platform when compared to a continuous passage, starting from the throat region extending up to the trailing edge. This can be contributed due to the mainstream flow ingress into the mateface gap. Other characteristic features of baseline endwall can also be observed such as development of pressure and suction side leg of horse-shoe vortex and cross passage flow due to pressure gradient from pressure to suction surface. It can also be observed that the general benefit of contouring to achieve lower endwall heat transfer is obtained for both with and without mateface gap. The contoured endwall was designed to minimize secondary aerodynamic losses, hence performed better than the baseline counterpart as endwall heat transfer is highly dependent on the secondary flow vortex formation and its trajectory along the passage. Comparing Figure 42(b) and (d) shows lower heat transfer coefficient values from mid-passage to trailing edge near suction side platform in case of AO endwall. The further reduction in HTC near the trailing edge for the AO endwall can be attributed due to egress of the ingested mainstream flow through the mateface gap.

Adiabatic effectiveness with and without mateface gap

Endwall film cooling effectiveness distributions for three measurement cases – with purge flow only, with mateface flow only and combined purge and mateface blowing, (Cases 2, 4 and 5 in Table 3) are shown in Figure 43 (a)-(f) for both baseline and AO endwall. The upstream purge cooling case without the mateface gap is carried out with 1.0% leakage flow, whereas, 0.35% coolant flow is used for mateface blowing only. For the combined leakage flow experiment, 1.0% upstream slot flow and 0.35% mateface gap coolant flow has been considered. The percentage refers to the mass flow ratio (MFR) between coolant flow rate and mainstream flow rate per passage. Adiabatic effectiveness contours provide a quantitative measure of the coolant film spread on the endwall surface and it has been established by several researchers before, that upstream purge cooling plays a dominant role in platform cooling over other cooling features. The effect of varying purge cooling flow rates has been discussed in detail previously [3] with the same experimental set up, hence is not repeated here. Only the representative case of 1.0% MFR for both endwall geometries has been chosen from [3] for comparison.

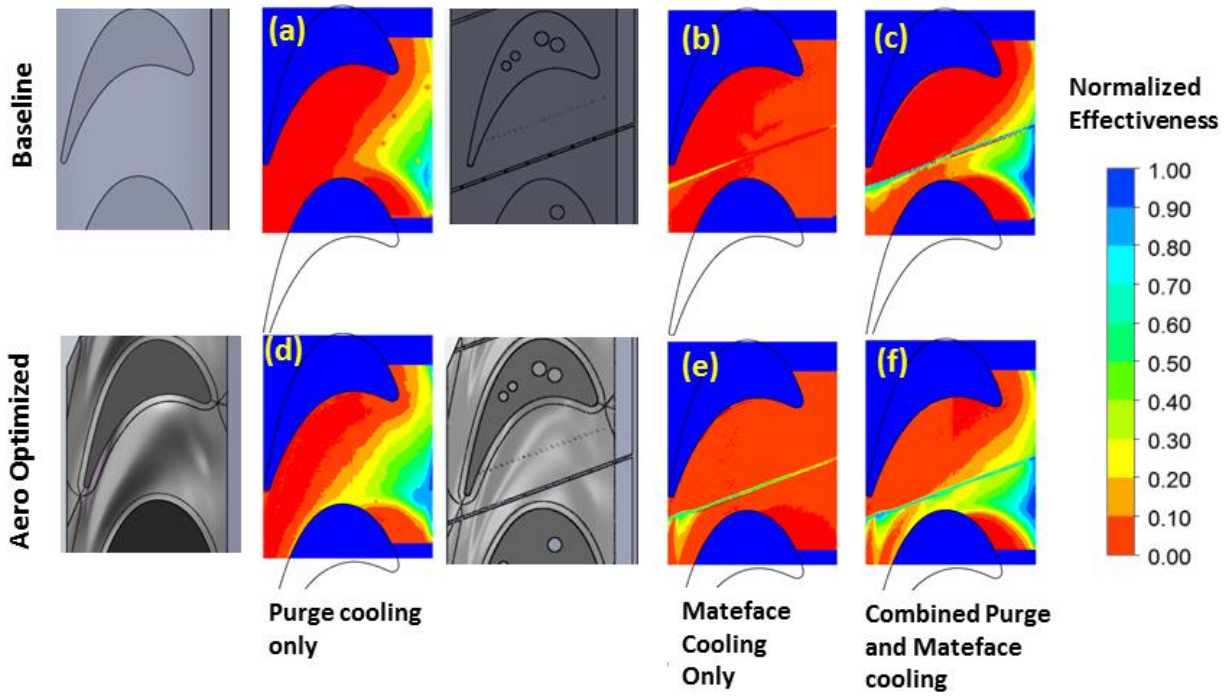

Figure 43: Endwall Adiabatic Effectiveness for all leakage cases (Cases 2, 4 and 5)

The film effectiveness pattern when upstream slot blowing is considered, more evidently for baseline geometry (Figure 43(a-c)) displays a general feature of being entrained within a V-shaped stagnation region upstream of the passage. This is due to formation of horse-shoe vortex and subsequent bifurcation into pressure side and suction side leg upstream of the leading edge. The coolant stream ejecting from the upstream slot does not possess enough momentum to penetrate through the pressure side leg of the horse-shoe vortex, which grows in strength while consuming energy from the mainstream flow along its trajectory towards the suction side of the adjacent airfoil. The cross passage pressure differential further moves the coolant injected upstream towards the suction side. When

mateface flow is combined with the purge cooling (Figure 43(c)), an immediate effect that can be observed is that the mateface leakage provides some coolant coverage near the suction side aft portion, whereas without mateface gap there is essentially no coolant coverage after mid-passage. The coolant spread region, however is not able to extend all the way up to the suction side airfoil-endwall junction due to mixing between mainstream and mateface leakage jet. Another effect of mateface flow that can be noted is that the coolant spread near the upstream slot stagnation region is slightly narrower; however, coolant is observed almost up to the throat region compared to upstream purge flow only. This can be attributed due to ingestion of slot coolant into the mateface gap which reduces film effectiveness near the pressure surface. Mateface coolant has a pronounced effect on the suction side of the platform due to inherent pressure distribution that drives the secondary flow from pressure side to the suction side of the airfoil. As described by Ranson et al. [10], near the front portion of the mateface gap, the coolant is pushed towards the pressure side of the platform to a little extent due to the direction of the high momentum mainstream flow. The same comment is inconclusive for the present case as the passage inlet region is highly dominated by slot coolant, isolating the effect of mateface flow is difficult. However, it is evident that adding mateface leakage flow has no beneficial effect on cooling near the pressure side. Interaction between the mainstream passage flow and the mateface gap leakage flow can be described from [14] as follows – starting from the inlet up to the throat region, the mainstream flow can be considered to be aligned with the mateface leakage. However, the coolant is unable to penetrate the high momentum mainstream flow and pushed more towards the trailing edge along the mateface gap. The mateface flow downstream is able to eject outwards as the endwall pressure distribution overcomes the inlet flow momentum. Near the trailing edge, the mainstream flow is almost perpendicular to the mateface which sweeps away the coolant. It is important to mention that the relative spreading of the coolant is highly dependent on the location of the mateface gap w.r.t. the passage and also on airfoil design.

The isolated effect of leakage flow through the mateface gap only has also been investigated (Case 4 in Table 3). The baseline geometry shows almost no effectiveness up to mid passage confirming hot gas ingestion into the mateface gap due to higher endwall static pressure distribution. Towards the trailing edge, some effectiveness is observed though limited only within the mateface gap. There is a sharp contrast between adiabatic effectiveness distribution comparing the baseline and AO endwall comparing Figure 43(b) and (e). The front section of the mateface gap for AO endwall almost resembles the rear part of the baseline endwall and near the trailing edge coolant streaks are visible on the endwall. This can explained due to two major reasons – first, the endwall static pressure near the front section of the AO endwall may be slightly lower than the baseline and the ridge of the contour starting from the pressure side of the airfoil extending almost up to trailing edge of the airfoil minimizes the strength of the secondary flow sweeping away the coolant from the mateface gap.

Benefits of endwall contouring on film cooling effectiveness can be observed considering both with and without mateface leakage (upstream flow only). As shown in Figure 43(a) and (d), with 1.0% MFR purge cooling only, contouring helps the coolant stream is to adhere to the endwall further along the passage direction almost up to the suction side airfoil-endwall junction. Larger region of the endwall can be cooled with contouring as the entrainment of the coolant inside the passage vortex is minimized and strength of the passage vortex is also weakened. This

explanation holds true for the case of combined leakage flow as well. The AO endwall shows much improved effectiveness profile on the suction side of the platform from inlet to the trailing edge; however, near the upstream region, the coolant spread is not able to penetrate the suction side leg of the horse-shoe vortex. Upstream leakage is again the most dominant form of the cooling up to the mid-passage region and mateface leakage is the major contributor towards cooling near the downstream region. The primary reason for coolant being drawn towards the suction side for AO endwall is believed to be the pressure differential between the coolant stream and the suction side of the airfoil as the cross passage flow is redirected further downstream generating from the pressure side of the airfoil.

Effect of leakage flows on endwall heat transfer with and without contouring

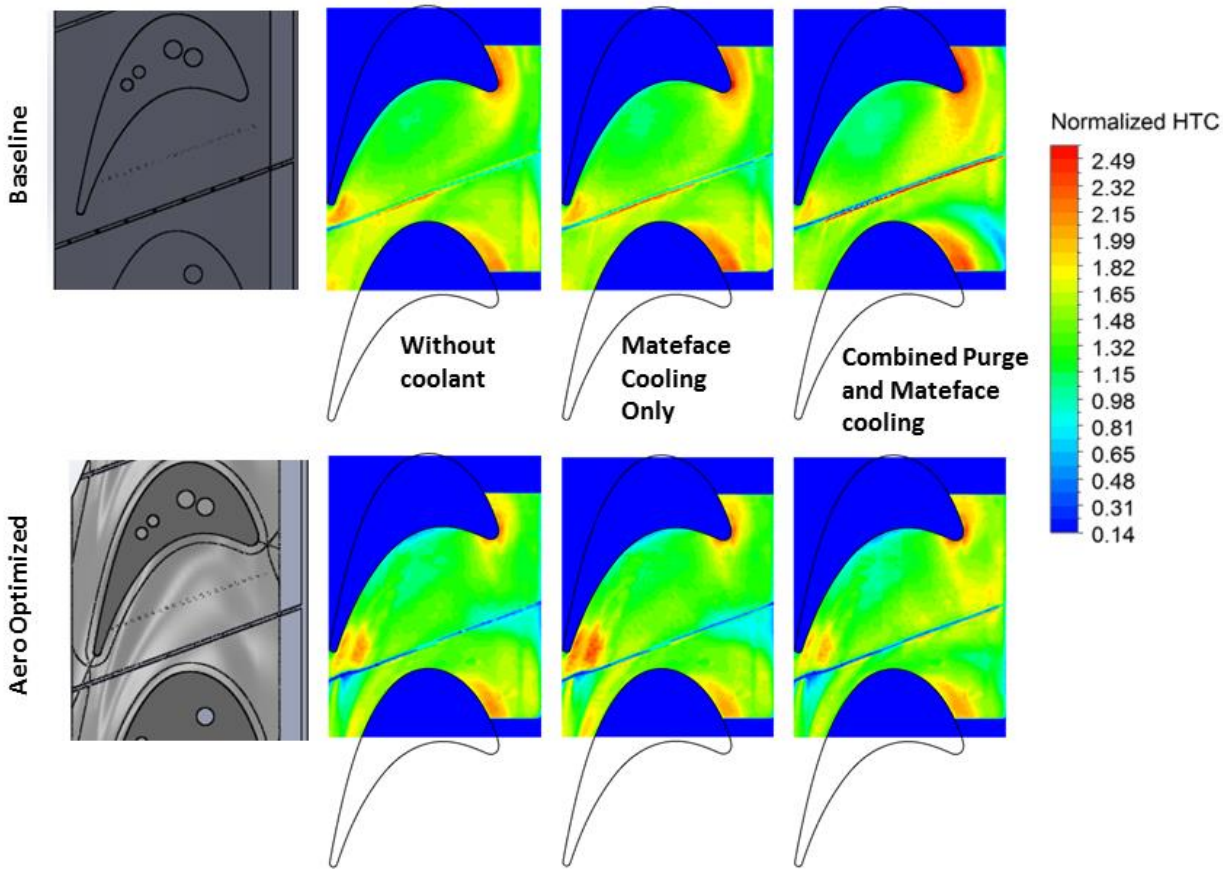

Figure 44: Normalized endwall heat transfer coefficients for all mateface cases (Cases 3-5)

Figure 44 shows the normalized endwall heat transfer coefficient distribution for only mateface leakage and combined purge and mateface leakage for both baseline and AO endwall geometries. Table 4 summarizes the comparative performance of area averaged HTC values considering Baseline (with purge slot and mateface gap) geometry without any coolant blowing. The region bounded by A-B-C is considered for area averaging HTC as shown in Figure 42(b). Reduction in area averaged HTC occurs for all cases using the contoured endwall, with the no coolant case performing the best (almost 10% reduction). Introduction of leakage flow seems to increase heat

transfer coefficients on the AO endwall. However, it is less than 5% which is comparable to HTC measurement uncertainty levels and therefore, no definite conclusions can be drawn. Locally, just downstream of the slot (Case 5), there is an increase in HTC levels close to the intersection of the mateface gap and upstream slot seen for both baseline and AO endwall. This is due to coolant injection into the incoming boundary layer creating additional turbulent mixing, heat dissipation and increased near wall velocity. Interestingly, the area averaged heat transfer levels remained similar for all baseline geometry leakage flow cases compared to without coolant. Controlling the formation and trajectory of complex vortices along with secondary flow is the key to minimize hot gas entrainment towards the platform and hence serves as the basis of design for endwall contour profiles. The detailed explanation behind the general heat transfer reduction using the aero-optimized geometry has been provided in [3,17].

Table 4: Area averaged heat transfer comparison

	No coolant	Mateface leakage only	Combined purge and leakage
Baseline	-	1%	1%
AO	-10%	-7%	-6%

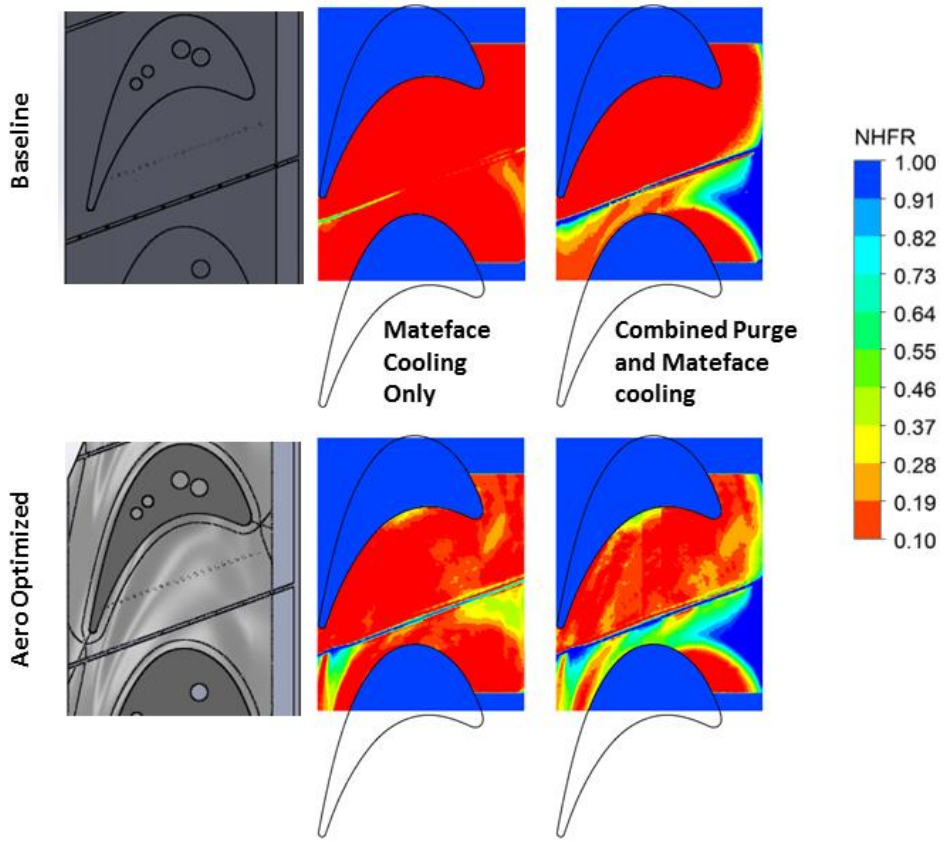

Figure 45: Net Heat Flux Reduction for mateface leakage cases (Cases 4 and 5)

Another way of quantifying the net reduction of heat load (NHFR) on the platform is to combine the adiabatic effectiveness and heat transfer coefficient distribution for a leakage flow along with heat transfer coefficient distribution of a reference case having no net coolant leakage. The mathematical expression for NHFR is given as,

$$\text{NHFR} = 1 - \frac{h_f}{h_{ref}}\left(1 - \frac{\eta}{\varphi}\right) \tag{10}$$

Where, φ is a non-dimensional metal temperature defined as overall cooling effectiveness. An average value of φ = 0.6 was first introduced by Mick and Mayle [21]. Majority of the film cooling studies have been using φ = 0.6 since then for NHFR calculation. The average value of 0.6 originates considering realistic gas turbine inlet, metal and coolant temperatures. For the present experimental study the calculated φ values are within 10% deviation from 0.6. The major focus of this paper is to present a comparative study of heat transfer performance between two endwall geometries. Therefore, a quantitative analysis can still be performed on a "delta basis" with identical reference level to show the benefits of using a properly contoured endwall. Figure 45 shows the local NHFR distribution for all leakage cases (mateface and combined flow). Significant improvement in NHFR is obtained using the contoured geometry, especially the platform region bounded within mateface gap and suction side of the airfoil for the combined leakage flow case. The major contributor to the NHFR along the suction side of the platform is the adiabatic effectiveness distribution. There is some reduction in heat flux near the pressure side of the platform as well which occurs due to altering the passage vortex flow path in case of the AO endwall. In case of the mateface only leakage for AO endwall, apart from expected improvement in NHFR near the trailing edge due to coolant spread, heat load reduction can also be observed near the region just downstream of the slot within the stagnation zone. This is caused due to lower HTC levels at these locations for the AO endwall with mateface leakage only.

CONCLUSIONS

Endwall heat transfer measurements have been performed in presence of leakage flows from mateface gap and upstream purge slot (isolated and combined) and the effect of endwall contouring on thermal performance has been investigated. Comparison without the mateface gap – both with and without coolant has been discussed in detail. The key heat transfer parameters – heat transfer coefficient and film cooling effectiveness was calculated simultaneously from a coupled set of experimental data using a novel Linear Regression Method.

In general, endwall contouring benefits in reduction of overall area averaged heat transfer coefficient for all with and without leakage flow cases due to secondary flow control. However, local enhancement of heat transfer can be observed just downstream of the purge slot due to turbulent mixing of the coolant jet with the mainstream. Although, purge cooling was the dominant factor in terms of cooling a larger portion of the endwall up to mid-passage, cooling through mateface gap had a pronounced effect on the suction side of the platform near trailing edge. Considering mateface leakage only, there was barely any cooling coverage on the baseline endwall due to higher endwall static pressure as well as stronger cross passage secondary flow compared to aero-optimized endwall. In the case of combined purge and mateface leakage, a major improvement in NHFR was observed using

the contoured endwall. Significant presence of cooling is observed on the suction side of the platform almost along the entire length of the mateface gap using the aero-optimized endwall.

The preliminary design of endwall contours are often based on solid endwalls without any slots, gaps and holes. But in realistic engine environment, leakage flows arising due to turbine assembly features are absolutely necessary to seal the interfaces in order to prevent hot gas ingestion into the core. Thus, it is also very important for designers to validate their modeling tools and advanced designs with extensive experiments in presence of realistic cooling and leakage flow features. This paper provides extensive experimental investigation on these important design features that are essential for overall improvement of aero thermal performance of gas turbines.

ACKNOWLEDGEMENTS

The authors would like to acknowledge the funding support from the US Department of Energy through Siemens Energy, Inc. This material is based upon work supported by the US Department of Energy under Award Number DE-FC26-05NT42644.

NOMENCLATURE

AO	Aero-Optimized
C_{ax}	Axial chord length (m)
h, HTC	Heat transfer coefficient $\left(\frac{W}{m^2K}\right)$
h_f	Heat transfer coefficient – Film Cooled case $\left(\frac{W}{m^2K}\right)$
h_{ref}	Heat transfer coefficient – Reference case $\left(\frac{W}{m^2K}\right)$
IR	Infrared
k	Thermal conductivity $\left(\frac{W}{m\,K}\right)$
M	Mach number
M_{iso}	Isentropic Mach number $M_{iso} = \sqrt{\left(\left(\frac{p_{0in}}{p_{s\,exit}}\right)^{\frac{\gamma-1}{\gamma}} - 1\right)\frac{2}{\gamma-1}}$
MFR	Mass flow ratio (coolant mass flow rate per passage/ mainstream mass flow rate per passage)
NHFR	Net Heat Flux Reduction
p_{0in}	Pitchwise average stagnation pressure at inlet midspan (Pa)

$p_{s\ exit}$	Pitchwise average static pressure on angled end wall 0.5 C_{ax} downstream of the trailing edge (Pa)
q''	Heat flux $\left(\frac{W}{m^2}\right)$
t	Time (s)
T	Temperature (K or ^oC)
T_{aw}	Adiabatic wall temperature (K or ^oC)
T_f	Film temperature (K or ^oC)
T_r	Recovery temperature (K or ^oC)
T_{ref}	Reference temperature (K or ^oC)
T_w	Wall temperature (K or ^oC)
T_i	Initial temperature (K or ^oC)
T_c	Coolant temperature (K or ^oC)
x, y, z	Cartesian Co-ordinates (m)
w	Uncertainty in measurements

Greek Letters

α	Thermal diffusivity $\left(\frac{m^2}{s}\right)$
φ	Overall Cooling effectiveness
γ	Ratio of specific heats
η, ETA	Film/Adiabatic Cooling effectiveness

Suffix

min	Minimum value
max	Maximum value

REFERENCES

[1] Robert Alan Brittingham, Edward Durell Benjamin, Charles Perry II Jacob, Craig Allen Bielek, "Airfoil shape for a turbine bucket", US Patent no. 6779980.

[2] Siemens Energy Inc. SGT5-4000F.

[3] Roy, A., Blot, D., Ekkad, S.V., Ng, W.F., Lohaus, A.S., and Crawford, M.E., 2013, "Effect of Endwall Contouring in presence of Upstream Leakage Flow in a Transonic Turbine Blade Passage: Heat Transfer Measurements", 49th AIAA/ASME/SAE/ASEE Joint Propulsion Conference & Exhibits, July 15-17, 2013, San Jose, CA.

[4] Yamao, H., Aoki, K., Takeishi, K., and Takeda, K., 1987, "An Experimental Study for Endwall Cooling Design of Turbine Vanes," IGTC-1987, Tokyo, Japan.

[5] Aunapu, N. V., Volino, R. J., Flack, K. A., and Stoddard, R. M., 2000, "Secondary Flow Measurements in a Turbine Passage with Endwall Flow Modification," ASME J. Turbomach., 122, pp. 651–658.

[6] Piggush, J. D., and Simon, T. W., 2005, "Flow Measurements in a First-Stage Nozzle Cascade Having Endwall Contouring, Leakage and Assembly Features," ASME Paper No. GT2005-68340.

[7] Piggush, J. D., and Simon, T. W., 2005, "Heat Transfer Measurements in a First-Stage Nozzle Cascade Having Endwall Contouring, Leakage and Assembly Features," ASME Paper No. HT2005-72573.

[8] Piggush, J. D., and Simon, T. W., 2006, "Heat Transfer Measurements in a First-Stage Nozzle Cascade Having Endwall Contouring: Misalignment and Leakage Studies", J. Turbomachinery, **129(4)**, pp. 782-790.

[9] Piggush, J. D., and Simon, T. W., 2006, "Adiabatic Effectiveness Measurements in a First-Stage Nozzle Cascade Having Endwall Contouring, Leakage, and Assembly Features," ASME Paper No. GT2006-90576.

[10] Ranson, W.W., Thole, K.A., and Cunha, F.J., 2005, "Adiabatic Effectiveness Measurements and Predictions of Leakage Flows Along a Blade Endwall", J. Turbomachinery, **127**, pp. 609-618.

[11] Reid, K., Denton, J., Pullan, G., Curtis, E., and Longley, J., 2007, "The Interaction of Turbine Inter-Platform Leakage Flow With the Mainstream Flow," ASME J. Turbomach., 129, pp. 303–310.

[12] Reid, K., Denton, J., Pullan, G., Curtis, E., and Longley, J., 2006, "Reducing the Performance Penalty Due to Turbine Inter-Platform Gaps," ASME Paper No. GT2006-90839.

[13] Cardwell, N.D., Sundaram, N., and Thole, K.A., 2006, "Effect of Midpassage Gap, Endwall Misalignment, and Roughness on Endwall Film-Cooling", J. Turbomachinery, **128**, pp. 62-70.

[14] Cardwell, N.D., Sundaram, N., and Thole, K.A., 2007, "The Effects of Varying the Combustor-Turbine Gap", J. Turbomachinery, 129, pp. 756-640.

[15] Hada, S., and Thole, K. A., 2006, "Computational Study of a Midpassage Gap and Upstream Slot on Vane Endwall Film-Cooling," ASME Paper No. GT2006-91067.

[16] Lynch, S.P., Thole, K.A.., 2001, "The Effect of the Combustor-Turbine Slot and Midpassage Gap on Vane Endwall Heat Transfer", J. Turbomachinery, 133, pp. 041002-1-9.

[17] Panchal, K.V., Abraham, S., Ekkad, S.V., Ng, W.F., Lohaus, A.S., and Crawford, M.E., 2012, "Effect of endwall contouring on a transonic turbine blade passage: Part 2 – Heat transfer performance", ASME Paper No. GT2012-68405.

[18] Roy, A., Blot, D., Ekkad, S.V., Ng, W.F., Lohaus, A.S., and Crawford, M.E., 2013. "Effect of upstream purge slot on a transonic turbine blade passage: Part 2 – heat transfer performance", ASME Paper No. GT2013-94581.

[19] Panchal, K.V., Abraham, S., Ekkad, S.V., Ng, W.F., Brown, B., and Malandra, A., 2011, "Investigation of effect of endwall contouring methods on a transonic turbine blade passage", ASME Paper No.GT2011-45192.

[20] Smith, D.E., Bubb, J.V., Popp, O., Grabowski, H.C., Diller, T.E. Schetz, J.A. and Ng. W.F., 2000, "Investigation of Heat Transfer in a Film Cooled Transonic Turbine Cascade, Part I: Steady Heat Transfer," ASME Paper No. 2000-GT-202.

[21] Mick W.J., Mayle R.E.,1988, "Stagnation film cooling and heat transfer, including its effect within the hole pattern", J. Turbomachinery,110,pp.61-70.

Overall Conclusions

Heat transfer measurements were performed on a transonic turbine passage and effects of endwall contouring were investigated in presence of three major endwall cooling features – upstream slot purge flow (turbine stator-rotor interface), mateface gap leakage (gap between adjacent airfoil-endwall assembly) and discrete hole film cooling for different coolant flow rate combinations. All experiments have been performed at design incidence angle and design exit Mach number 0.88 using transient infrared thermography measurement technique. Local distribution of three key heat transfer parameters has been investigated to account for comparative analysis – heat transfer coefficient, adiabatic film cooling effectiveness and net heat flux reduction. The major conclusions that can be summarized considering the overall heat transfer performance of the contoured endwall compared to a baseline planar endwall are as follows:

- Presence of the upstream slot has a first order effect on endwall heat transfer coefficient for both designs. Contouring aids in further reduction of endwall heat load due to weakening of secondary flow effects.
- At higher purge flow rates through the upstream slot, coolant coverage was observed marginally inside the passage, however, suction side throat region was better cooled in case if contoured endwall and almost extended up to the trailing edge.
- High heat transfer levels were observed near discrete hole exit and the intensity increased with higher coolant flow rates for baseline endwall. This phenomenon was highly diminished using the contoured endwall.
- In case of discrete hole film cooling, pressure side leg of the horse-shoe vortex and cross passage pressure differential influenced coolant coverage pattern significantly. Majority of the coolant streaks from three rows of coolant holes were directed towards suction side of the airfoil for baseline endwall, whereas, the streaks were more aligned towards mainstream flow passage direction for contoured endwall resulting in better film coverage. This was more prominent considering the improvement in net heat flux reduction near the mid-passage region for the contoured endwall.
- Heat transfer performance of the contoured endwall outperformed the baseline endwall considering the most realistic engine cooling condition – combination of upstream purge flow and mateface gap leakage. Major improvement in heat load reduction was achieved specially near suction side of the platform. Endwall pressure distribution was attributed to non-uniform cooling along the mateface gap and coolant ejection was more favorable near the trailing edge due to higher momentum of the coolant able to overcome endwall surface pressure.

Contribution of Research Work

The major contributions of the presented study towards development and further advancement of gas turbine film cooling science and technology are highlighted below:

Heat transfer data reduction method development - A novel heat transfer data reduction procedure, "Linear Regression Method", has been developed for improved quantitative measurements applicable under realistic gas turbine operating conditions. The Linear Regression method has been shown to be beneficial under engine representative flow conditions. The effects of compressible flow physics, transonic aero-thermodynamic conditions have been successfully incorporated to obtain more accurate heat transfer parameters. Simultaneous calculation of key heat transfer parameters in presence of film cooling conditions – heat transfer coefficient and adiabatic film cooling effectiveness, is also a salient feature of the Linear Regression Method. Majority of the papers in existing literature present results on either heat transfer coefficient or film cooling effectiveness. However, for overall understanding of heat transfer performance in presence of external film cooling, knowledge of both parameters are necessary to contribute towards quantifying the benefits of design improvement. The proposed method was based on a technique earlier developed by Oliver Popp at Virginia Tech [1] for application in vane film cooling using where the recovery temperature profile was obtained from uncooled heat transfer experiments and superimposed on film cooled vanes to solve for heat transfer coefficient and film effectiveness simultaneously. The assumption of identical recovery temperature profiles for uncooled and film cooled case may be reasonable for vane or blade cooling with relatively lower coolant flow rates. For the present application in endwall cooling, major section of the near endwall flow characteristics change from uncooled to film cooled case, thereby assuming local flow parameters to remain the same would be inappropriate. The Linear Regression method developed thus incorporates the correct flow physics by comparing similar flow conditions between two film cooled runs varying only coolant temperature to calculate heat transfer coefficient and film effectiveness simultaneously. The reliability of this method was also validated by comparing data with existing Nusselt number correlations upstream of the passage.

Addition of benchmark data under engine representative conditions – The other unique contribution of this research work is to provide experimental data to the existing pool of literature on gas turbine cooling for benchmarking, which would also serve as an important validation database for highly advanced computational fluid dynamics (CFD) prediction tools. Studies on heat transfer performance with realistic cooling features under modern gas turbine engine operating conditions are rare. Engine representative condition warrants matching not only Reynolds number, simulating the effect of realistic Mach number is essential as well. As mentioned in the literature review in earlier chapters, that no such experimental study has been reported that investigates effects of endwall contouring with any cooling features under transonic operating conditions. The only study that exists incorporating upstream purge flow and discrete film cooling in a low speed first stage vane cascade was presented by Thrift et al. [2]. However, as shown in Figure 46, comparison with the present study on the first stage blade reveals that - 1) the endwall heat transfer levels (Nusselt number) are significantly under predicted and 2) film cooling coverage is severely over predicted under similar coolant to mainstream mass flow ratios and matching inlet Reynolds number.

The primary reason for this discrepancy is the effect of mainstream pressure which is negligible for low speed studies. Hence the coolant jet can easily overcome mainstream static pressure barrier. This certainly depicts the necessity of performing experiments using appropriate non-dimensional flow parameters for data accuracy.

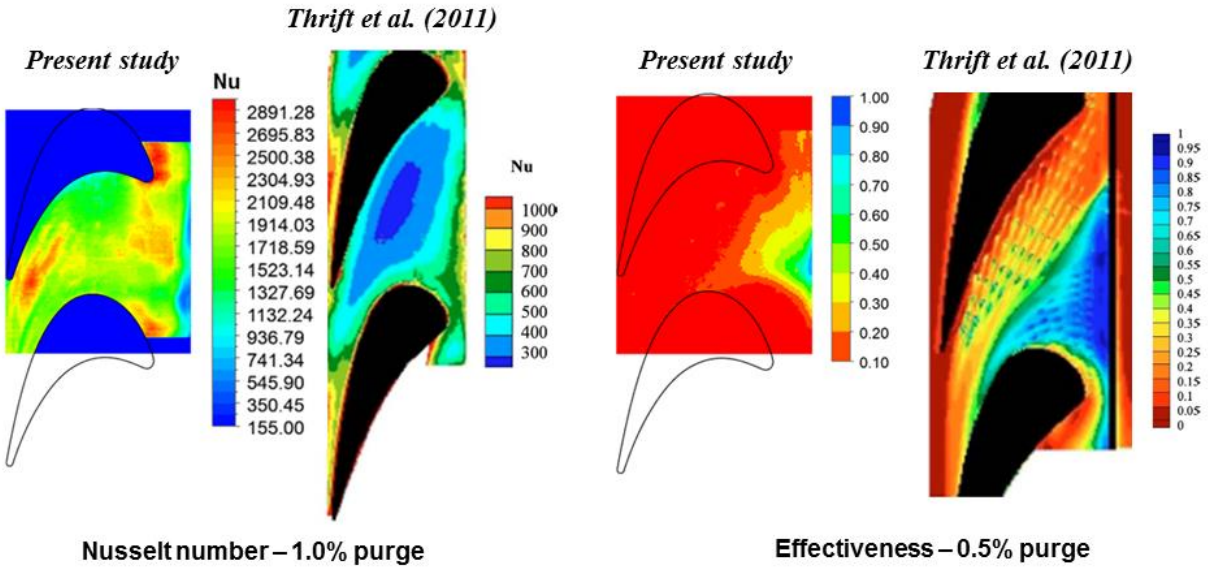

Figure 46: Comparison of endwall heat transfer performance with published low speed cascade study

Therefore, the present study provides a significant insight that compressible flow effects have a major influence on aero-thermal performance of gas turbine engines under realistic conditions. Primarily the research project was aimed to provide experimental data to sponsor Siemens Energy Inc., for CFD code validation, thus improving their CFD prediction capabilities.

References

[1] Popp, O., Smith, D.E., Bubb, J.V., Grabowski, H.C., Diller, T.E. Schetz, J.A. and Ng. W.F., 2000, "Investigation of Heat Transfer in a Film Cooled Transonic Turbine Cascade, Part II: Unsteady Heat Transfer," *ASME* 2000-GT-203.

[2] Thrift, A.A., Thole, K. A., Hada, S., "Effects of an Axisymmetric Contoured Endwall on a Nozzle guide Vane: Adiabatic Effectiveness Measurements", *ASME Journal of Turbomachinery*, 2011, Vol. 133, pp. 041007-1-041007-10.

Appendix A - Heat Transfer Characteristics of New Optimized Endwall Design

Background

Three different passage designs were experimentally investigated during Siemens Project 2012-13 for aerodynamic and heat transfer performance. The endwall geometries (baseline, AO endwall and OPT1 endwall) have identical blade profiles, span and pitch. The basic design features of baseline and AO endwall contours have already been mentioned earlier. Another new endwall contour profile (OPT1) designed with the intent to minimize aerodynamic losses in presence of an upstream purge slot (simulating a geometrical feature between stator-rotor interface) was also investigated. All endwall contour designs were provided by Siemens Energy Inc. Similar to Baseline and AO endwall as mentioned in Chapter 3, the following heat transfer experiments were performed on OPT1 endwall:

- Heat transfer experiments were carried out using transient infrared thermography technique. Several cases were investigated to isolate the individual effect of addition of mateface geometry as well as addition of coolant through the mateface gap. Combined upstream and mateface leakage conditions were also simulated which represents realistic engine operating conditions. The temperature data was converted to evaluate key heat transfer parameters - Heat Transfer Coefficient and Adiabatic Cooling Effectiveness using a comprehensive analysis and detailed comparisons were reported.

Design

The upstream leakage slot design and mateface leakage gap design as mentioned earlier in Chapter 1 and Chapter 3 respectively were kept identical for OPT1 endwall as well. Figure A-1 shows the full cascade set up with blown up center part with upstream purge slot and mateface gap for OPT1 endwall.

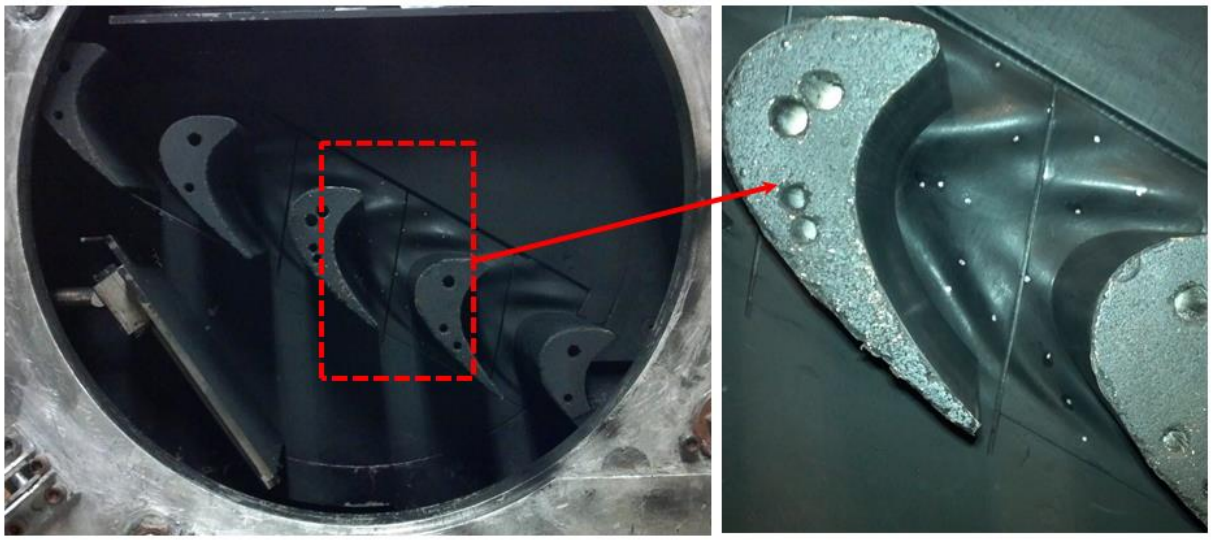

Figure A 1: OPT1 endwall cascade (left) and passage design (right)

Heat Transfer Results

The test cases that were performed on OPT1 endwall geometry have been summarized in Table 4 (Cases 3, 4 and 5) of Chapter 3 of this dissertation.

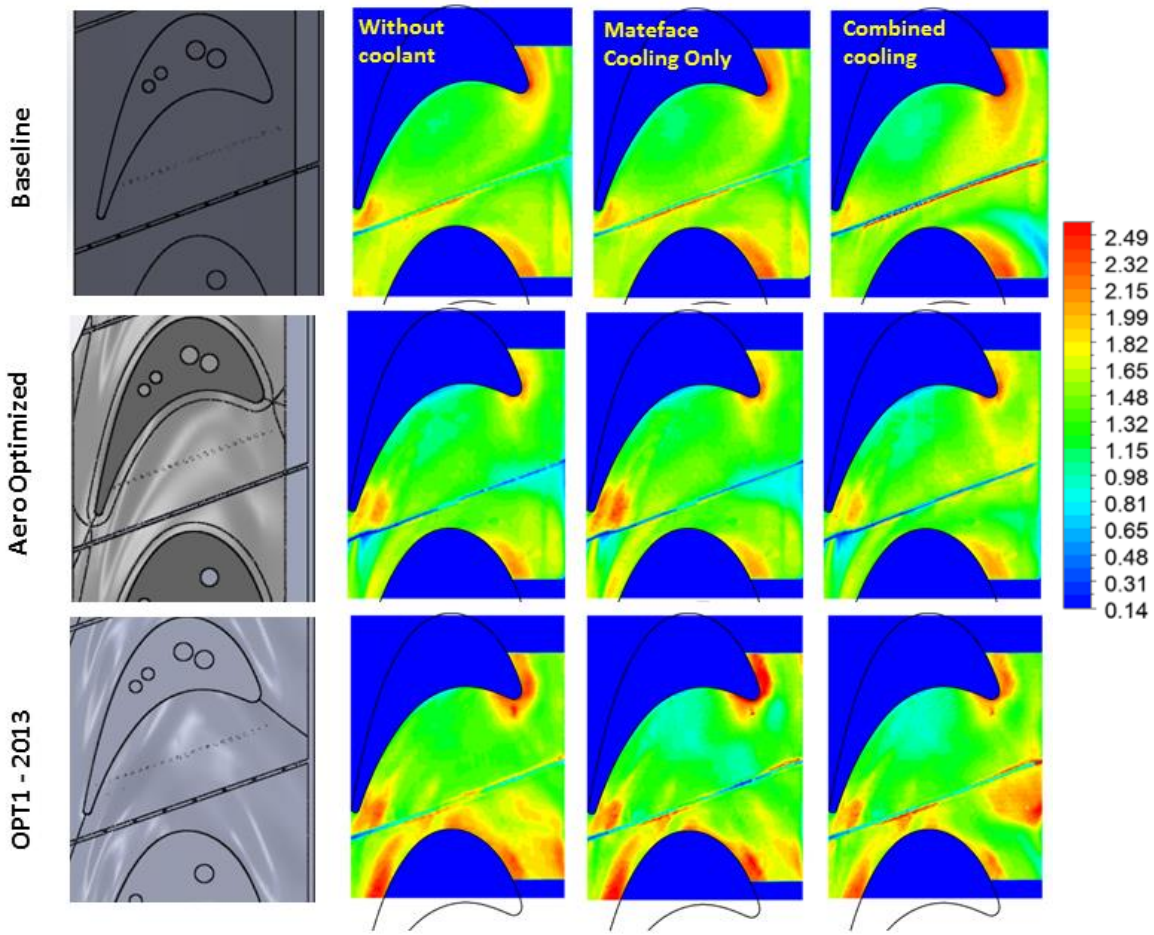

Figure A 2: Effect of contouring on endwall heat transfer coefficient in presence of upstream slot and mateface gap

Table A 1: Area averaged Heat Transfer Coefficient Comparison

	No coolant	Mateface leakage only	Combined purge and leakage
Baseline	-	+1%	+1%
AO	-10%	-7%	-6%
OPT1	+6%	-1%	-

Figure A-2 shows the endwall heat transfer coefficient distribution for only mateface leakage and combined purge and mateface leakage for baseline, AO and OPT1 endwall geometries. The without coolant case has been

added to show the effect of coolant injection. Table A-1 summarizes the comparative performance of area averaged HTC values considering Baseline (with purge slot and mateface gap) geometry without any coolant blowing. Reduction in area averaged HTC occurs for all cases using the AO endwall, with the no coolant case performing the best (almost 10% reduction). On the contrary, the OPT1 endwall showed marginal or almost no improvement in overall heat transfer coefficient for mateface leakage only and combined leakage flow cases respectively. This is due to the increase in localized HTC especially near the suction side of the airfoil (both cases) and just downstream of the purge slot adjacent to the mateface gap.

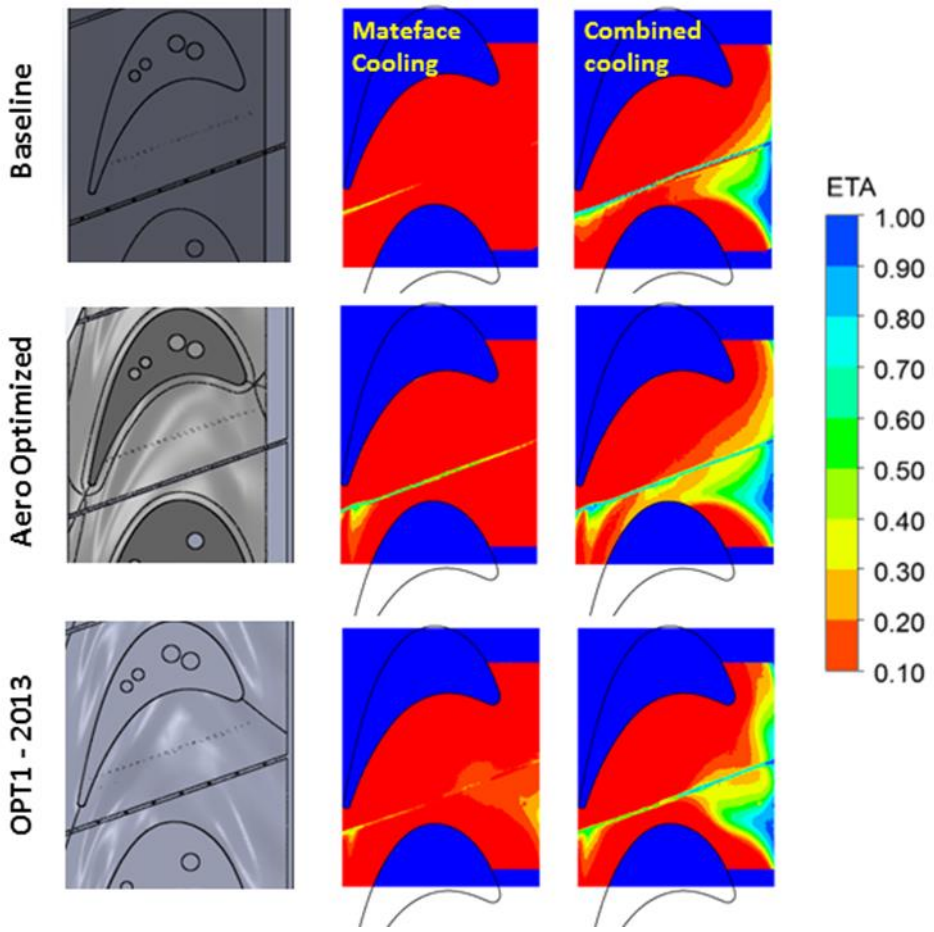

Figure A 3: Effect of contouring on endwall adiabatic cooling effectiveness in presence of upstream slot and mateface gap

Investigation of the local heat transfer coefficient distribution reveals that addition of coolant in case of combined upstream slot and mateface gap leakage flow, increases heat transfer levels just downstream of the purge slot. This enhancement occurs around the mateface gap purge slot intersection and highly prominent for OPT1 endwall. This is due to coolant injection into the incoming boundary layer creates additional turbulent mixing, heat dissipation and increased near wall velocity. Another point that can be noted is that the high HTC zone shifts from pressure side to the suction side of the mateface platform moving from AO endwall to OPT1 endwall. The profile of

the endwall near the upstream slot may attribute to the reason behind this shift. The other prominent differences that can be observed comparing the HTC contours in Fig. A-2 are – 1) the pressure side leg of the horse-shoe vortex grows in strength with addition of coolant from the purge slot (combined leakage case) for baseline endwall. This can be attributed to strengthening the boundary layer approaching the leading edge of the airfoil with addition of energy from the coolant and, 2) reduction of endwall heat transfer coefficient near upstream of the airfoil to throat region on the suction side of the platform. A concrete explanation behind this phenomenon could not be established with the present set of experimental data and warrants more detailed investigation. Controlling the formation and trajectory of complex vortices along with secondary flow is the key to minimize hot gas entrainment towards the platform and hence serves as the basis of design for endwall contour profiles. It can be conjectured that, the additional increase in endwall heat transfer levels, occur due to increase in strength of suction side leg of the horseshoe vortex, which is also evident from oil flow visualization experiment performed. Heat transfer reduction due to effect of endwall contouring is evident though on the pressure side of the platform using both AO and OPT1 endwall. The detailed explanation behind the general heat transfer reduction using the AO geometry has been provided in Project Report FY2010-11 and FY2011-12 and hence is not repeated here.

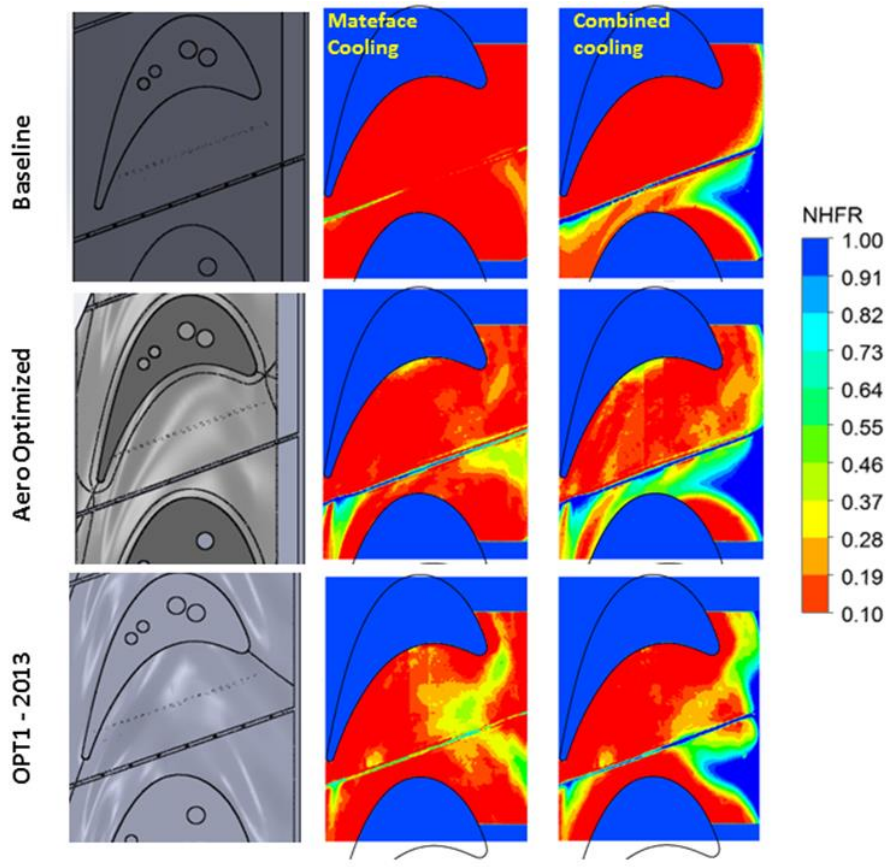

Figure A 4: Effect of endwall contouring on net heat flux reduction (NHFR)

Figure A-3 shows the adiabatic cooling effectiveness levels for all endwall geometries considering Cases 4 and 5 as mentioned in Table 1 of Chapter 3. Once again, the AO endwall outperforms the other two endwall designs in terms of coolant coverage on the endwall in both mainstream flow and cross passage directions. The advantage of using the OPT1 endwall over the AO design can only be realized near the leading edge, where the coolant spread is more uniform and therefore provides better cooling. The coolant is almost blown away and hardly any coolant coverage downstream of the passage near trailing can be seen with mateface leakage only, which is similar to baseline endwall.

Figure A-4 shows the local NHFR distribution for all leakage cases (mateface and combined flow). Significant improvement in NHFR is obtained using the AO endwall geometry, especially the platform region bounded within mateface gap and suction side of the airfoil for the combined leakage flow case. Similar to the coolant spread profile, OPT1 endwall provides better NHFR near the leading edge, however, appreciable NHFR is only observed up to mid-passage suction side. The major contributor to the NHFR along the suction side of the platform is the coolant effectiveness distribution. There is some reduction in heat flux near the pressure side of the platform as well which occurs due to altering the passage vortex flow path in case of the contoured endwalls compared to the baseline geometry. In case of the mateface only leakage for OPT endwall there is minimal improvement downstream of the passage near the trailing edge region. However, some improvement in NFHR levels is observed up to mid-passage on the pressure side due to effective control of the pressure side leg of the horseshoe vortex, hence dominated by lower HTC. For AO endwall, apart from expected improvement in NHFR near the trailing edge due to coolant spread, heat load reduction can also be observed near the region just downstream of the slot within the stagnation zone.

Conclusions

AO endwall benefits in reduction of overall area averaged heat transfer coefficient for with and without leakage flow cases due to most effective secondary flow control. OPT1 endwall however, shows enhanced endwall heat transfer levels localized near the suction side of the platform, due to increase in strength of suction side leg of the horse-shoe vortex. Local enhancement of heat transfer can be observed just downstream of the purge slot due to turbulent mixing of the coolant jet with the mainstream, which is more prominent in case of OPT1 endwall. Although, purge cooling is the dominant factor in terms of cooling a larger portion of the endwall up to mid-passage, cooling through mateface gap had a pronounced effect on the suction side of the platform near trailing edge especially in case of AO endwall. Near trailing edge region, OPT1 endwall performance w.r.t. coolant coverage is comparable to baseline case. Considering mateface leakage only, there was barely any cooling effectiveness on the baseline and OPT1 endwall most likely due to higher endwall static pressure as well as stronger cross passage secondary flow compared to aero-optimized endwall. In case of combined purge and mateface leakage, a major improvement in NHFR was observed using the AO endwall. Improvement in NHFR using the OPT1 endwall could only be realized near the leading edge of the airfoils along pressure side of the platform. Significant NHFR is obtained on the suction side of the platform almost along the entire length of the mateface gap using the AO endwall.

Appendix B - Mateface Ingestion Analysis

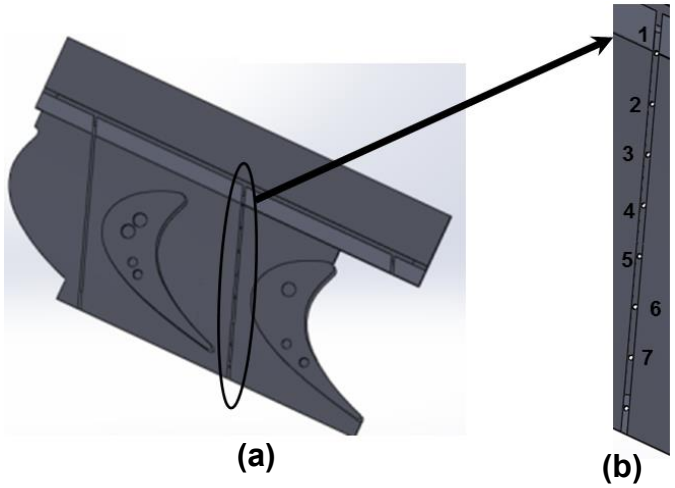

Figure B 1: (a) Baseline geometry center passage with mateface gap, (b) thermocouple locations

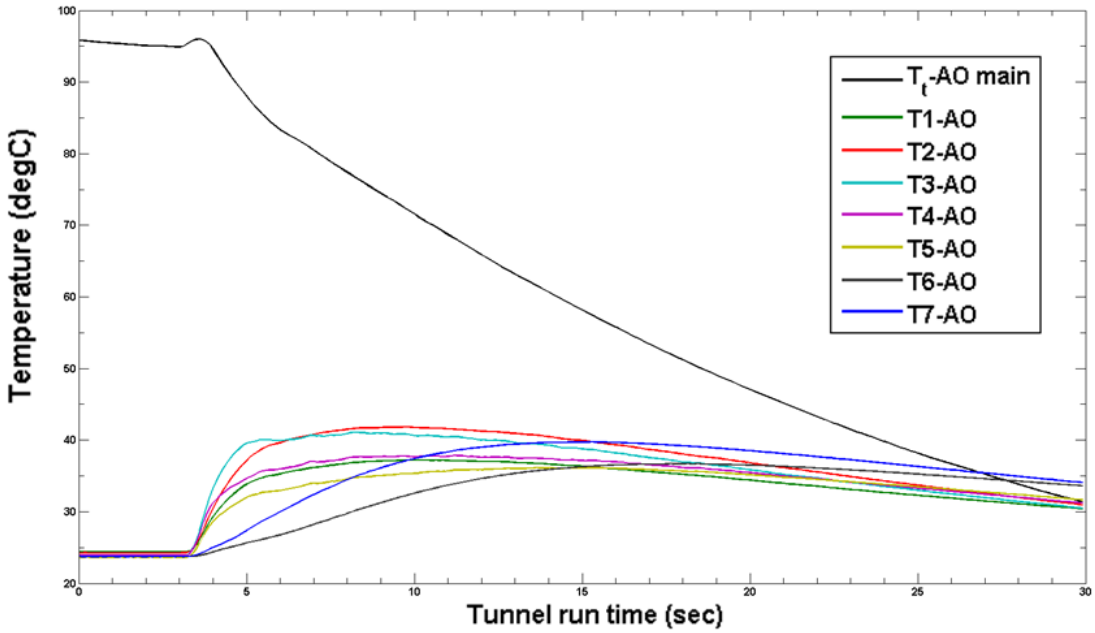

Figure B 2: AO endwall mateface temperature transience

Figure B-1 (a) and (b) show the center part of the baseline endwall cascade test section with the mateface gap and thermocouple positions along the length of the mateface gap respectively. These thermocouple beads protrude above the base of the mateface gap up to the centerline of the holes ejecting the coolant inside the mateface gap. Thermocouples 1 through 7 recorded transient temperature variation inside the gap at each individual location. One such temporal variation for AO endwall without any coolant injection is shown in Fig. B-2.

In order to carry out the extent of mainstream ingestion and mixing with coolant inside the mateface gap the following normalization procedure is adopted to be consistent for all endwall geometries along with all leakage cases. This method also nullifies the effect of variation of initial temperature from day to day. The normalized mateface temperature (θ) is expressed as,

$$\theta = \frac{T_m - T_{tc}}{T_m - T_c} \tag{B-1}$$

Where, T_{tc} represents the mateface thermocouple data (tc = 1 to 7). Therefore, θ values 0 would mean complete mainstream ingestion and 1 refers to no mixing, hence presence of coolant only. Each temperature in Eq. (B-1) is time averaged for 1s within the data reduction period.

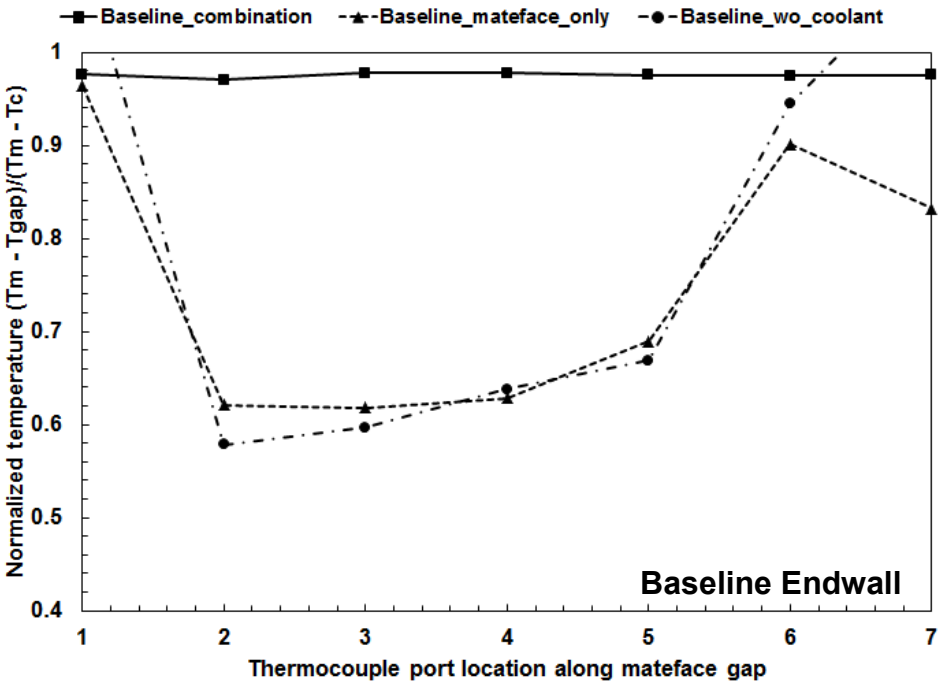

(a)

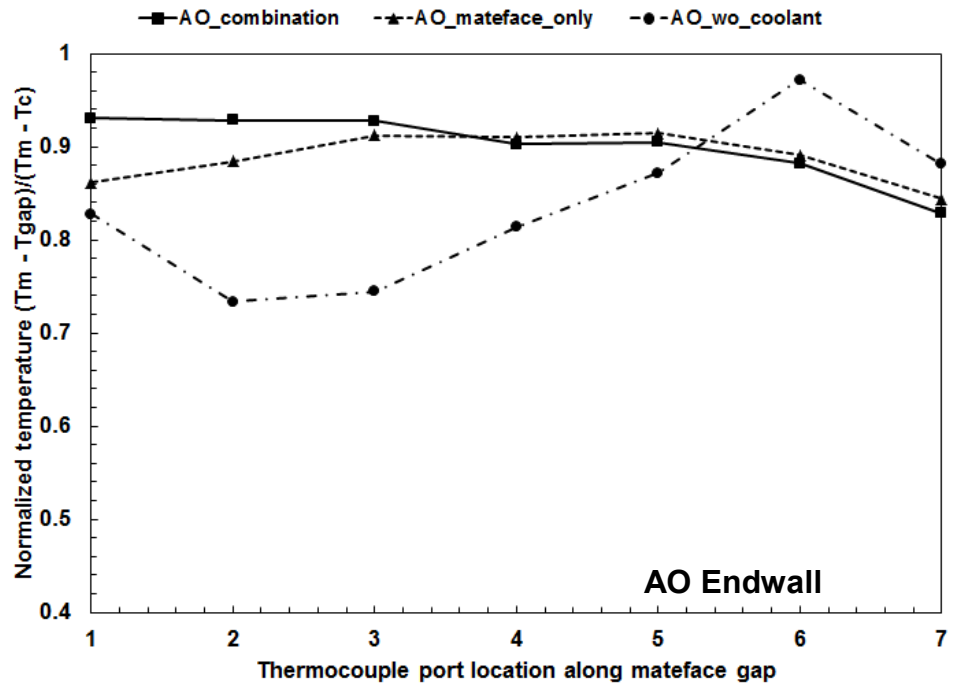

(b)

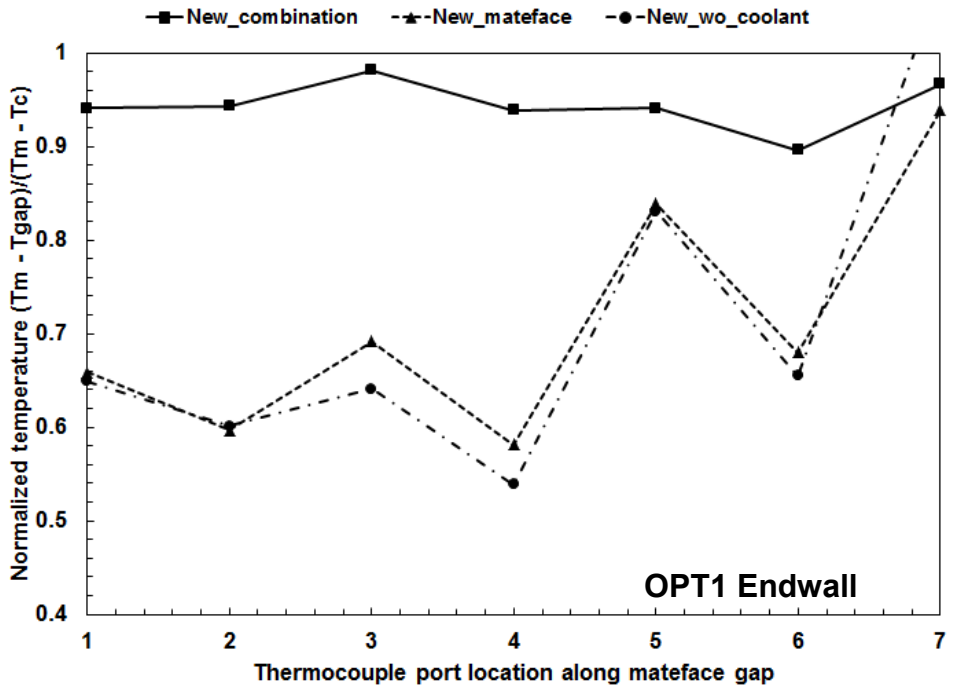

(c)

Figure B 3: Mateface ingestion profile comparing all cases

Figure B-3(a)-(c) represent non-dimensional temperature profile along mateface gap length for baseline, AO and OPT1 endwall respectively. Without coolant cases are included to show primarily the effect of coolant injection through the mateface gap only. A general trend that can be observed for without coolant and mateface only

leakage, present in endwall geometries is that θ decreases starting from the upstream slot region up to a certain distance along the mateface gap and then recovers gradually progressing towards the trailing edge. This can be explained from endwall surface pressure variation along the flow direction as described earlier. The low momentum coolant up to mid-passage region is not able to overcome the high static pressure of the mainstream flow, resulting in major mainstream ingestion. However, as the surface pressure decreases, the coolant gathers more energy to eject near the trailing edge of the passage increasing non-dimensional mateface temperature. For combined leakage case, baseline endwall exhibits best performance throughout the mateface gap with values more than 0.95.

The comparison between respective endwall geometries for mateface leakage and combined leakage cases are clearly evident from Fig. B-4. The ingestion though OPT1 endwall mateface gap lies between AO and Baseline endwall especially for combined leakage condition.

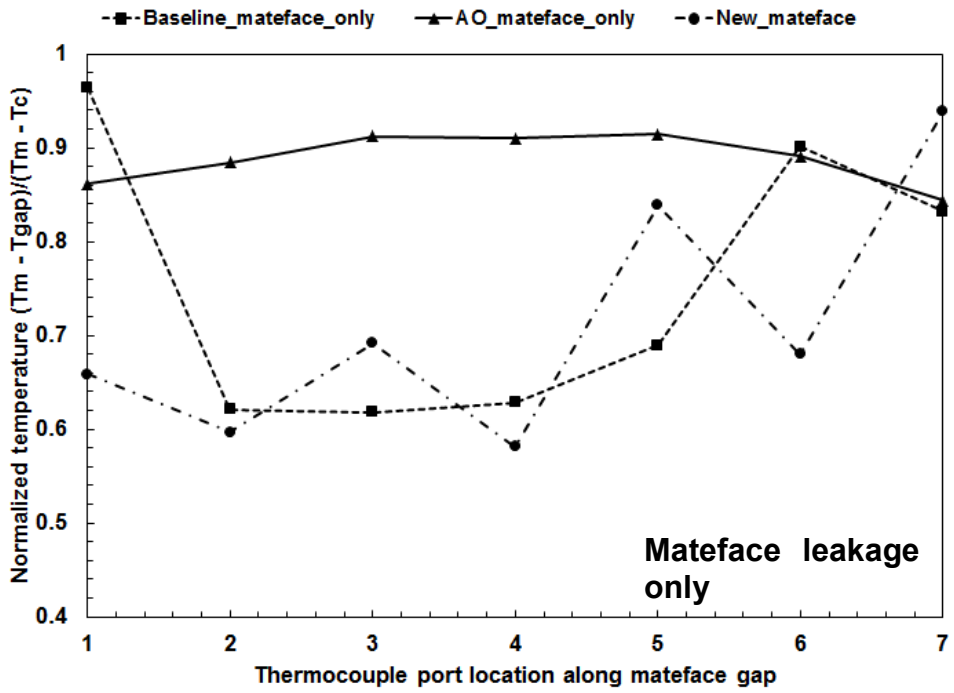

(a)

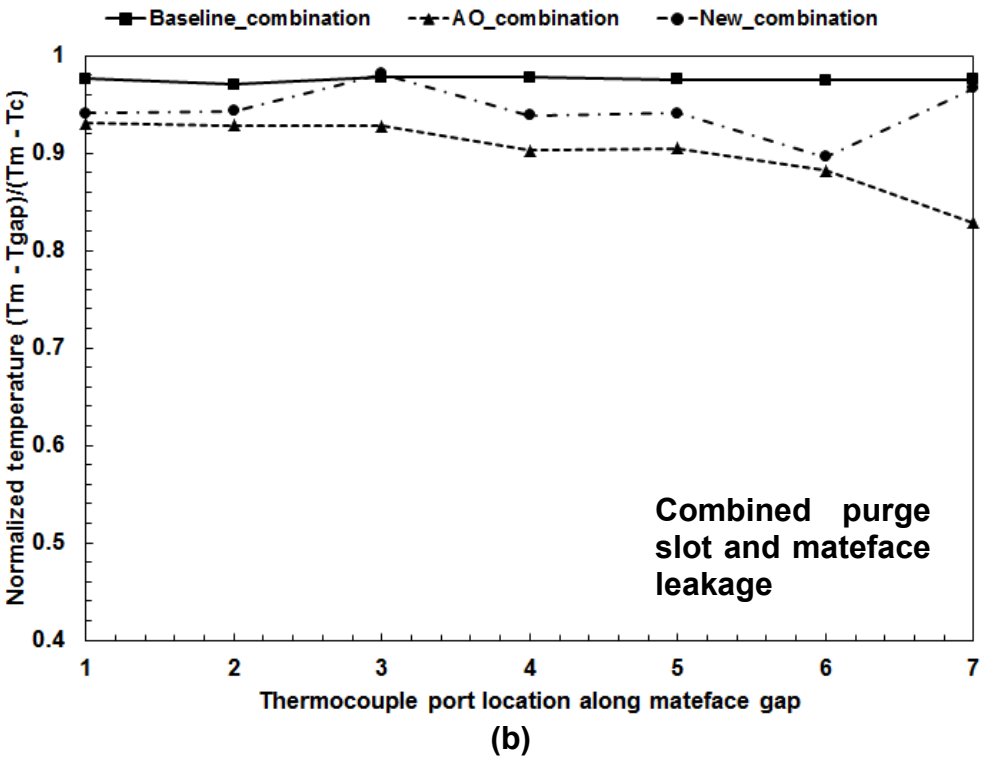

(b)

Figure B 4: Effect of contouring on non-dimensional mateface temperature

Appendix C

A Novel Data Processing Technique for Convective Heat Transfer Experiments in a Transient Transonic Heated Wind Tunnel

Song Xue, Arnab Roy, Srinath V. Ekkad, Wing F. Ng

Mechanical Engineering Department
Virginia Polytechnic Institute and State University
Blacksburg, VA 24061

Manuscript submitted to Measurement Science and Technology journal

ABSTRACT

The study presented in this article provides detailed description about a newly developed data processing technique to determine two key convective heat transfer parameters simultaneously in hot gas path of a modern high pressure turbine - heat transfer coefficient (HTC) and adiabatic film cooling effectiveness (Eta). The proposed technique, Linear Regression Method, is compared with a widely used data reduction procedure - Curve Fitting Method. Both techniques are based on the 1-D semi-infinite transient conduction theory and applicable towards uncooled as well as film-cooled heat transfer. The major difference between the Linear Regression Method, and the Curve Fitting Method is highlighted as, the latter considers the initial unsteady flow development within the data reduction period by assuming a step jump in mainstream pressure and temperature, which results in significant under prediction of HTC due to the gradual ramping of the flow Mach/Reynolds number and varying temperature in a transient, cascade wind tunnel facility. The linear regression method is advantageous due to the elimination of these added assumptions. For film cooling experiments, both techniques address the three-temperature problem by a two-test strategy to determine HTC and Eta. The recovery temperature is equal to the mainstream total temperature in case of the Curve Fitting Method. However, while applying Linear Regression method incorporating compressibility effects, the recovery temperature is treated as an unknown and for a film cooled surface, and is calculated through an iterative procedure. The detailed discussion on theory and development of the methods is followed by validation with analytical calculation and application of both techniques reducing the same set of experimental data. Results indicate that the Linear Regression Method stands out in both film cooling and uncooled experiments with a higher accuracy and reliability.

INTRODUCTION

In order to assess the thermal protection schemes during the design of turbine hot gas path components, it is important to accurately determine the convective heat transfer coefficient which is defined by Eq. (1).

$$h = \frac{q}{(T_\infty - T_w)} \tag{1}$$

Where, h is the HTC; q is the surface heat flux; T_∞ is the mainstream gas temperature, which should be replaced by

the local recover temperature T_r when compressibility effect is considered under high speed conditions; T_w is the surface temperature.

Theoretically, the easiest way to calculate the HTC is to measure the surface temperature under steady state conditions, with a known surface heat flux. In some heat transfer experiments the constant surface heat flux is implemented by the instrumentation of thin foil heater on the test surface. However, the application of this technique is limited due to – 1) difficulties in instrumentation for many sophisticated geometries, 2) poor spatial resolution and 3) unable to extract parameters in film-cooled cases. Therefore, transient techniques, such as liquid crystal and infrared thermography had been significantly developed over in the last two decades.

Transient heat transfer problem in uncooled experiments

In case of a transient convective heat transfer experiment, usually, the first step of the entire procedure is to measure the temperature of the test section surface. The surface temperature can be measured using thermal sensors (Nasir et al. [1] and Xue et al. [2]); or though associated color change in thermo-chromic liquid crystals (Ekkad et al.[3], Kwak et al.[4]); or directly using infrared cameras (Christophel et al.[5] and Ekkad et al. [6]).

The surface temperature once recoded, is applied either as a direct or indirect boundary condition to solve the transient thermal conduction inside the material. In most of the studies, to obtain a more accurate measure of the convective heat flux, low thermal conductivity materials are used, such as ABS or epoxy. If the surface curvature variation is small enough and thermal penetration depth is neglected, the heat flux can be assumed to occur in the direction perpendicular to the surface. Therefore, a 1-D thermal transient conduction model as shown in Eq. (2) is applicable for a short duration (usually less than 10 seconds). It will be discussed later, the major difference between the data processing techniques lies in the application of the boundary conditions to this 1-D model.

$$\frac{\partial T}{\partial t} = \alpha \frac{\partial^2 T}{\partial x^2} \tag{2}$$

Transient heat transfer problem in film cooling experiment

Since 1970's, film cooling technology in gas turbines has improved significantly. In film cooling, coolant air tapped from compressor stages injected through small holes on the airfoil surface as well as through the interfaces between stationary and rotating parts of the turbine to prevent ingestion into the turbine core, generates a thin insulating layer along the surface to protect the component material from the hot gas flow. On a film cooled surface, the definition of HTC in equation (1) becomes,

$$h = \frac{q}{(T_{aw} - T_w)} \tag{3}$$

Where, T_{aw} is the adiabatic wall temperature, which is equal to the near wall film temperature, and is a mixed intermediate temperature between the mainstream and the coolant flow. Besides the HTC, another important parameter to be determined in a film cooling experiment is the adiabatic cooling effectiveness, which is defined as:

$$\eta = \frac{T_\infty - T_{aw}}{T_\infty - T_c} \tag{4}$$

Where T_c is the coolant temperature. Again, for compressible flow, the mainstream temperature T_∞ , should be replaced by the recovery temperature T_r. The film cooling phenomenon is usually referred as "Three Temperature Problem", due to three temperature variables, the flow recovery temperature (T_r), the surface temperature (T_w), and the coolant temperature (T_c), involved in the convective domain.

The coolant temperature (T_c) and surface temperature (T_w) can be measured directly; the heat flux (q) can be recorded or calculated, based on the temperature data, however, the adiabatic wall temperature (T_{aw}) and the local recovery temperature T_r are unknowns. The 1-D transient conduction model (Eq. 2) is still applicable to describe the heat conduction inside the material, except around the near injection hole region, where the effect due to 2-D or 3-D heat conduction may be considerable.

Literature summary

Studies on development of different data processing techniques for convective heat transfer experiments in gas turbine research area are scarce in open literature. In 1991, Vedula and Metzger [7] developed a two test strategy to calculate HTC and Eta simultaneously, which is still widely used in today's film cooling experiments. Chambers et al. [8] proposed a three-test strategy for data reduction in the impingement cooling tests. In their method the HTC is first calculated in a single test, and the cooling effectiveness is thereafter deduced with the data from additional tests. Kwak [9] summarized the efforts on improving the application of transient liquid crystal technique for non-film cooling convective heat transfer measurement. The data processing method described in his transient liquid crystal technique is similar to the curve fitting method discussed in the present study. To account for varying mainstream reference temperature, Duhamel's superposition theorem is applied, and the flow temperature history profile is discretized with a series of step changes.

The studies reviewed above are based on low speed conditions, whereas in contrast there are limited studies on turbine heat transfer under transonic operating conditions within the compressible flow regime. Giel et al. [10] used transient liquid crystal (TLC) technique along with foil heaters to determine local heat transfer coefficients (HTC) under high speed operating conditions. Nicklas [11] applied a superposition approach to evaluate simultaneous endwall HTC and Eta distribution under transonic operating conditions. IR thermography for surface temperature measurement along with known heat flux conditions from a surface heater were used to analyze the experimental data. As mentioned earlier, the difficulty in instrumentation is usually the major issue that limits the application of surface heater technique on the complicated contour surfaces. Jonsson et al. [12] performed film cooling experiments in presence of upstream slot leakage and discrete hole blowing and calculated simultaneous HTC, Eta, and heat flux on endwall surface using non-linear regression method developed by Vogel et al. [13]. They combined Liquid Crystal and Pressure Sensitive Paint techniques, to calculate key heat transfer parameters simultaneously from three coupled experiments. O'Dowd et al. [14] compared different techniques to obtain HTC on a blade tip

surface and concluded that the infrared thermography technique with heat flux reconstruction using the impulse method, is the most accurate and reliable method to obtain detailed, spatially-resolved heat transfer coefficient and adiabatic wall temperature. It is important to note that the linear regression calculation used in their "A-1 method" is different from the linear regression method that will be discussed in the present study. In their experiment, the wind tunnel facility is able to establish a steady free stream flow, and a powerful electric heater provides a near perfect step rise of the free stream flow temperature. Thus, the linear regression equation in their study is: $q = C_1 T_w + C_2$.

In general, the selection of data reduction techniques in heat transfer experiments is highly dependent on the facility characteristics and resources. Considering heat transfer experiments performed in transient transonic blow down hot wind tunnels, results processed by the Curve Fitting Method may introduce unavoidable errors, which are related to the ramping of the major parameters at the tunnel start. The present study proposes a novel data processing technique to resolve this issue. The present paper also provides a comparative analysis of the proposed data processing technique - Linear Regression Method and the widely used Curve Fitting Method.

CHARACTERISTICS OF THE VIRGINIA TECH TRANSONIC WIND TUNNEL FACILITY

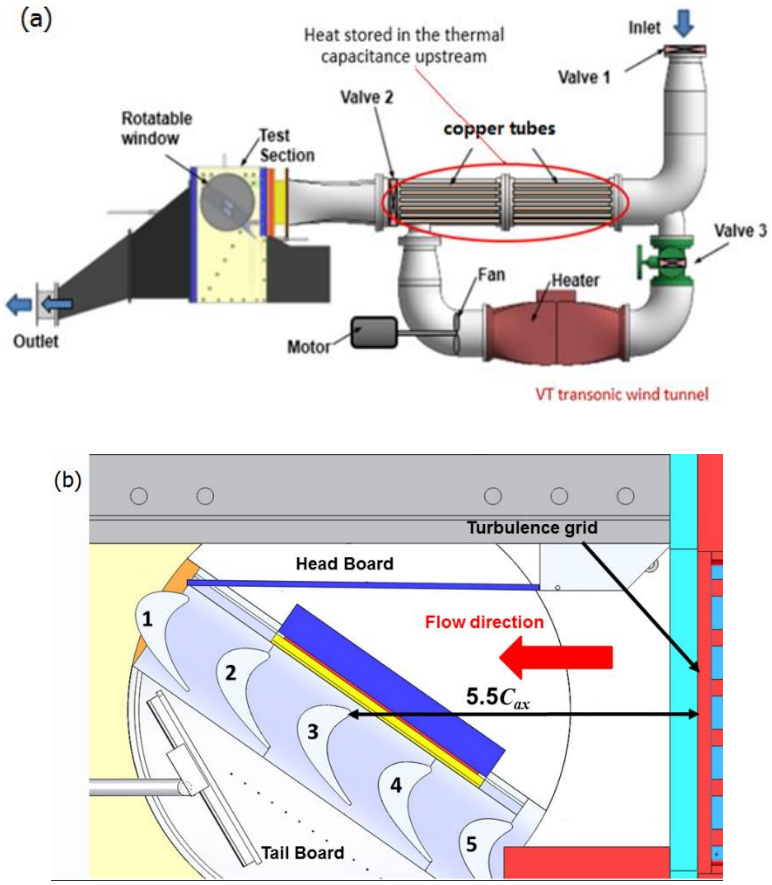

Figure C 1: Virginia Tech Transonic Wind Tunnel Facility: (a) over view of the wind tunnel; (b) close-up view of the test section.

The proposed data processing technique - Linear Regression Method is developed for heat transfer experiments performed at the Virginia Tech transonic, blow down, linear cascade wind tunnel facility, however, it is applicable for wind tunnels having similar transient characteristics. The Virginia Tech Transonic Wind Tunnel was designed to conduct aerodynamic and heat transfer investigations on gas turbine components. It is able to simulate the flow conditions of high freestream turbulence, transonic Mach numbers, and Reynolds numbers as experienced in realistic gas turbine engine environment. The prior heat transfer research that has been performed in this facility includes the work by Smith et al. [15], Popp et al. [16], Carullo et al. [17], Nasir et al. [1], Xue et al. [2], to list a few of them. Fig. C-1 shows the entire wind tunnel facility with the two-dimensional transonic linear cascade test section setup. Air is supplied from high pressure air tanks that are charged up to 1380 kPa (200 psig) prior to testing. A control valve regulates the mainstream flow to the test section. Cascade inlet pressures range from 20.7 kPa (3 psig) to 69.0 kPa (10 psig) depending on the objective test conditions. This blow-down facility is capable of sustaining a constant test section pressure for up to 15-20 seconds, with cascade exit Mach number ranging from 0.7 to 1.1, and a maximum mass flow rate of 5.0 kg/s.

During heat transfer experiments, the copper tubes upstream of the test section works as a thermal capacitor to store the heat energy produced by the closed loop forced convection heating loop before each tunnel run as shown in Fig. C-1. During the experiments, the mainstream flow is heated as it flows through the copper tube banks. The peak temperature of the mainstream air could reach up to 115°C approaching the test section. As the heater is turned off before start of each experiment, the thermal energy stored in the copper tubes decreases and therefore the air temperature decreases gradually. The tunnel response of the total temperature and Mach number of the mainstream flow is shown in Fig. C-2.

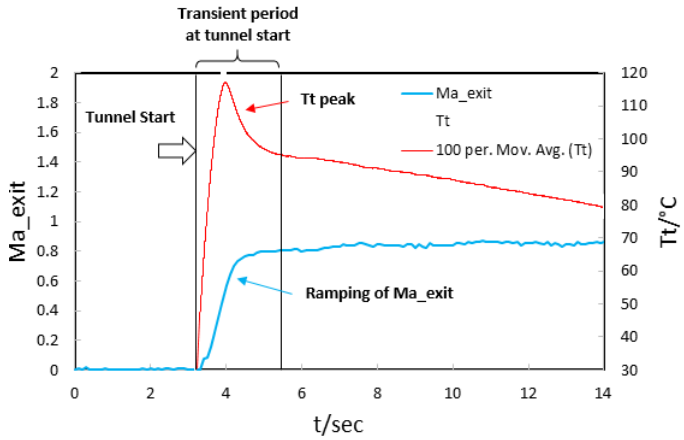

Figure C 2: Tunnel response of free stream temperature and Mach number

The Virginia Tech Transonic Wind Tunnel is characterized by its transient performance. As shown in Fig. C-2 there is about 2 seconds transition period before the Mach number reaches steady state. During this period, the Mach number ramps form 0.0 to 0.8 (or the desired isentropic exit Mach number). The HTC would follow similar characteristics as it is dependent on flow Reynolds number. In the present study, the mainstream temperature was

measured upstream of the test section using a total air temperature thermocouple, and used in the data processing time window as T_t in the calculation. The mainstream flow temperature approaches a peak of 115°C at about 1 second after the tunnel start, and then falls sharply. This peak is caused by the pre-heated air inside the copper tubes upstream of the test section before the tunnel starts. After about 2 seconds of the tunnel start, the pre-heated air is blown off, and the flow is heated only when it passes thought the copper tubes. Thereafter, the flow temperature ramps down gradually.

DATA PROCESSING TECHNIQUES IN TRANSIENT CONVECTIVE HEAT TRANSFER EXPERIMENT

As discussed above, in most convective heat transfer experiments, the same 1-D thermal conduction model is employed, and the heat transfer in both convective domain (boundary layer flow) and the conductive domain (inside the material) are calculated to obtain HTC and Eta. The major difference between different data processing techniques is on the approach to couple the information on thermal convection and conduction.

Curve fitting method for uncooled heat transfer experiment

In the curve fitting method, the surface temperature T_w and the mainstream temperature T_∞ form a Robin boundary condition (or third-type boundary condition) for the 1-D model (Eq. 2). The entire set of 1-D transient thermal conduction semi-infinite model with boundary condition can be described by Eq. (5).

$$\begin{cases} \dfrac{\partial T}{\partial t} = \alpha \dfrac{\partial^2 T}{\partial x^2} \\ k \dfrac{\partial T}{\partial x}\Big|_{x=0} = h(T_\infty - T_w) \\ T|_{x\to\infty} = T_i \\ T|_{t=0} = T_i \end{cases} \tag{5}$$

Where T_i is the initial temperature of the test section material. The initial temperature profile inside the material is uniform at the start of the tunnel run. The convection and conduction domains are coupled by the second row in Eq. (5). The closed form analytical solution of Eq. (5) can be expressed as (Incropera et al. [18])

$$\frac{T_w - T_i}{T_\infty - T_i} = 1 - \exp\left(\frac{h^2 \alpha t}{k^2}\right) erfc\left(\frac{h\sqrt{\alpha t}}{k}\right) \tag{6}$$

Equation (6) is an implicit function of h , which means a direct solution is not possible. Thus, a numerical approach is applied by using the time history of flow temperature T_∞ and a tentative trial of h value. The value of surface temperature (T_w) is calculated for each time step as shown in Eq. (7)

$$\left(T_w(t)\right)_{calculated} = T_i + \left(1 - \exp\left(\frac{h_{guess}^2 \alpha t}{k^2}\right) erfc\left(\frac{h_{guess}\sqrt{\alpha t}}{k}\right)\right)\left(T_\infty(t) - T_i\right) \tag{7}$$

$$error = T_w(t)_{calculated} - T_w(t)_{measured}$$

The difference between the measured T_w value and the calculated T_w value is carried out to obtain the error at each time instant. A standard numerical routine is used thereafter, that iteratively assumes the correct h value to minimize the sum of squares of error including all time steps during the data reduction period. During the iteration of Eq. (7), the calculated T_w curve approaches to the measured T_w value. Fig. C-3 shows a sample curve fit between measured and calculated values of test surface temperature for a single local data point.

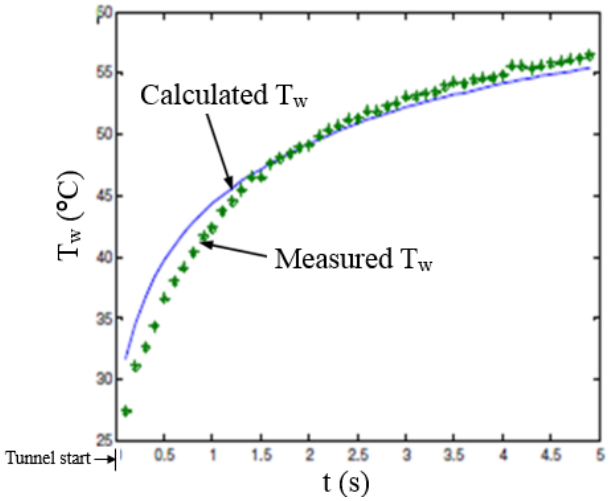

Figure C 3: Curve fitting of surface temperature data

The curve fitting method has been used extensively to calculate convective heat transfer coefficient distribution ([3], [7], and [9]). However, most of these experiments were performed at low speed wind tunnels and have the following limitations on its application to high speed blow down facilities.

1. The governing expression as shown in Eq. (6) is obtained assuming the mainstream reference temperature T_t remains constant for the entire time period. This condition can also hold true if the mainstream temperature experiences a step jump. However, as shown in Fig. 2, during the first 2 seconds, the mainstream temperature ramps up to a peak value and then experiences a sharp fall, and ramping down gradually thereafter. Therefore, this assumption leads to a certain amount of the error in the final result of HTC value for the present facility.

2. The second assumption for Eq. (6), which contributes a major part of the error in the Curve Fitting Method, is HTC remain constant during the data processing time window. However, as shown in Fig. C-2, it takes 2 seconds for the mainstream Ma to ramp from 0 to the designed condition (0.8). Since HTC is highly dependent on flow stability, this ramping in the first 2 seconds will result in the calculated HTC lower than the actual value.

3. The surface heat flux is based on mainstream fluid temperature that is measured upstream of the test section. Ideally for high speed flow applications, local recovery temperature should be counted for calculation of surface heat transfer.

In case of the curve fitting method, the convective calculation has to begin from the tunnel start, therefore the influence of the initial transient period cannot be avoided. As Kwak [9] summarized, the Duhamel's superposition theorem can be applied to count in the smooth ramping of flow temperature, using a series of steps. Thus, the first issue can be solved. However, the error caused by the non-uniform convective heat transfer due to the ramping of Ma/Re, which causes the HTC variation at the tunnel start, cannot be eliminated through the superposition method, so the second issue maintains. Compared to the first two issues, the error in final HTC result due to the third issue is not significant.

In some low speed wind tunnels, the HTC variation issue is avoided by switch on the instant heater after the steady mainstream is established. However, in most of the transient transonic wind tunnel, due to the large mass flow rate, when the instant heating is not be available the HTC variation issue is unavoidable.

Curve fitting method for film cooling heat transfer experiment

All assumptions as well as the fundamental 1-D semi-infinite model discussed above remain the same for film cooling cases. However, the mainstream temperature T_∞ in Eq. (5) has to be replaced by film temperature. It is also referred as the adiabatic film cooling temperature (T_{aw}), which governs the convective heat transfer to the surface wherever coolant film exists.

Introducing the definition of the film cooling effectiveness (Eq. 4) to the analytical solution of the 1-D semi-infinite model (Eq. 7), the final expression is given as:

$$T_w - T_i = \left[1 - \exp\left(\frac{h^2 \alpha t}{k^2}\right) erfc\left(\frac{h\sqrt{\alpha t}}{k}\right)\right] \times \left[\eta T_c + (1-\eta) T_\infty - T_i\right] \tag{8}$$

Since, one more unknown (η) is introduced, a two-test strategy is employed in order to solve for HTC and Eta simultaneously. Following this method, two similar transient film cooling tests are performed. The first test is carried out with mainstream at a high temperature and coolant at lower than ambient temperature and suddenly exposed to the test surface at ambient temperature initially. In the second test, the only difference is the coolant is heated up to a certain temperature instead of being cooled. The present curve fitting method differs to some extent from the method described in Ekkad et al.[3], where the coolant and mainstream temperatures cannot be matched due to tunnel characteristics as the mainstream air cannot be continuously heated during experiments. Nevertheless, generating two different data sets from two similar transient runs provides enough points to solve the two unknowns iteratively.

HTC and Eta are calculated simultaneously following the algorithm shown in Fig. C-4. The subprogram calculates

HTC at Step 4 using the method as described in uncooled heat transfer section as assuming no effectiveness over the entire surface to start with. However, HTC being a hydrodynamic parameter, is independent of coolant temperatures and should remain similar at corresponding locations during hot and cold coolant runs. Therefore, HTC is compared between hot and cold coolant runs at each pixel location and a tolerance limit of 10% is adopted due to measurement uncertainties. Finally, if the percentage difference of HTC between hot and cold coolant runs is within 10%, Eta = 0 is assigned for that location or otherwise, Eta is increased in steps of 0.01 and HTC is calculated again according to Eq. (3) in an iterative manner until the tolerance criterion is satisfied. The data reduction time window and limitations for this method remains the same as uncooled heat transfer described earlier.

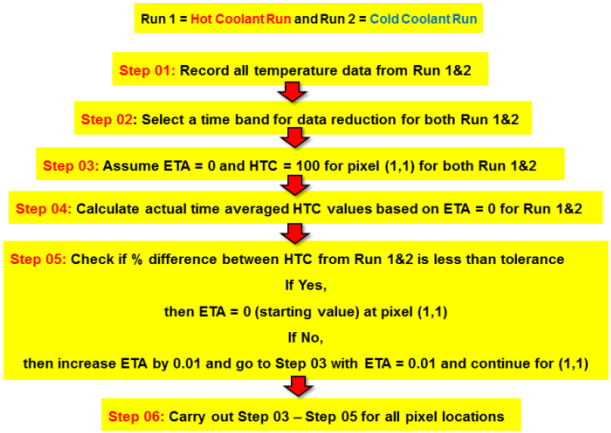

Figure C 4: Curve fitting scheme for film cooling data reduction

Linear regression method for un-cooled heat transfer experiment

Given the transient characteristic of Virginia Tech Transonic Wind Tunnel, another heat transfer data processing method was developed by Smith et al. [19] to determine the HTC in convective heat transfer experiments. In this method the surface temperature data is directly used to solve Eq. (2) as a Dirichlet boundary condition (or first-type boundary condition), and the entire set of 1-D semi-infinite model is expressed in Eq. (9).

$$\begin{cases} \dfrac{\partial T}{\partial t} = \alpha \dfrac{\partial^2 T}{\partial x^2} \\ T|_{x=0} = T_w(t) \\ T|_{x\to\infty} = T_i \\ T|_{t=0} = T_i \end{cases} \tag{9}$$

Using the solution of this model (Eq. 9) the surface heat flux history, $q(t)$, could be reconstructed. In the present study, this calculation is implemented by a 1-D finite difference code. Once the surface heat flux is reconstructed, the convective heat transfer coefficient can be estimated through a linear regression method descripted below.

The 1-D surface convection model is:

$$q = h(T_\infty - T_w) \tag{10}$$

In case of compressible flow the free stream temperature T_∞ has to be replaced by the local recovery temperature, T_r , so the convective equation becomes

$$q = h(T_r - T_w) \tag{11}$$

Rearranging Eq. (11), a linear relationship in the form of $\boldsymbol{y = ax + b}$ is obtained:

$$\underset{\text{y}}{q} = \underset{\text{a}}{h}\underbrace{(T_t - T_w)}_{\text{x}} + \underbrace{h(T_r - T_t)}_{\text{b}} \tag{12}$$

T_t is the mean flow total temperature, which varies at each time step. According to the definition of recovery temperature:

$$T_r = T_t - (1 - r)\frac{{u_\infty}^2}{2C_p} \tag{13}$$

Where, *r* is the recovery factor to incorporate the dissipation of energy from thermal boundary layer to mainstream, The value of the last term in Eq. (12), $b = h(T_r - T_t)$, depends only on the aerodynamic condition, and remains constant if the local Mach number does not change during the calculation time window. Theoretically, all the data points ($x = T_t - T_w, y = q$) should lie along a straight line, as shown in Fig. C-5. The slope of the fitting line provides the HTC value, and the recovery temperature can be estimated from the y intercept value ($T_r = T_t - \frac{y}{a}\Big|_{x=0}$).

In the Linear Regression Method, the total temperature of the flow does not have to be assumed step jump at tunnel start, but the HTC has to be constant in the data processing time window. However, one of the advantages of this method is that it splits the process in two steps, so that the error caused by the ramping of HTC and T_t at the starting of the tunnel running can be avoided.

Step1: While reconstructing the surface heat flux (solving Eq. 9), the calculation is performed within the conduction domain inside the solid material, and no data from the convective domain is required. Thus, any variation of HTC within the short duration before the mainstream Mach number reaches steady state does not have any influence on the surface heat flux result. For the present study, time window of this step is the first 7 second of the tunnel run.

Step 2: To estimate the HTC through linear regression (Eq. 12), the calculation is carried out in the convective domain. However, the data processing time window can be chosen suitably to avoid the transition period of the tunnel start, so that the HTC remains constant during the calculation. For the present study, time window of this step

is between 2 seconds and 7 seconds after the tunnel start.

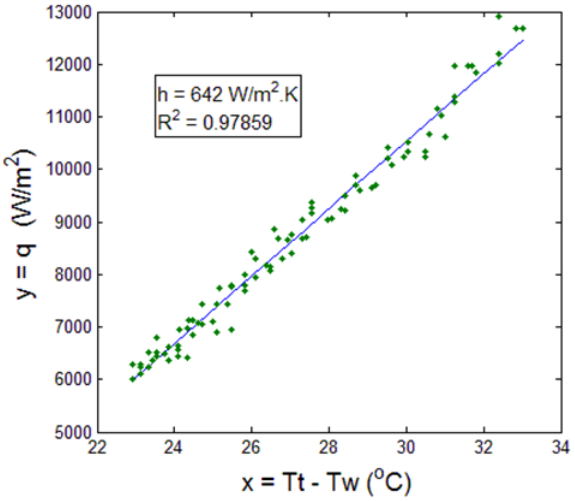

Figure C 5: Linear regression of surface temperature and heat flux data

The data reduction time windows of these two steps for linear regression method are shown in Fig. C-6. The heat flux reconstruction has to begin from the tunnel start, because a uniform condition of the initial temperature in the material is necessary to solve Eq. (9). The curve fitting method time window is also included in Fig. C-6 for comparison.

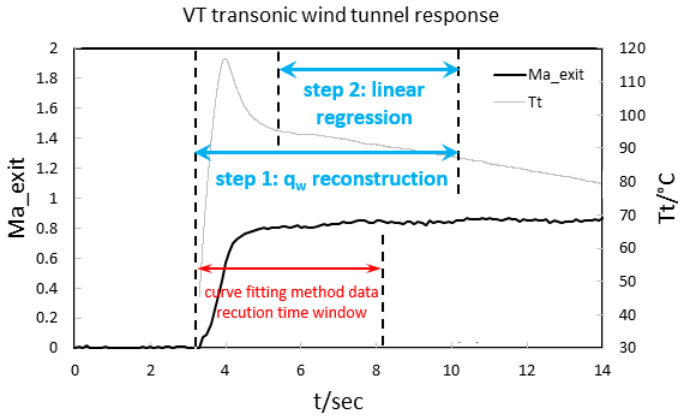

Figure C 6: Data processing time window

Linear regression method for film cooled heat transfer experiment

For film cooling experiments, a novel application of linear regression method named as Dual-Coolant Linear Regression Method is proposed. In this method, similar two-test strategy as described earlier is adopted. The two sets of data are recorded at the same aerodynamic conditions with the same mainstream Mach number and

temperature, and the same coolant blowing ratio, but of different coolant temperatures. In the present study, the temperature of hot coolant (about 40^0C) is higher than the temperature of cold coolant (about 15^0C), but is much lower than the hot main flow temperature (around 100^0C).

Each of the two sets of data is first processed respectively by the Linear Regression Method discussed above. However, unlike for the non-film cooling experiment, one more unknown (η) is included, and Eq. (12) cannot be solved directly. To go through the calculation, an initial guess of T_r value is given. (It will be shown later, that the mainstream total temperature is a reasonable starting value of T_r guessing to begin the optimizing iteration.) Thereafter, the two sets of data can be plotted with $x = \frac{T_t - T_w}{T_t - T_c}$, and $y = \frac{q}{T_t - T_c}$, as shown in Fig. C-7. It can be observed the two sets of data point follow their own trend lines respectively, and the quality of the alignment is poor initially.

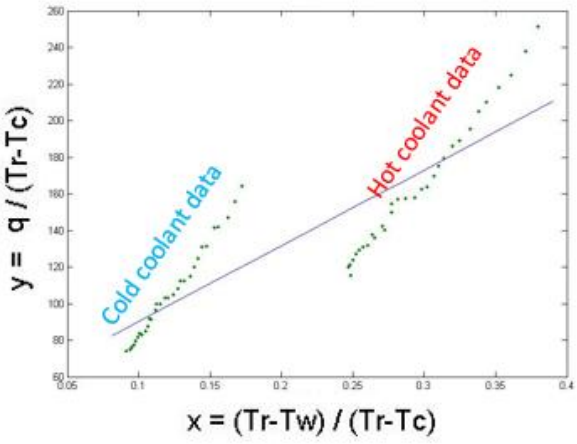

Figure C 7: Linear regression of two data sets calculated with tentative guessed Tr value

Ideally, if the two experiments are performed at similar mainstream aerodynamic condition, and the same coolant blowing ratio, HTC and Eta values should remain identical, which means the two sets of data should line up perfectly. The disagreement of the hot and cold coolant data trends shown in Fig. C-7 is because the first guess of T_r disagree with the correct value. The second step is to find the correct T_r to make the two sets of data line up. In linear regression calculation, the indicator of the alignment quality of a data set is the R-square value (R^2). The R^2 is close to unit means the data points are perfectly aligned. The essential assumption in this step is that through the optimization iteration, the correct T_r can be found to provide the value of R^2 closest to unity.

$$\underset{T_r}{\operatorname{argmin}}\{1 - R^2(T_r)\} \tag{14}$$

Figure C-8 shows a typical relationship between the normalized recovery temperature, $C_r = T_r/T_t$, and R^2 value in the current type of heat transfer studies. Based on our understanding of the physics, the local peak on the right is the searching objective. It is easy to see that $C_r = 1$ is a reasonable starting guess, which in most of the cases guarantees the searching converges to the objective point. Many optimization algorithms work for this searching process. In the

present study, the Gradient Descent Method is employed for its simplicity and stability in local searching operation. It is worthy to point out, that a global searching method is not preferable in the present calculation, as it may converge to the singular area on the left, which provides negative HTC as shown in Fig. C-9.

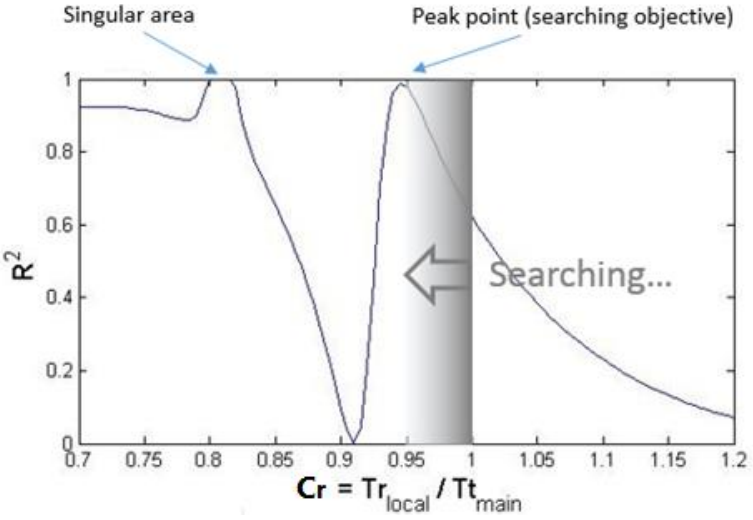

Figure C 8: Typical relationship between R-square and normalized recovery temperature

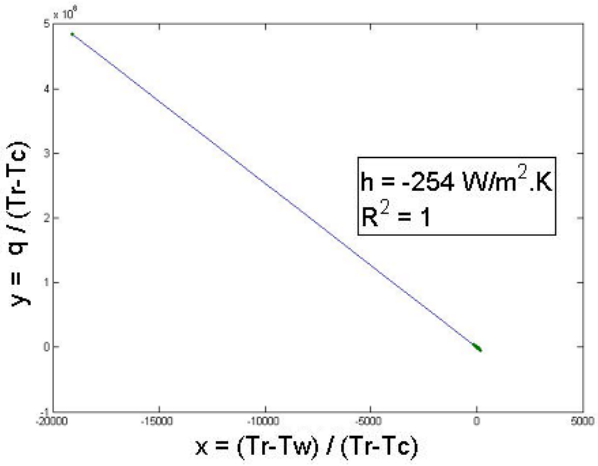

Figure C 9: Dual-Coolant Linear regression plot when Searching converged in singular area

Figure C-10 shows a few snapshots of the iteration process. As the T_r approaches to the correct value, the alignment quality (R^2) of the two data set is being improved. One major assumption has to be pointed out here is that the effect of change in density ratio of the coolant due to heating or cooling will be insignificant on the film cooling flow. This assumption is based on the research reported by Ekkad et al. [20]. According to their study, the density ratio impact on HTC and Eta is secondary. In most of the studies performed in the present test facility, the discrepancy of the density ratio of cold and hot coolant test is less than 15%. Thus, the error caused by the density ratio disagreement between the two data sets is negligible.

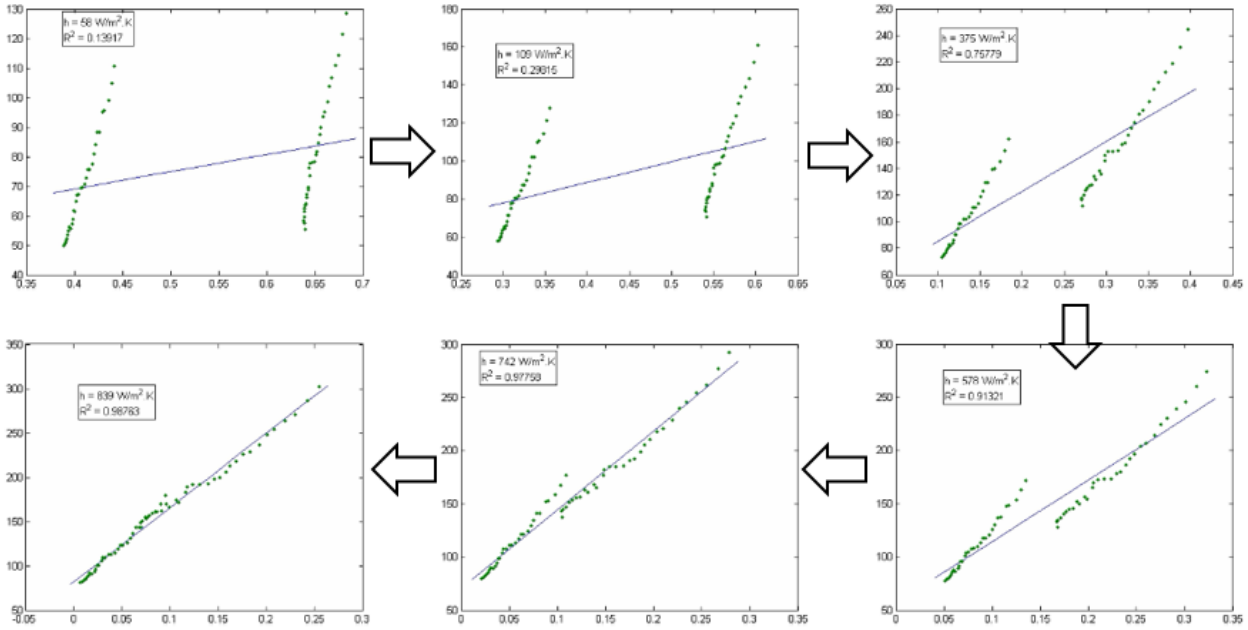

Figure C 10: Different steps of the searching process for Dual-Linear-Regression

UNCERTAINTY

Curve fitting method

For curve fitting method, the uncertainty in the calculation of HTC values was calculated using Kline and McClintok's method [21] and was found to be about on average ±9.5% of the local HTC value. This uncertainty value does not include the error caused by the ramping effect at the tunnel start. Detailed uncertainty analysis on HTC has been provided in Panchal et al. [22]. The overall uncertainty in Eta values for film-cooled cases is fixed at 10% due to step size resolution.

Linear regression method

For linear regression method, different uncertainty analysis methods are applied in the two data processing steps respectively. In step 1, the surface heat flux is reconstructed by a finite-difference code, and no explicit equations can be formulated for this process, the propagation of the major errors is analyzed through the Moffat's perturbation method [23]. In step 2, linear regression uncertainty analysis is carried out though the method recommended by Coleman and Brown [24]. The average uncertainty of HTC is about ±8.0% and ±0.08 for Eta. The detailed uncertainty analysis can be found in Xue's thesis [25].

COMPARISON OF RESULTS

In this section, the two data processing methods are used to reduce the same set of experimental data for a comparative discussion. The heat transfer results presented here are for a high pressure turbine endwall with high turning airfoils operating under transonic conditions. All the measurements were performed at exit isentropic Mach

number 0.88 and at design incidence, where the inlet Mach number is 0.45 and inlet Reynolds number based on axial chord is about 9 x 10^5. Transient IR thermography technique was used for direct measurement of endwall surface temperature. Due to proprietary nature of the data any information on actual heat transfer coefficient values as well as test section design details may not be provided. The primary objective of this paper is to present the comparison of heat transfer results obtained by the two data reduction methods, therefore a detailed discussion on secondary flows or associated endwall heat transfer patterns is not necessary.

Un-cooled heat transfer results

Figure C-11 shows a comparison of results obtained from the two data reduction methods described earlier with an analytical expression, $Nu = 0.0300{Re_x}^{0.8}Pr^{0.6}$ (Kays and Crawford [26]). This semi-empirical correlation is used to find Nusselt number on a flat plate a turbulent boundary layer with constant heat flux boundary condition. The experimental results are obtained at 1.0Cax upstream of the leading edge where uniform flow patterns are expected which can be approximated as flat plate study where, location of the turbulence grids are considered equivalent to the edge of the flat plate. Since the free stream turbulence intensity in the present experiment is relatively high (*Tu*=8%), the actual Nusselt number is expected to be slightly higher than the analytical result, which agrees fairly well with the linear regression result. Therefore, it is reasonable to believe that the linear regression provides more accurate result than the curve fitting method in this case.

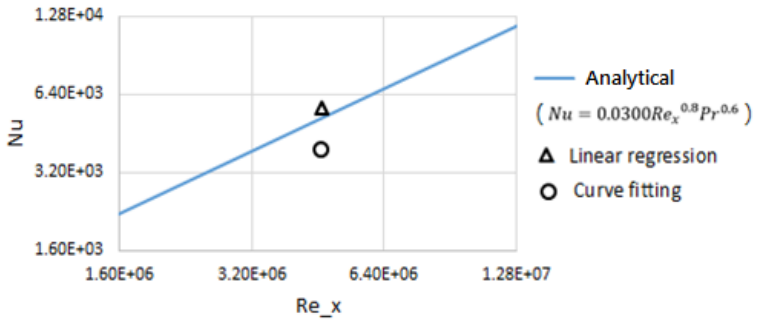

Figure C 11: Technique validation with Nusselt number comparison

Figures C-12 (a) and (b) respectively show the Nusselt number distribution obtained using Linear Regression Method and Curve Fitting Method, whereas Fig. C-12 (c) shows Curve Fitting Method result again, however, at a different color scale for clarity and identification of distinct local heat transfer features. The Nusselt number distribution provided in Fig. C-12 is calculated based on the axial chord of the airfoil. Higher Nusselt number on the endwall represent higher heat transfer regions. Endwall heat transfer is highly dependent on secondary flow features and formation of complex vortices.

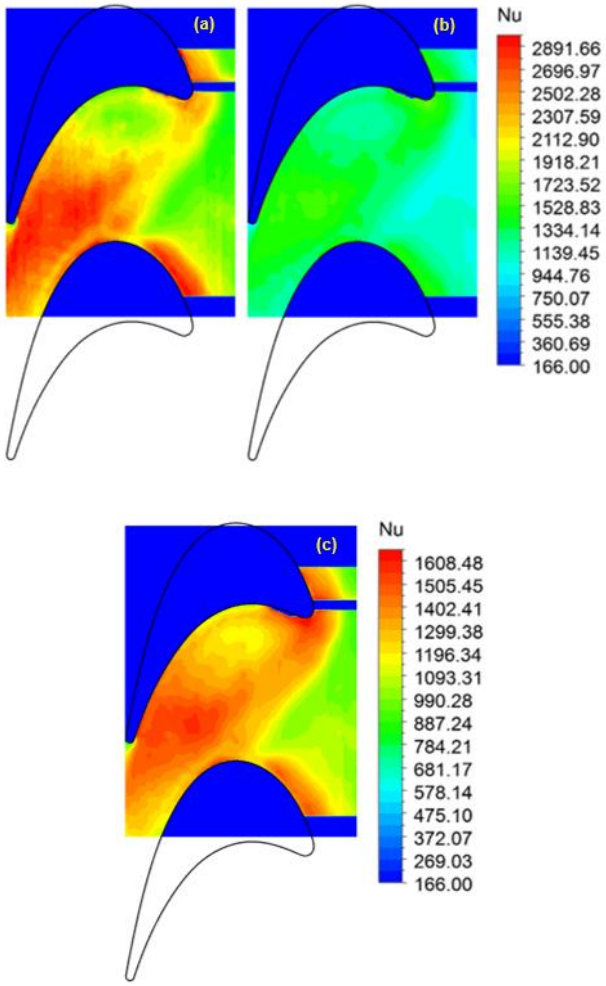

Figure C 12: Comparison of Nusselt number distribution using (a) Linear Regression method, (b) Curve Fitting method, and (c) Curve fitting method using reduced color scale

These local heat transfer characteristics are evident from both Figs. C-12 (a) and (c) which delineates the fact that both data reduction methods are able to capture the flow physics qualitatively and differ only from the Nusselt number level perspective. The overall area averaged Nusselt number is about 40% lower using curve fitting method as seen in Fig. C-12 (b) compared to Fig. C-12 (a). The major reason attributed towards this discrepancy is embedded in the assumptions of the data reduction techniques. Curve fitting method calculates a lower Nusselt number for a certain location compared to linear regression method, primarily because it takes into account the initial tunnel flow development period while calculating HTC during the data reduction window. A constant HTC guess value is assumed to fit all the data points, during the entire data acquisition time window, which is typically about 5 seconds, as shown in Fig. 3. However, the HTC is not constant due to the Mach number ramping in the duration of the flow development period, which is typically about 2 seconds. Therefore, the best fit on experimental data would compromise accuracy during the initial period where, the heat transfer is low, resulting in lower heat transfer coefficient as well. Time averaging HTC over these data points reduces the overall HTC level. Moreover,

the free stream total temperature taken as the reference fluid temperature in Curve fitting method also decreases as time progresses resulting in higher driving temperature potential, therefore lowering HTC values. However, the linear regression result indicates that the local recovery temperature, T_r, is about on average 2°C lower than the mean flow total temperature, T_t. This contributes another part of the error which results in a lower HTC than the correct value.

Film cooling experiment results

Figure C-13 shows endwall Nusselt number distribution for the same geometry, however in presence of 1.0% MFR (coolant to free stream mass flow ratio per passage) leakage flow from an upstream purge slot. The purge slot is located at 0.3Cax upstream of the leading edge of the airfoil. The measurements were performed at the same mainstream condition as the non-film cooling experiment discussed above.

Similar to uncooled endwall heat transfer distribution, the qualitative nature of endwall heat transfer characteristics and flow structure depicted from both data reduction methods remain similar except at the near upstream region where interaction between coolant and pressure side leg of horse-shoe vortex is prominent for Curve Fitting Method. This is due to turbulence created by coolant jet during the initial transient period which is included in the Curve Fitting Method. Similarly, quantitative comparison between the two data reduction techniques reveals significant difference in endwall Nusselt number level. The major reason behind this discrepancy is attributed towards inclusion of tunnel flow development period for Curve Fitting Method and detailed description remains similar to explanation provided earlier in the uncooled heat transfer case.

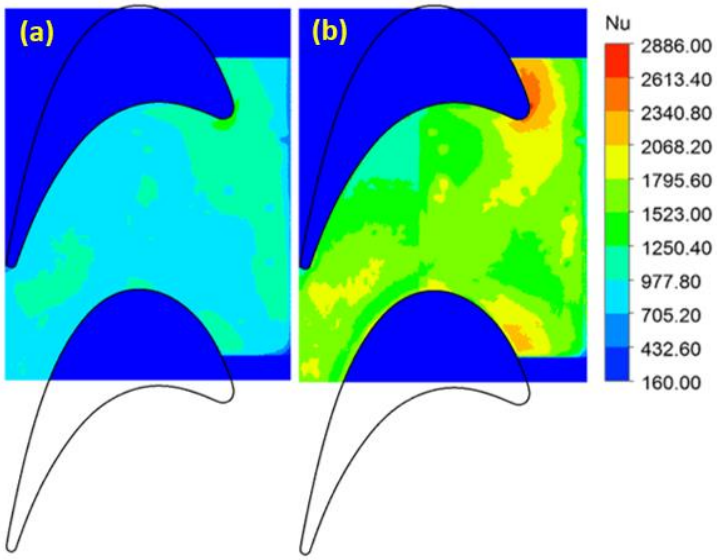

Figure C 13: Endwall Nusselt number distribution with 1.0% MFR slot cooling (a) Curve Fitting method, (b) Linear regression method

Comparison of endwall adiabatic effectiveness distribution obtained using Curve Fitting Method and Linear

Regression Method is shown in Fig C-14. The results from two methods agree with each other both qualitatively and quantitatively. It seems the ramping of Mach number at the tunnel start has less impact on the adiabatic effectiveness than it has on the HTC or Nusselt number.

The coolant ejected from the leakage slot creates a layer of thin film, thus prohibiting the hot mainstream to be in direct contact with the endwall surface. Regions where coolant is present, endwall heat transfer takes place due to temperature differential between the film and the endwall surface. Since the film temperature is always less than the mainstream temperature, the net heat flux to the endwall surface decreases. Eta values close to unity signifies that the region is highly affected by coolant flow, whereas Eta values close to zero means effect of coolant is either negligible or absent. Due to the formation of the passage vortices, the extent of the purge flow is contained within the triangular region upstream of the horse-shoe vortex and the cross passage pressure differential between the airfoils helps to move the coolant more towards the suction side of the blade.

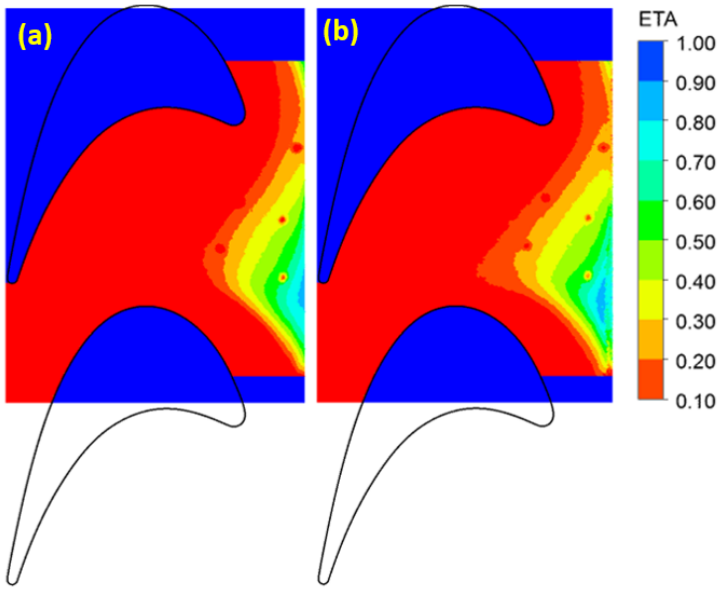

Figure C 14: Endwall adiabatic effectiveness distribution for 1.0% MFR purge flow (a) Curve fitting method, (b) Linear regression method

FURTHER DISCUSSION ON LINEAR REGRESSION METHOD

Recovery temperature issue in un-cooled heat transfer experiment

As described above, the Linear Regression Method assumes the discrepancy between the total temperature and the recovery temperature ($T_r - T_t$) constant. This is based on Eq. (10), and the assumption that flow velocity stays constant. However, in most of the wind tunnel, the control objective parameter is Mach number. When there is a significant variation of free stream temperature during the data reduction time window, even with a constant Mach number, the flow velocity may change. In that case, another format of convective heat transfer equation is recommended for linear regression.

The heat capacity of the flow can be written in

$$C_p = R\frac{\gamma - 1}{\gamma} \tag{15}$$

and the velocity can be converted in Mach number through the following equation

$$M_a{}^2 = \frac{u_\infty{}^2}{\gamma R T_\infty} \tag{16}$$

Introduce Eq. (15) and Eq. (16) to Eq. (13), a proportional relationship can be derived between T_r and T_t.

$$T_r = T_t \frac{1 + r\frac{\gamma - 1}{2} M_a{}^2}{1 + \frac{\gamma - 1}{2} M_a{}^2} \tag{17}$$

Eq. (13) can be written in a simplified way as

$$T_r = T_t \cdot C_r \tag{18}$$

where the factor, C_r, only depends on Mach number. Introducing C_r to the convective heat transfer Eq. (11), and normalizing by total temperature, T_t, on both sides, another linear relationship is obtained in the form of $\boldsymbol{y = ax + b}$:

$$\underbrace{\frac{q''}{T_t}}_{y} = \underbrace{-h}_{a}\underbrace{\frac{T_w}{T_t}}_{x} + \underbrace{hC_r}_{b} \tag{19}$$

Equation (19) is applied when the flow temperature varies dramatically during the data reduction time window. In the present study, since the change of mainstream temperature in the linear regression time window is small (-5°C from t=2s to t=7s), the variation of velocity is small. Therefore, the difference between the final convective heat transfer coefficients between Eq. (12) and (19) is negligible.

Recovery temperature issue in film cooling experiment

In some cases the local recovery temperature, T_r on the film cooled surface is assumed to be equal to the un-cooled surface. Therefore, T_r value is obtained either from the uncooled experiments performed on the same test model, or from simple estimations through the empirical correlations (Eq. 13).

However, since the coolant injection disturbs the main stream boundary layer, usually a new sub-layer establishes

from the injection holes, and the local boundary layer flow condition is totally different from the non-injected surface. Therefore, it is not reasonable to expect the film cooled surface share the same T_r value with the non-film cooled surface. In the proposed Dual-Linear-Regression Methods, a more reasonable assumption – the discrepancy between free stream total temperature and surface recovery temperature ($b = T_r - T_t$) stays the same for the cold and hot coolant tests – is adopted. Thus, the proposed data processing technique is believed to provide more accurate and reliable results.

CONCLUSIONS

A novel heat transfer data reduction method has been developed for improved quantitative measurements applicable under realistic gas turbine operating conditions. The presented paper also compares the proposed method (Linear Regression Technique) with one of the widely used data analysis technique (Curve Fitting) in literature involving convective heat transfer measurements in presence of external cooling features in gas turbine hot gas path. The major conclusions that can be drawn from the entire analysis described earlier in this paper are summarized as follows:

- The Linear Regression method has been shown to be beneficial under engine representative flow conditions. The effects of compressible flow physics, transonic aero-thermodynamic conditions have been successfully incorporated to obtain more accurate heat transfer parameters.
- Simultaneous calculation of key heat transfer parameters in presence of film cooling conditions – heat transfer coefficient and adiabatic film cooling effectiveness, is also a salient feature of the Linear Regression Method.
- The Linear Regression method effectively takes into account the mainstream flow development period and has the capability to calculate heat transfer parameters under stable aerodynamic conditions in a large scale blow down wind tunnel facility. Thus, heat transfer measurements can be carried out efficiently in short duration experiments with matching Reynolds number and Mach number conditions without the need of continuous flow set up arrangements.
- Although the effect of selection of data reduction technique (Linear Regression vs Curve Fitting) on adiabatic film cooling effectiveness is not significant, heat transfer coefficient levels seems to be largely influenced by inclusion of proper aero-thermal and physical conditions via the Linear Regression method. Appropriate calculation of recovery temperature, associated heat flux and exclusion of the initial transient period has been observed to increase local Nusselt number levels by as much as 60% compared to the Curve Fitting method using identical data sets.
- Effect of varying mainstream temperature has been implemented with the analysis procedure of Linear Regression method. This feature provides a huge benefit in terms of cost effectiveness, where setting up heating systems for mainstream air in large scale facilities to maintain constant temperatures (even in the range of 80°-100°C) with very high mass flow rates (~ 4-5 kg/s) is exorbitantly expensive. The current set up with closed loop heat exchanger system at Virginia Tech facility as described earlier, thus presents one of the convenient approaches to attain higher mainstream temperatures as it approaches the test section.

Future work on Linear Regression Method will focus on incorporating coolant density variation effects due to change in coolant temperatures between the hot and cold coolant runs. This will further improve heat transfer data accuracy and minimize error bars on the calculated parameters.

ACKNOWLEDGEMENT

The authors are grateful to grduate student and colleague Jacob Delimont at Virginia Tech for his discussions related to the fundamentals of the linear regression method.

NOMENCLATURE

a	slope in linear regression plot
b	intersect in linear regression plot
Cax	axial chord of test blade
Cp	thermal capacity [J/(K·kg)]
Cr	normalized recovery temperature
h	convective heat transfer coefficient [W/(m^2·K)]
k	thermal conductivity [W/(m·K)]
Ma	Mach number
q	heat flux [J/(m^2·t)]
R^2	linear regression alignment quality factor
Re	Reynolds number
R	specific gas constant [J/(mol·K)]
r	recovery factor
Tu	turbulence intensity
T	temperature [K]
t	time [s]
u	velocity [m/s]
x	distance from the surface to the solid material [m]

Greek Symbol

α thermal diffusivity [m^2/s]

η adiabatic film cooling effectiveness

ρ density [kg/ m^3]

γ adiabatic index (ratio of heat capacities)

Subscripts

aw adiabatic parameters

c coolant parameters

i initial condition

r recovery parameters

t total condition

w wall surface parameters

∞ free stream parameters

REFERENCES

[1] Nasir, S., Carullo, J.S., Ng, W.F., Thole, K.A., Wu, H., Zhang, L.J., and Moon, H.K., 2009, "Effects of Large Scale High Freestream Turbulence, and Exit Reynolds Number on Turbine Vane Heat Transfer in a Transonic Cascade," *ASME J. Turbomach*., 131, 021021.

[2] Xue, S., Ng, W., Moon, H.K., and Zhang, L., 2012, "Fan-Shaped Hole Film Cooling on Turbine Blade in a Transonic Cascade with High Freestream Turbulence," 50th AIAA Aerospace Sciences Meeting, Nashville Tennessee, Jan 2012, AIAA-2012-0368.

[3] Ekkad, S.V., and Han, J.C., 2000, "A transient liquid crystal thermography technique for turbine heat transfer measurements", Meas. Sci. Technol., 11, pp. 957-968.

[4] Kwak J. S., Ahn J., Han J., 2004, "Effects of rim location, rim height, and tip clearance on the tip and near tip region heat transfer of a gas turbine blade," *International Journal of Heat and Mass Transfer*, 47 (2004) 5651–5663.

[5] Christophel J. R., Couch E., Thole K. A., Cunha F. J., 2005, "Measured Adiabatic Effectiveness and Heat Transfer for Blowing From the Tip of a Turbine Blade," *ASME J. of Turbomachinery*, 2005, Vol. 127 pp 251-262.

[6] Anto, K., Xue, S., Ng, W.F., Zhang, L.J., Moon, H.K., 2013, "Effects of Tip Clearance Gap and Exit Mach

Number on Turbine Blade Tip and Near-Tip Heat Transfer," *ASME TURBO EXPO 2013*, GT2013-94345.

[7] Vedula, R. J., and Metzger, D. E., 1991, "A Method for Simultaneous Determination of Local Effectiveness and Heat Transfer Distribution in Three-Temperature Convection Situations," ASME 91-GT-345.

[8] Chambers, A. C., Gillespie, D. R. H., Ireland, P. T., and Dailey, G. M., 2003, "A Novel Transient Liquid Crystal Technique to Determine Heat Transfer Coefficient Distributions and Adiabatic Wall Temperature in Three-Temperature Problem", J. Turbomachinery Vol. 125, pp. 538-546.

[9] Kwak, J. S., 2008, "Comparison of Analytical and Superposition Solutions of the Transient Liquid Crystal Technique," Journal of Thermophysics and Heat Transfer, Vol. 22, No. 2, pp 290-295.

[10] Giel, P.W., Thurman, D.R., Van Fossen, G.J., Hippensteele, A.A., and Boyle, R.J., 1998, "Endwall heat transfer measurements in a transonic turbine cascade", J. Turbomachinery, 120, pp. 305-313

[11] Nicklas, M., 2001, "Film-Cooled Turbine Endwall in a Transonic Flow Field: Part II – Heat Transfer and Film Effectiveness", J. Turbomachinery, 123, pp. 720-729.

[12] Jonsson, M., Charbonnier, D., Ott, P., and von Wolfersdorf, J., 2008, "Application of the transient heater foil technique for heat transfer and film cooling effectiveness measurements on a turbine vane endwall", ASME Paper No. GT2008-50451.

[13] Vogel, G., Wagner, G., and Bolcs, A., 2002, "Transient Liquid Crystal Technique combined with PSP for Improved Film Cooling Measurements", The 10th Int. Symp. Flow Visualization, Kyoto, Japan, F0109.

[14] O'Dowd, D., Zhang, Q., Ligrani, P., He, L., Friedrichs, S., 2009, "Comparison of Heat Transfer Measurement Techniques on a Transonic Turbine Blade tip," ASME TURBO EXPO 2009, GT2009-59376.

[15] Smith, D.E., Bubb, J.V., Popp, O., Grabowski, H.C., Diller, T.E. Schetz, J.A. and Ng. W.F., 2000, "Investigation of Heat Transfer in a Film Cooled Transonic Turbine Cascade, Part I: Steady Heat Transfer," *ASME* 2000-GT-202.

[16] Popp, O., Smith, D.E., Bubb, J.V., Grabowski, H.C., Diller, T.E. Schetz, J.A. and Ng. W.F., 2000, "Investigation of Heat Transfer in a Film Cooled Transonic Turbine Cascade, Part II: Unsteady Heat Transfer," *ASME* 2000-GT-203.

[17] Carullo, J. S., Nasir, S., Cress, R. D., Ng, W. F., Thole, K. A., Zhang, L. J., and Moon, H. K., 2011, "The Effects of Freestream Turbulence, Turbulence Length Scale, and Exit Reynolds Number on Turbine Blade Heat Transfer in a Transonic Cascade," *ASME J. Turbomach*., 133, 011030.

[18] Incropera, F. P., et al., 2007, "Fundamentals of heat and mass transfer," 6th edition. Publ. John Wiley & Sons.

[19] Smith, D.E. 1999, "Investigation of Heat Transfer Coecient and Film Cooling Effectiveness in a Transonic Turbine Cascade," M.Phil. thesis, Virginia Polytechnic Institute and State University.

[20] Ekkad, S. V., Zapata, D., and Han, J.C., 1997, "Film Effectiveness Over a Flat Surface with Air and CO2 injection Through Compound Angle holes Using a Transient Liquid Crystal Image Method," ASME Journal of Turbomachinery, Vol. 119, No. 3, pp. 587-593.

[21] Kline, S. J. and McClintok, F. A., 1953, "Describing uncertainties in single sample experiments," Mechanical Engineering, pp. 3-8.

[22] Panchal K. V., Abraham S, Ekkad S. V., Ng W., Lohaus A. S., and Crawford M. E., 2012, "Effect of Endwall

Contouring on a Transonic Turbine Blade Passage: Part 2 — Heat Transfer Performance," *ASME* GT2012-68405

[23] Moffat, R. J., 1988, "Describing Uncertainties in Experimental Results," Exp. Thermal and Fluid Science, 1, pp. 3-17.

[24] Coleman, H. W., Brown, K. H., and Steele, W. G., 1995, "Estimating Uncertainty Intervals for Linear Regression," AIAA-1995-0796.

[25] Xue S., 2012, "Fan-Shaped Hole Film Cooling on Turbine Blade and Vane in a Transonic Cascade with High Freestream Turbulence," Ph.D. thesis, Virginia Polytechnic Institute and State University.

[26] Kays W. M., Crawford M. E. 2004, "Convective Heat and Mass Transfer (4th edition)," McGraw-Hill, Boston, MA.

Appendix – D

EXPERIMENTAL VALIDATION OF SYNGAS COMPOSITION OF AN ENTRAINED FLOW GASIFIER MODEL UNDER DIFFERENT OPERATING CONDITIONS

Arnab Roy* **Srinath V Ekkad** **Uri Vandsburger**

arnab8@vt.edu sekkad@vt.edu uri@vt.edu

Department of Mechanical Engineering
Virginia Polytechnic Institute and State University
Blacksburg, VA-24061
USA

Proceedings of the 28th International Pittsburgh Coal Conference, Pittsburgh, USA, September 12-15, 2011

ABSTRACT

A computational fluid dynamics (CFD) based model of a single stage, dry-feed, down-flow entrained flow gasifier is developed and the effect of oxygen (O_2)/coal and steam (H_2O)/coal feed ratios on syngas composition is investigated. The model is set up using a coupled Eulerian-Lagrangian technique, where the continuous fluid phase is modeled in Eulerian approach and the trajectory of the coal particle is calculated in Lagrangian frame. The two phases are coupled by appropriate source terms in the conservation equations. Global gas phase homogenous reactions are implemented in species transport model and the Discrete Phase Model (DPM) is used to account for the devolatilization and heterogeneous char gasification reactions. Steady state model predictions of the effective syngas composition ($CO+H_2$) at different O_2/coal and H_2O/coal ratios are compared with benchmark experimental data from literature and found to be in good agreement within the error bounds of the experiment. Results show gasifier exit temperature increase with increase in O_2/coal ratio, whereas it is found to decrease with increase in H_2O/coal ratio. The species composition also has a similar trend where it can be observed that the amount of syngas production is lower with increase of steam feed rate than compared to increase in oxygen feed rate. This can be attributed to the effect of water gas shift reaction which promotes the formation of CO_2 at higher steam concentrations. The further decrease in syngas production with increase in O_2/coal feed ratio (greater than 1) is due to the increased burning rate of coal which in turn lowers the residence time as a result of excess of O_2 supply. The simulation also provides detailed information of temperature and species concentration distribution inside the gasifier which indicates the three different reaction zones for devolatilization, gasification and reduction. A validated set of parameters are thus obtained that can be employed to improve design conditions for experiment. The model validation also provides the basis to achieve further accuracy incorporating complex effects such as detailed reaction mechanisms and effect of ash deposition.

INTRODUCTION

The annual world energy consumption as predicted by Environmental Information Administration (EIA) [1] would increase to 700 exajoules (EJ) by the end of 2030, i.e. more than 45% of the present demand. The major threat of global climate change is a direct consequence of this huge demand in energy. The dominant contributor of climate change are the increased level of greenhouse gases especially carbon di-oxide (CO_2), where coal is the major source of CO_2 emission into the atmosphere. Effective and economic utilization of coal, thus protecting the environment producing less CO_2 and other pollutants during thermo-chemical processes need employment of efficient conversion techniques. Gasification has been an important part of energy conversion process and a key initiative towards clean coal technology for the foreseeable future. Public Utility Commissions have identified Integrated Gasification Combined Cycle (IGCC) plants for power generation as the best available control technology (BACT) [2]. Gasification is a process to convert carbon containing fuel into a mixture of H_2 and CO, known as synthesis gas via incomplete combustion of a concurrent stream of oxidant (O_2 or air) and steam or water. One of the major applications of the syngas produced is to use it as a source of fuel in a gas turbine where syngas at high temperature and pressure is fed to the turbine from the gasifier in an IGCC plant. Syngas can also be used for manufacturing ammonia, synthetic natural gas and several other chemical products in refineries. Entrained flow gasifiers are slagging type, hence ensuring operation above ash melting point and more commonly used in industrial applications due to fuel flexibility, high degree of carbon conversion and tar free syngas production. Typically, commercial entrained flow gasifiers operate at very high temperature (1600-2000K) and pressure (up to 50 atm) with pulverized dry or slurry particles (size < 0.1mm) as feedstock. Entrained flow gasification constitutes of the following physical and chemical sub processes (1) Vigorous mixing of inlet oxidizing stream and pulverized coal particles, (2) Inert heating and moisture release of the coal particles, (3) Devolatilization, where the volatile matter within coal breaks up in an oxygen lean environment releasing mixture of gases comprising of mainly CO, CH_4, H_2S and leaving solid char particle residue, (4) Heterogeneous reactions where solid char particle reacts with O_2, CO_2 and H_2O to produce a mixture of CO, H_2, CO_2, H_2O and trace amount of CH_4, (5) Homogeneous gas phase equilibrium reactions controlling the syngas composition and finally (6) Ash and slag formation. CFD modeling is a powerful tool that provides necessary predictive capacity for performance and design optimization and delineates the underlying processes inside a reactor. The entrained flow gasifier model for the present work is developed using commercial finite volume based software ANSYS FLUENT.

BACKGROUND

Extensive studies on CFD modeling of entrained flow gasifiers with varying level of complexity are available in published literature. The modeling study by Wen and Chuang [3] has been a pioneering work in entrained flow gasification research. They developed a mathematical model and distinguished three separate zones in a gasifier: the Pyrolysis and volatile combustion zone, the gasification and combustion zone and the gasification zone. Different reaction kinetic mechanisms were considered for each zone in order to better understand the critical parameters affecting performance of the gasifier. In the modeling work of Govind and Shah [4], an entrained bed gasifier is simulated using coal liquefaction residues and coal water slurry as feedstocks. Smoot and co-authors [5-7] at

Brigham Young University developed in-house mathematical model PCGC (Pulverized Coal Gasification and Combustion) and predicted that rapid devolatilization occur near the inlet region where the particle surface reactions are controlled by oxidizer diffusion. The model also incorporates various equilibrium gas phase reactions and turbulence models. Vamvuka et al. [8] presented a one-dimensional steady state model of oxygen blown gasifier and pointed out the dependence of three critical parameters: steam/coal ratio, oxygen/coal and gasifier pressure on performance and reactor temperature. Chen et al. [9] developed a comprehensive 3-D entrained flow gasifier model using Multi Solids Progress Variables (MSPV) method. The numerical simulations were carried out for a two stage inlet 200 tpd commercial scale gasifier. The model predicted that carbon conversion in a two stage entrained flow gasifier depends primarily on coal devolatilization and char oxidation reactions. Further results concluded that increases in moisture content of the coal feed stock increases the H_2 composition in syngas and increase in gasifier pressure enhances the carbon conversion by increasing the residence time of the char particles. Choi et al. [10] used coal slurry as the feedstock and coupled the slurry evaporation with two phase heat transfer and coal devolatilization. Shrinking core model (SCM) and eddy break up model (EBU) were used to describe particle surface and turbulent chemistry interaction respectively. Liu et al. [11] investigated the effect of turbulence on reaction rates and concluded that char-CO_2 and char-H_2O gasification reactions are least affected by turbulent fluctuations, while the dominant effect is on devolatilization and char oxidation reactions. Bockelie et al. [12] of Reaction Engineering International (REI) developed an in-house comprehensive coal combustion and gasification modeling tool GLACIER by incorporating flow field with full equilibrium chemistry and Probability Distribution Function (PDF) to characterize turbulence. Vincente et al. [13] developed an Eulerian-Eulerian model of an air blown entrained flow gasifier. National Energy Technology Laboratory (NETL) developed a 3D two stage, slurry fed entrained flow gasifier model [14] using commercial CFD software FLUENT and successfully coupled with plant-wide process simulator ASPEN plus through Advanced Process Engineering Co-Simulator (APECS). Shi et al. [15] presented a detailed methodology for CFD modeling of entrained flow gasification in FLUENT using Discrete Phase method where the heterogeneous reaction rates are assumed to be kinetics/diffusion controlled. Wanatabe and Otaka [16] formulated a CFD model predicting the performance of the 2 tpd CRIEPI research scale gasifier using commercial software CFX and compared temperature distribution data with experiments. Harris et al. [17] computed an effectiveness factor based on the heterogeneous reaction rates and included the effect of pressure in their 2D CFD model. More recently Kumar et al. [18] investigated several devolatilization (CPD and Kobayashi) and char combustion sub-models (Unreacted core, Shrinking Core Model and Random Pore Model) and coupled it with gasifier simulations using FLUENT. Ajilkumar et al. [19] developed a 2D CFD model to show the effect of inlet stream temperatures of air and steam. Silaen et al. [20-21] developed 3D CFD models of two stage entrained flow gasifiers and investigated the effect of different turbulence models and fuel injector designs on reactor temperature and syngas composition. Slezak et al. [22] used the CFD model developed by Shi et al. [15] to incorporate the effect of particle density and size fractions. Wu et al. [23] computed different time scales for turbulence, devolatilization, heterogeneous and homogeneous reactions to understand the controlling mechanism in a GE entrained flow gasifier.

Although numerous studies have been carried out on CFD simulation of entrained flow gasification, attempts of detailed model validation of simultaneous, multiple species concentration profile predictions withy experimental data under parametric variation of operating conditions are rare in literature. The main objective of this paper is to investigate the validity of a basic entrained flow gasifier model developed using ANSYS FLUENT, widely used in other CFD studies. Comparison of its syngas composition predictions under different O_2/coal and H_2O/coal feed ratio are presented with benchmark experimental data obtained from Azuhata et al. [24].

MODEL DESCRIPTION

The model developed in the present study is primarily based on the methodology described by Shi et al. [15]. The ultimate and proximate analysis of coal is used as an input parameter and is given in Table D-1. The proximate analysis of coal consists of four components: volatile matter, fixed carbon, moisture and ash. Moisture is released in the initial heating period after the vaporization temperature where as volatile matter breaks up into gaseous components during devolatilization and fixed carbon reacts with gasifying agents in heterogeneous reactions. As described before, the coal gasification process can be assumed to consist of four sub-processes: (1) inert heating and moisture release, (2) devolatilization, (3) char gasification, (4) gas phase reactions. These physical and chemical processes are described in the following sections.

Table D 1: Composition of Utah Bituminous Coal [24]

Proximate Analysis		Ultimate Analysis	
Fixed carbon	40.5	C	66.8
Volatile	38.4	H	5.2
Moisture	6.0	O	9.9
Ash	15.1	N	1.4
		S	0.5
		Ash	16.2
		HHV	26.6 (MJ/kg)

Inert heating and moisture release

The coal particles are injected through an inlet using a carrier gas Argon as used in the experiments. The particle size distribution follows Rosin-Rammler [25] law which can be expressed as

$$Y_d = \exp(-d_P / \bar{d})^n \quad (1)$$

where, $\bar{d}$ is the mean diameter, d_P is the initial particle diameter and n is the spread parameter. The coal particles are heated till the devolatilization temperature, where the inherent moisture of the coal is released at the vaporization temperature (i.e. less than the devolatilization temperature). No chemical reactions or mass transfer processes take place during the inert heating of coal particles. The moisture thus released is added to the gas phase species continuity equation as a source term. The vaporization energy required for moisture release is extracted from the continuous phase.

Devolatilization

The devolatilization phenomenon has a significant impact on the gasification stability and ignition. The volatile break up reaction and evolution of different species is based on a phenomenological model [26]. The major species released during the volatile break up are CO, CO_2, CH_4, H_2, N_2, H_2S, O_2 and H_2O. The stoichiometry of the individual species is maintained through strict elemental balance and enthalpy of formation of the volatile matter is determined from standard state enthalpy balance of product species. A typical volatile matter composition can be expressed as $C_{a1}H_{a2}O_{a3}N_{a4}S_{a5}$, where a_i's are determined from proximate and ultimate analysis. In the present study, two competing rates model by Kobayashi [25] is used to simulate the devolatilization process due to its wide acceptability. The mathematical expression for Kobayashi model is as follows

$$\frac{dm_{vol}}{dt} = m_i \left(\sum_{i=1}^{2} \alpha_i R_i\right) \exp\left(-\int_0^t \sum_{i=1}^{2} R_i dt\right) \quad (2)$$

where, m_i is the initial mass of particle, α_i and R_i are yield factors and reaction rates respectively at two different temperature ranges. The change in particle size due to devolatilization is taken care of by swelling parameter of the coal. More details can be found in [25].

Char gasification

The char gasification reactions take place after the volatiles are released. The reactions take place until all char particles react or exit the gasifier. The heterogeneous reactions are modeled by multiple surface reaction mechanism proposed by Smith [27] i.e. already available as a sub-model in ANSYS FLUENT. The chemical reactions in the gas-solid interaction include char oxidation and reaction of char particle with CO_2 and H_2O after all O_2 is consumed. The major products of surface reactions are CO and H_2, whereas trace formation of methane has also been taken into account. The reactions considered in this model along with reaction rate information are summarized in Table 2.

Gas phase reactions

Several gas phase reactions take place in the gasification and reduction zone of the gasifier including carbon di-oxide and steam formation, water gas shift reaction and methane steam reactions. The homogeneous reactions are modeled using global reaction kinetics to describe gas phase chemistry and are given in Table D-2.

Table D 2: Gasification global reactions

Particle Surface	$C + 0.5\ O_2 \rightarrow CO$	R.1
	$C + H_2O \rightarrow CO + H_2$	R.2
	$C + CO_2 \rightarrow 2CO$	R.3
	$C + 2H_2 \rightarrow CH_4$	R.4
Gas Phase	$CO + 0.5\ O_2 \rightarrow CO_2$	R.5
	$H_2 + 0.5\ O_2 \rightarrow H_2O$	R.6
	$CH_4 + 0.5\ O_2 \rightarrow CO + 2H_2$	R.7
	$CO + H_2O \leftrightarrow CO_2 + H_2$	R.8
	$CH_4 + H_2O \leftrightarrow CO + 3H_2$	R.9

Table D 3: Reaction kinetic parameters [5,9,16]

Reaction	A	n	E (J/kmol)
R.1	0.86	1	1.49×10^8
R.2	1.33	1	1.47×10^8
R.3	4.4	1	1.62×10^8
R.4	1.18×10^{-5}	0	1.49×10^8
R.5	2.2×10^{12}	0	1.67×10^8
R.6	6.8×10^{15}	-1	1.67×10^8
R.7	3×10^8	-1	1.26×10^8

R.8	2.75×10^{10}	0	0.84×10^{8}
	2.65×10^{-2}	0	3.96×10^{3}
R.9	4.4×10^{11}	0	1.68×10^{8}
	5.12×10^{-14}	0	2.74×10^{4}

The kinetic rate expression for global reactions for both heterogeneous and homogeneous reactions are expressed by Arrhenius relationship as following and given in Table D-3.

$$k = AT^{n} \exp(-E / \bar{R}T) \tag{3}$$

The turbulence-chemistry interaction is modeled using a finite rate/eddy dissipation model, a built in module in FLUENT [25] where the effective reaction rate is defined by considering the minimum between turbulence dissipation rate and chemical reaction rate.

Multiphase modeling

As mentioned earlier, the numerical method is based on a coupled Eulerian-Lagrangian formulation in which the conservation equations of the continuous phase are modeled in Eulerian frame and the coal particle trajectory is predicted in a Lagrangian reference frame. The governing equations for mass, momentum, energy and species of the continuous phase are given as

$$\frac{\partial}{\partial x_i}(\rho u_{ij}) = S_m \tag{4}$$

$$\frac{\partial}{\partial x_i}(\rho u_i u_j) = \rho g_j - \frac{\partial P}{\partial x_j} + \frac{\partial}{\partial x_i}(\tau_{ij} - \rho\overline{u_i' u_j'}) + S_j \tag{5}$$

$$\frac{\partial}{\partial x_i}(\rho C_P u_i T) = \frac{\partial}{\partial x_i}(\lambda \frac{\partial T}{\partial x_i} - \rho\overline{C_P u_i' T'}) + \mu\Phi + S_h \tag{6}$$

$$\frac{\partial}{\partial x_i}(\rho u_i C_j) = \frac{\partial}{\partial x_i}(\rho D_i \frac{\partial C_j}{\partial x_i} - \rho\overline{u_i' C_j'}) + S_j \tag{7}$$

Standard $k - \varepsilon$ model with standard wall function is used to model turbulence. The turbulence transport equations are expressed as

$$\frac{\partial}{\partial x_i}(\rho u_i k) = \frac{\partial}{\partial x_i}\left[\left(\mu + \frac{\mu_t}{\sigma_k}\right)\frac{\partial k}{\partial x_i}\right] + G_k - \rho\varepsilon \tag{8}$$

$$\frac{\partial}{\partial x_i}(\rho u_i \varepsilon) = \frac{\partial}{\partial x_i}\left[\left(\mu + \frac{\mu_t}{\sigma_k}\right)\frac{\partial \varepsilon}{\partial x_i}\right] + C_{1\varepsilon}G_k\frac{\varepsilon}{k} - C_{2\varepsilon}G_k\frac{\varepsilon^2}{k} \tag{9}$$

The discrete phase method (DPM) in FLUENT is used to model trajectory of coal particles using a Lagrangian formulation with the assumption that particle volume fraction is less than 10% of the fluid phase and mass feed ratio of solid to gas phase is less than or equal to unity. Hence the gas carries the coal particles and the flow regime is considered to be dilute. The force balance of the particle equates particle inertia with drag force. The turbulent dispersion of the particles is computed using a stochastic tracking model. Heat transfer to the particle includes contribution due to convection, radiation, heat of devolatilization and heat of surface reaction that can be written as

$$\begin{aligned} mC_P\frac{dT_P}{dt} &= hA_P(T_\infty - T_P) + \varepsilon_P A_P \sigma(\theta_R^4 - {T_P}^4) \\ &+ \frac{dm_P}{dt}h_{fg} - f_h\frac{dm_P}{dt}H_{reac} \end{aligned} \tag{10}$$

Radiation heat transfer is incorporated using P-1 model, where scattering is ignored in the gas phase but included for particles.

Finally, SIMPLE algorithm is used to implement pressure-velocity coupling with second order discretization and the continuous phase and discrete phase equations are solved alternatively until a converged coupled solution is obtained.

Operating and Boundary conditions

The geometry of the experimental gasifier is detailed in [5]. High volatile Utah bituminous coal is used for this study. The primary stream consisted of coal and Argon as carrier gas with inlet temperature of 300K and the secondary inlet stream through the annular section contained only steam at 590K. Figure D-1 shows the model geometry, flow direction and inlet streams with computational grid. The parametric cases considered varying O_2/coal and H_2O/coal mass flow ratio are provided in Table D-4.

Table D 4: Operating conditions [24]

	Coal feed rate (kg/hr)	H_2O/coal	O_2/coal
Case-I			0.85
Case-II	23.2		0.95
Case-III	Condition A	0.03	1.05
Case-IV			1.15
Case-I			0.875
Case-II	22.8	0.32	0.975
Case-III	Condition B		1.075

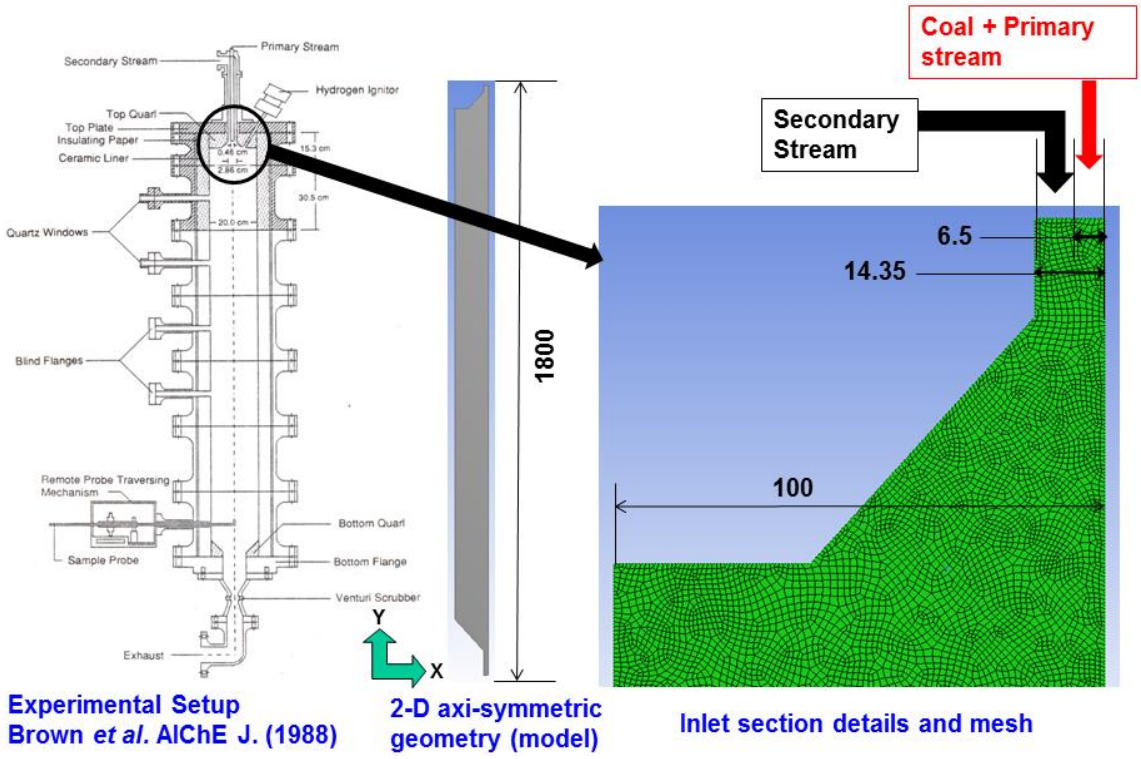

Figure D 1: Model Schematic and computational grid

Argon mass flow rate is 3.31 kg/hr for all the cases. The coal particle size distribution (mean particle diameter 50.4 μm) is also provided in the experiment from which the parameters for Rossin-Rammler distribution are computed. In

the experiment the gasifier was preheated with a methane burner until a stable temperature between 1400K and 1700K was reached and then slowly the coal particles are injected. Simultaneously, the methane flow rate is gradually decreased and stopped when stable coal fame is established. To simulate this initial condition in the CFD model, a temperature of 1500K is patched to gas phase after the cold flow solution is obtained. Temperature patching is required to ignite the mixture while it has no effect on the final solution. The walls of the gasifier are assigned as adiabatic with internal emissivity of 0.8 and reflective boundary conditions are used for discrete phase model. At the outlet, the particle escapes the computational domain. The pressure of the gasifier is 1 atm. The inlet turbulent intensity is assumed to be 5% for all inlet streams based on Reynolds number of the flow.

RESULTS AND DISCUSSIONS

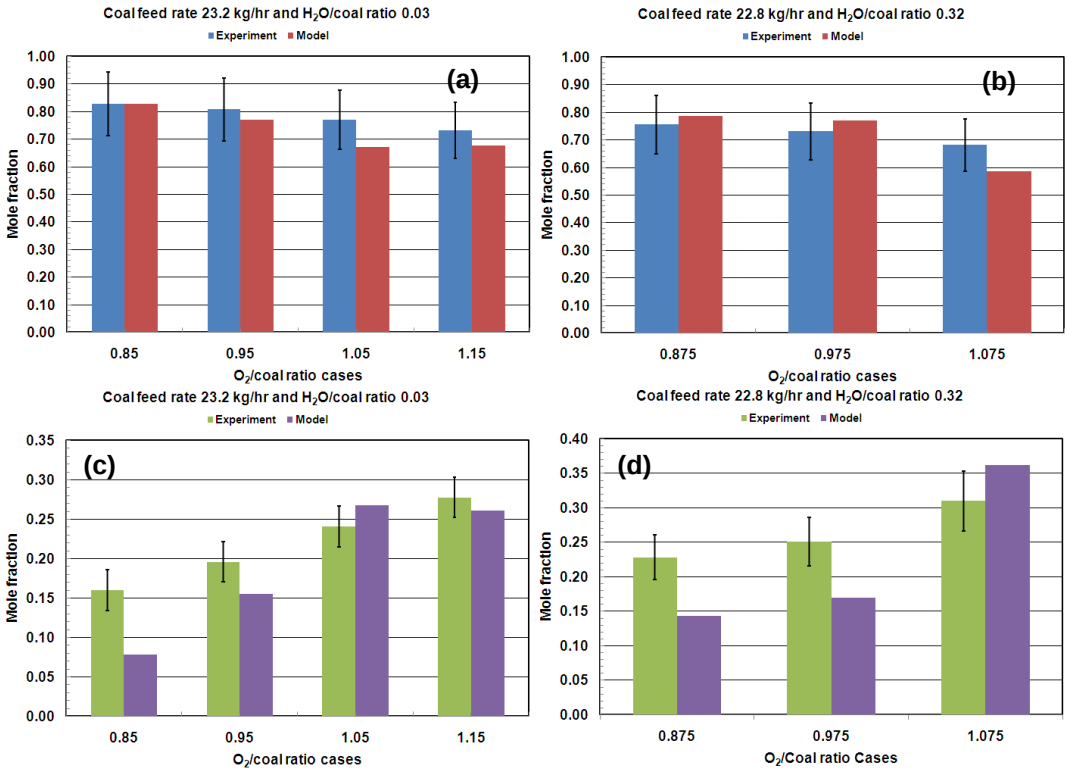

Figure D 2: Comparison with experimental data (a)-(b) syngas composition, (c)-(d) CO2 mole fraction

The effect of O_2/coal ratio on syngas composition is shown in Fig. D-2, where the experimental data are compared with values obtained from the model at the exit of the gasifier. For both coal feed rates and H_2O/coal ratios the model predictions are in good agreement within the error bounds of the experimental data. It can be seen that the effective syngas production ($CO+H_2$) in Fig. D-2(b) is lower for higher H_2O/coal ratio comparing the corresponding O_2/coal feed rates in Fig D-2(a). The CO_2 production increases with increase in O_2/coal feed ratios as presented in Fig. D-2(c) and Fig. D-2(d). Though, the comparisons of model predictions for CO_2 mole fractions are not satisfactory, but the model has been able to capture the correct trend.

To further explain this behavior and understand the fundamental mechanism, axial distribution of species mole fraction within the gasifier are illustrated in Fig. D-3 and Fig. D-4 where, (a), (b) and (c) represent the CO, H_2 and CO_2 mole fractions respectively for two different conditions A and B.

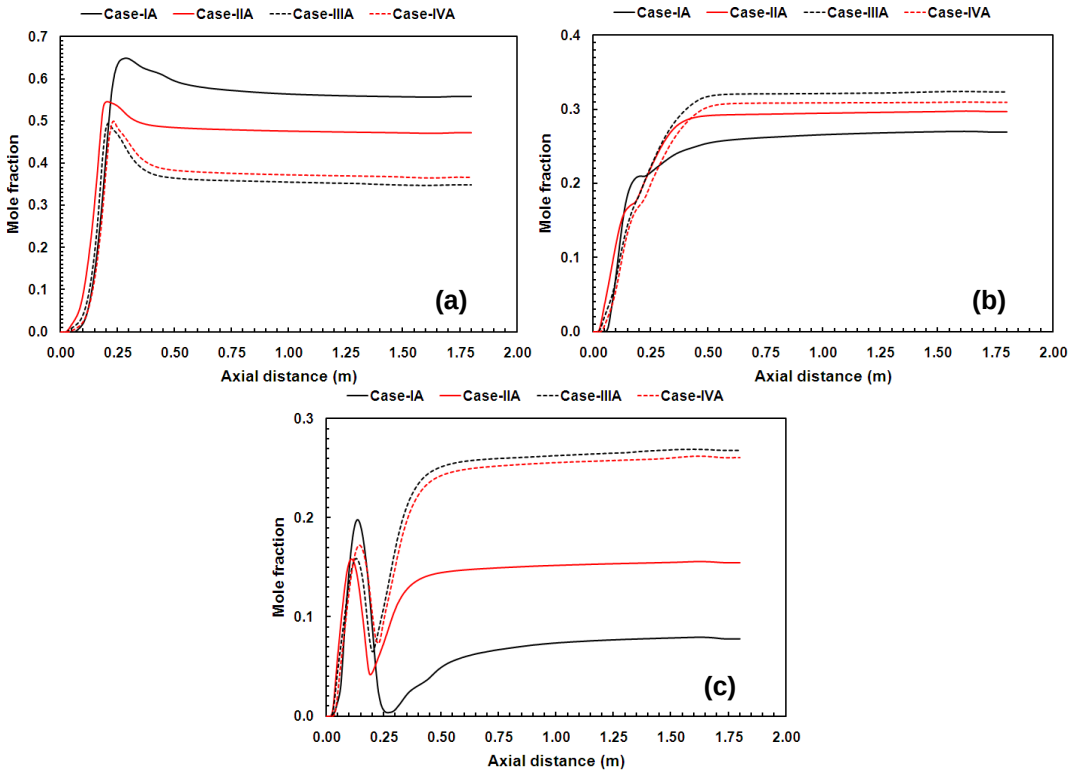

Figure D 3: Axial distribution of species mole fraction for (a) CO, (b) H2, (c) CO2 for Condition A in Table D 4

One major cause of the discrepancy between the experimental data and model predictions might be due to the presence of strong swirl that has been simplified in the model as uniform flow of the inlet streams as the standard $k-\varepsilon$ turbulence model used in this study might not be able to resolve the dispersion of the particles and details of the flow field accurately. The major reason behind choosing the standard $k-\varepsilon$ model as it is computationally inexpensive and other complex turbulence models do not have a significant effect on species distribution [20]. The distribution reveals that the rate of CO formation near the inlet region is very slow whereas the CO_2 mole fraction increases sharply upto a certain length of the gasifier.

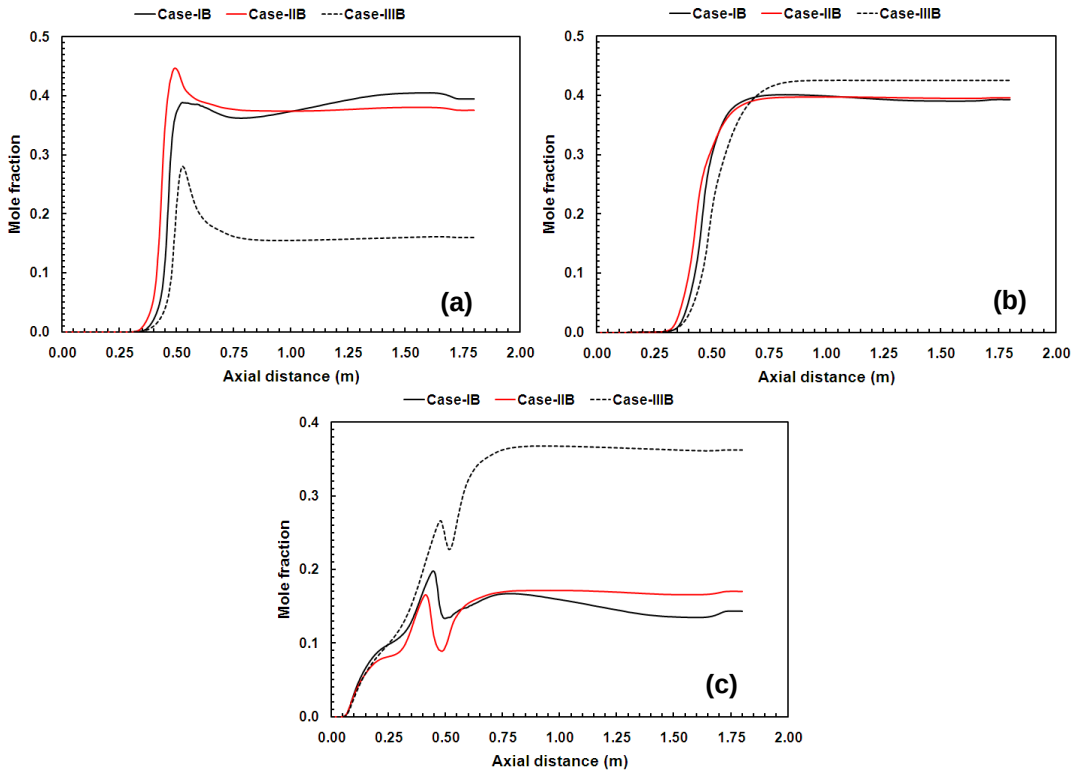

Figure D 4: Axial distribution of species mole fraction for (a) CO, (b) H2, (c) CO2 for Condition B in Table D 4

This phenomenon is amplified in case of higher steam flow rate as seen in Fig. D-4. After, the initial low concentration region period, CO concentration increases rapidly and reaches a peak whereas, at the same location CO_2 mole fraction decreases and comes to a local minima. This phenomenon can be explained as, in the initial phase CO produced from char oxidation can be further oxidized to CO_2 in presence of O_2 as it is seen that CO_2 concentration increases. At the peak concentration level, the heterogeneous particle surface reactions take place more prominently producing more CO and release thermal energy into the gas phase. At this point there is not enough oxygen present to oxidize the produced CO to CO_2. Hence the CO_2 concentration in this region decreases. Now, after all the char has been consumed downstream of the gasification, water gas shift reaction plays a prominent role to convert CO into CO_2 hence CO_2 mole fraction increases again. The difference in devolatilization characteristics between the experiments and the assumed model can also attribute to the initial increase of H_2 and CO concentration.

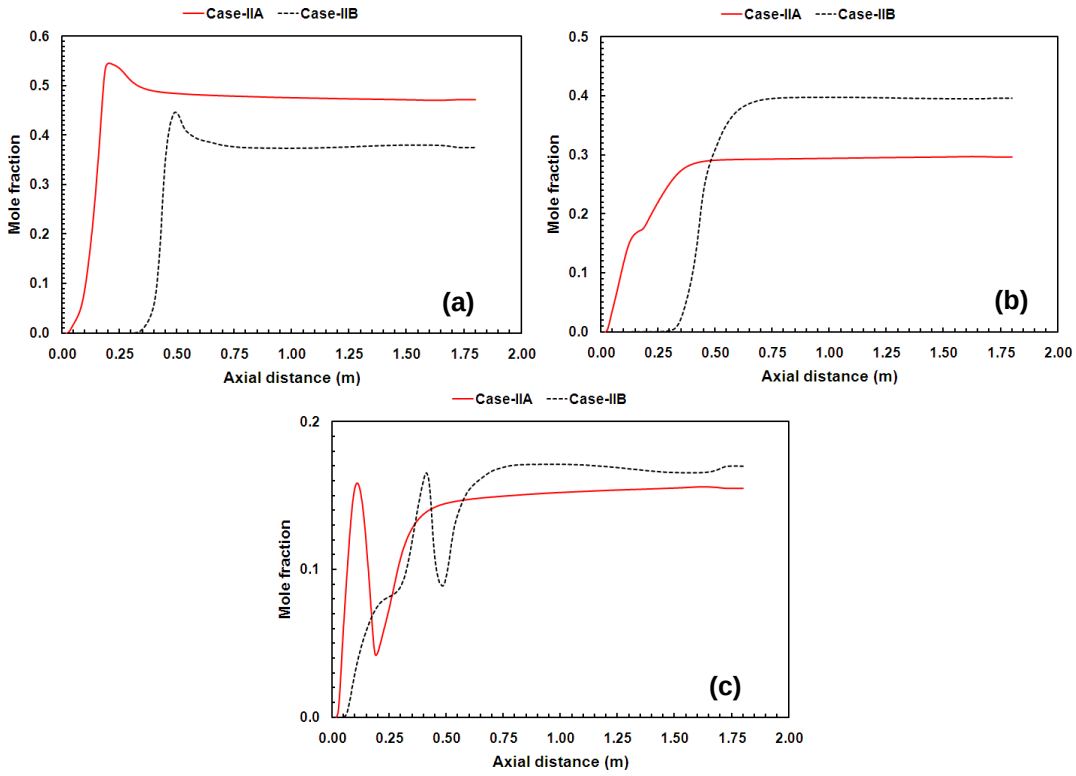

Figure D 5: Effect of H2O/coal ratio for Case-II: species mole fraction distribution for (a) CO, (b) H2, (c) CO2

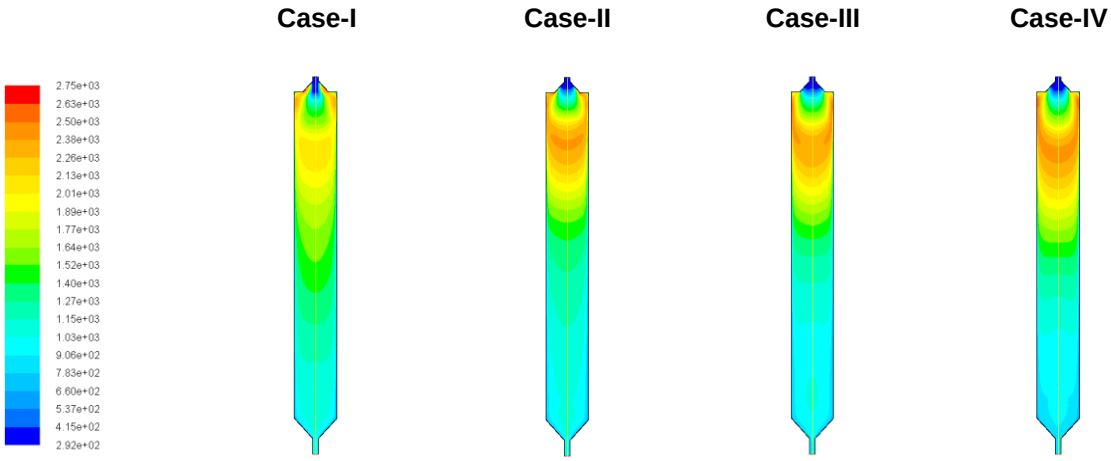

(a) Condition A

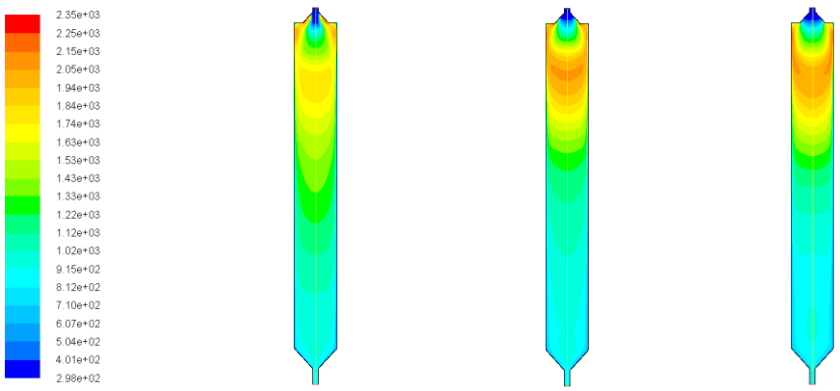

(b) Condition B

Figure D 6: Temperature distribution inside the gasifier for all cases

It can be observed that with increase of O_2/coal ratio, CO_2 production increases by a considerable amount due to oxidation of CO, CH_4 and char combustion as the amount of unreacted carbon decreases. With lower oxygen content the rate of pyrolysis increases, therefore the amount of H_2 concentration decreases and the product gases contain more CO_2 and H_2O due to enhanced combustion in shown in Fig. D-4.

Steam is an important component as a reactant in entrained flow gasification. Though the amount of steam has negligible influence on carbon conversion, it has a significant effect on syngas quality and composition as noted in Fig. D-5 which shows the dependence of increase in inlet steam mass flow rate on species concentration along the axial direction of the gasifier. Water gas shift and char-steam reactions are the controlling factors while the effect of steam addition is investigated. In general steam is injected to obtain H_2 rich syngas fuel, but it is observed that CO_2 concentration also increases and CO yield decreases attributed to the combination of water gas shift and char-steam reaction. The mineral matters present in the coal can act as a catalyst to the water gas shift reaction [7] as it can be seen that the amount of H_2 yield in case of higher steam content is greater than CO concentration at exit.

Figure D-6 (a) and (b) depict the temperature contours for all cases at two different coal feed rates, mentioned in Table D-4 as condition A and B respectively. The rates of gasification and combustion reactions are highly dependent on temperature variations, as evident from Fig. D-6 that higher oxygen ratio increases the temperature of the gasifier due to greater extent of oxidation reactions resulting in increased formation of CO_2. The higher temperature also favors the backward rate of the water gas shift reaction which controls the heterogeneous char-CO_2 and char-H_2O reactions hence an increase in oxygen content yields lower amount of synthetic gases (CO and H_2). It is also observed in Fig. D-6 that higher amount of steam also tends to decrease the gasifier temperature as the rate of char-CO_2 and char-H_2 reactions decrease.

CONCLUSIONS

A 2D axi-symmetric CFD model is developed and the predictions of species mole fraction at the exit of the gasifier are compared with benchmark experimental data under various conditions of O_2/coal and H_2O/coal feed

ratios. The model results matches well with the experimental data for syngas composition. The comparison suggests that the CO_2 formation increases with higher oxygen feed rates and the effective syngas composition decreases. With increase in steam flow rate, H_2 and CO_2 concentration increases but formation of CO decreases, hence lower amount of syngas is produced.

There is a definite scope of improvement in the model results. The model accuracy can be enhanced with further incorporation of the following details:

(1) Accurate devolatilization model along with experimental data to predict the volatile break up species composition, (2) Detailed chemical reaction mechanisms, especially for gas phase reactions where the intermediate radical pools generated controls the reaction chemistry, (3) Better numerical schemes for turbulence model, (4) Effective mesh refinement techniques and computationally inexpensive full scale 3D simulations, (5) Accurate sub-models for wall heat transfer, ash deposition and heterogeneous reaction rate kinetic parameters.

ACKNOWLEDGMENTS

The authors would like to acknowledge the financial support from Advanced Fuel gasification Project funded by Institute for Critical Technology and Applied Sciences (ICTAS), Virginia Tech. Discussions with Dr. Danesh Tafti, Dr. Brian Lattimer and Dr. Francine Battaglia were extremely helpful in the progress of this research work.

REFERENCES

[1] Energy Information Administration, 2007: "International Energy Outlook 2007" http://www.eia.gov/oiaf/ieo/index.html

[2] Breault R.W., Gasification Processes Old and New: A Basic Review of the Major Technologies, Energies, 3 (2010) 216-240

[3] Wen, C.Y., Chaung, T.Z., Entrainment coal gasification modeling, Ind. Eng. Chem. Proc. Dev., 18:4 (1979) 684-695

[4] Govind, R., Shah, J., Modeling and simulation of an entrained flow coal gasifier, AIChE J., 30:1 (1984), 79-91

[5] Brown, B.W., Smoot, L.D., Smith, P.J, Hedman, P.O., Measurement and prediction of entrained-flow gasification processes, AIChE J., 34:3 (1988), 435-446

[6] Hill, H.C., Smoot, L.D., A comprehensive three-dimensional model for simulation of combustion systems, PCGC-3, Energy and Fuels, 7 (1993) 874-883

[7] Smoot, L.D., Brown B.W., Controlling mechanisms for gasification of pulverized coal, Fuel, 66 (1987) 1249-1261

[8] Vamvuka, D., Woodburn, E.T., Senior, P.R., Modeling of an entrained flow coal gasifier 1. Development of the model and general predictions, Fuel, 74 (1995) 1452-1460

[9] Chen, X., Horio, M., Kojima, T., Numerical simulation of entrained flow gasifiers. Part 1. Chem. Engg. Sci., 55 (2000) 3861-3874

[10] Choi, Y.C., Li, X.Y., Park, T.J., Lim, J.H., Lee, J.G., Numerical study on coal gasification characteristics in an entrained flow coal gasifier, Fuel, 80 (2001) 2193-2201

[11] Liu, H., Chen, C., Kojima, T., Theoretical simulation of entrained flow IGCC gasifiers: Effect of mixture fraction fluctuation on reaction owing to turbulent flow, Energy and Fuels, 16 (2002) 1280-1286

[12] Bockelie, M, Denison, M., Chen, Z., Senior, C. and Sarofim A., Using Models to Select Operating Conditions for Gasifiers, Proceedings of the 20th Pittsburgh Coal Conference , 2003

[13] Vincente, W., Ochoa, S., Aquillon, J., Barrios, E., An Eulerian model for the simulation of an entrained flow coal gasifier, App. Thermal Engg., 23 (2003) 1993-2008

[14] Guenther, C., Zitney, S.E., Gasification CFD modeling for advanced power plant simulation, Proceedings of the 22nd International Pittsburg Coal Conference, Pittsburgh, Pennsylvania, September 12-15, 2005

[15] Shi, S.P., Zitney, S.E., Shahnam, M., Syamlal, M., Rogers, W.A., Modeling coal gasification with CFD and discrete phase method, J. Energy Institute, 79(4) (2006) 217-221

[16] Wantabe, H., Otaka, M., Numerical simulation of coal gasification in entrained flow coal gasifier, Fuel 85 (2006) 1935-1943

[17] HLA, S.S., Harris, D.J., Roberts, D.G., CFD modeling for entrained flow gasification reactor using measured intrinsic kinetic data, 5th International Conference on CFD in the Process Industries, Melbourne, Australia, December 13-15 2006

[18] Kumar, M., Zhang, C., Monaghan, R.F.D., Singer, S.L. and Ghoniem, A.F., CFD simulation of entrained flow gasification with improved devolatilization and char consumption submodels, Proceedings of the ASME 2009 International Mechanical Engineering Congress and Exposition, November 13-19, Lake Buena Vista, Florida, USA

[19] Ajikumar, A., Sudararajan, T. and Shet, S.P., Numerical modeling of a steam assisted tubular coal gasifier, Int. J. Thermal Sci. 48 (2009) 308-321

[20] Silaen, A., Wang, T., Effect of turbulence and devolatilization models on coal gasification simulation in an entrained flow gasifier, Int. J. Heat Mass Transfer, 53 (2010) 2074-2091

[21] Wang, T., Silaen, A., Hsu, H.W., Shen, C-H., Top fuel injection design in an entrained flow coal gasifier guided by numerical simulations, Int. J. Thermal Sci., 3(1) (2011) 11009-11017

[22] Slezak, A., Kuhlman, J.M., Shadle, L.J., Spenik, J., Shi, S.P., CFD simulation of entrained floe coal gasification: Coal particle density/size fraction effects, Powder Technology, 203 (2010) 98-108

[23] Wu, Y., Smith, P.J., Zhang, J., Thornock, J.N., Yue, G. Effects of Turbulent Mixing and Controlling Mechanisms in an Entrained Flow Coal Gasifier, Energy and Fuel, 24 (2010) 1170-1175

[24] Azuhata,S., Hedman, P.O., Smoot, L.D., Carbon conversion in an atmospheric pressure entrained flow gasifier, Fuel, 65 (1986) 212-217

[25] ANSYS FLUENT v.13 user manual, ANSYS Inc. 2011

[26] Syamlal, M., Bissett, L.A., METC gasifier advanced simulation (MAGS) model, NITS repot no.

DOE/METC-92/4108 (DE92001111), National Technical Information Service, Springfield, VA, USA, 1992

[27] Smith, I.W., The combustion rates of coal chars: A review, Proceedings of the 19th International Symposium on combustion, The Combustion Institute, 1045-1065, 1982.